Modeling and Design of Semi-Solid Flow Batteries

by

Victor Eric Brunini

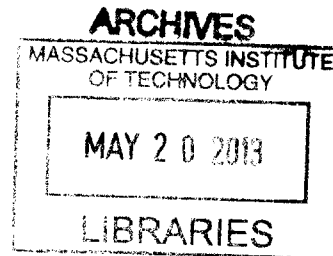B.S., Massachusetts Institute of Technology (2008)

Submitted to the Department of Materials Science and Engineering
in partial fulfillment of the requirements for the degree of

Doctor of Philosophy

at the

MASSACHUSETTS INSTITUTE OF TECHNOLOGY

September 2012

Author . . . .
Department of Materials Science and Engineering
August 7, 2012

Certified by . . . .
W. Craig Carter
Professor of Materials Science and Engineering
Thesis Supervisor

Certified by . . . .
Yet-Ming Chiang
Professor of Materials Science and Engineering
Thesis Supervisor

Certified by . . . .
Christopher A. Schuh
Professor of Materials Science and Engineering
Thesis Supervisor

Accepted by . . . .
Gerbrand Ceder
Chair, Departmental Committee on Graduate Students

Modeling and Design of Semi-Solid Flow Batteries

by

Victor Eric Brunini

Submitted to the Department of Materials Science and Engineering
on August 7, 2012, in partial fulfillment of the
requirements for the degree of
Doctor of Philosophy

Abstract

A three-dimensional dynamic model of the recently introduced semi-solid flow battery system is developed and applied to address issues with important design and operation implications. Because of the high viscosity of semi-solid flow battery suspensions, alternative modes of operation not typically used in conventional redox flow battery systems must be explored to reduce pumping energy losses. Modeling results are presented and compared to experimental observations to address important considerations for both stoichiometric and intermittent flow operation. The importance of active material selection, and its impact on efficient stoichiometric flow operation is discussed. Electrochemically active zone considerations relevant to intermittent flow operation of semi-solid flow batteries (or other potential electronically conductive flow battery systems) are addressed. Finally, the use of the model as a design tool for optimizing flow channel design to improve system level performance is demonstrated.

Thesis Supervisor: W. Craig Carter
Title: Professor of Materials Science and Engineering

Thesis Supervisor: Yet-Ming Chiang
Title: Professor of Materials Science and Engineering

Thesis Supervisor: Christopher A. Schuh
Title: Professor of Materials Science and Engineering

Acknowledgments

I would like to acknowledge the support and advice of many individuals who helped make this work possible. First, my advisors Prof. Craig Carter and Prof. Yet-Ming Chiang for the opportunity to work on this project and their guidance throughout the project. Also thank you to Prof. Chris Schuh for making time to serve as an additional co-advisor, as well as my thesis committee members Prof. John Vander Sande and Prof. Jeff Grossman. Scheduling with such a large committee is challenging, and I greatly appreciate your time, patience, and constructive comments.

Thank you to all of the current and former members of the Chiang and Carter groups who have helped with thought-provoking discussions and advice on various presentations along the way. In particular, thanks to Yajie Dong and Nir Baram for providing experimental data for me to compare my modeling work to.

Finally, thank you to my family and friends for their love and support. I've greatly enjoyed my graduate school experience, and the time spent outside of classes and research has been essential in allowing me to remain focused and motivated while working. Most importantly, thanks to my fiancée Steph for her endless patience and love.

Contents

List of Figures

8

12

List of Tables

Chapter 1

Introduction

Mounting evidence for global climate change and a desire for reduced dependence on oil is driving a flurry of research around electric vehicles and the incorporation of renewable energy sources into the power grid [1–6]. Improvements in energy storage technology represent an important step for the widespread adoption of both electric vehicles and renewable energy generation. Present day battery technology is sufficient for hybrid electric vehicles and short range plug-in hybrid electric vehicles, but meeting the requirements for all-electric vehicles with $\geq$ 150 mile range (150-200 Wh/kg) is likely to require more than the simple evolution of current lithium-ion battery technology [7, 8]. Similarly, the intermittent nature of many renewable energy sources creates a need for large scale inexpensive energy storage solutions to perform load leveling. A variety of existing energy storage technologies have been considered for grid-scale storage, with the two most widely adopted being pumped hydroelectric and compressed air energy storage because of the lower associated costs [9, 10].

Recently, ARPA-E announced funding opportunities for research in energy storage aimed at both transportation (BEEST) and grid-scale storage (GRIDS) [7, 11]. Semi-solid flow batteries (SSFCs) are a novel energy storage technology recently proposed to potentially address both grid-scale and transportation scale energy needs [12]. The motivating concept behind semi-solid flow batteries is the goal of combining the high energy density of Li-ion batteries with the flexible system architecture and low costs of redox flow batteries.

In this thesis a continuum model of semi-solid flow battery operation is developed and applied to address three relevant issues for SSFC operation. In Chapter 2 the model is applied to study the effects of active material selection on operating an SSFC under low flow rate conditions. In Chapter 3 the model is used to study the extended electrochemically active zone that develops as a result of the suspensions used as electrode materials being mixed ionic and electronic conductors. Finally, in Chapter 4 the use of the continuum model solved using finite element methods as a design tool for improving SSFC performance is discussed.

1.1 Background

1.1.1 Redox Flow Batteries

Redox flow batteries are a type of energy storage system that store energy using redox reactions between species in two liquid electrolytes. A variety of different chemistries, primarily aqueous, have been explored for use in redox flow batteries; examples include: bromine-polysulphide, all vanadium, vanadium-bromine, iron-chromium, zinc-bromine, and zinc-cerium [13]. Since they are aqueous the typical voltage of a redox flow battery is limited to 1-1.5 V to avoid electrolysis of water. The combination of this small potential window and solubility limits of the dissolved species limit conventional aqueous redox flow battery systems to energy densities of approximately 40 Wh/kg, significantly lower than needed for practical EV applications [13]. More recently, some attempts have been made at using non-aqueous chemistries for redox flow batteries in order to reach higher voltages, and therefore improved energy density [14–17]. The primary advantages of redox flow battery systems are two-fold: first, they are capable of extremely high cycle life since no solid-state reactions are present, and second they are relatively low cost systems [15].

Another important characteristic of redox flow battery systems that differentiates them from other battery systems is that they separate the system power and energy storage capacity as design variables. This is accomplished by storing the electrolyte

solutions in external tanks and pumping them through a power stack where the electrochemical reaction takes place and power is extracted. Figure 1-1 shows a schematic of a redox flow battery system. As an example consider the all-Vanadium redox flow system [18]. In the all-Vanadium system both electrolytes use H_2SO_4 solutions as the solvent. The species of interest in the anolyte are V^{2+} and V^{3+}, and in the catholyte they are VO^{2+} and VO_2^+. The anodic half-reaction is:

$$V^{2+} \rightleftharpoons V^{3+} + e^- \tag{1.1}$$

with a potential of -0.255 V vs SHE. The cathodic half-reaction is:

$$VO^{2+} + H_2O \rightleftharpoons VO_2^+ + 2H^+ + e^- \tag{1.2}$$
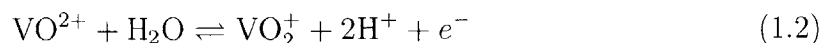
with a potential of 1.004 V vs SHE. Each reaction occurs at the surface of the electrode in its respective half of the cell as seen in Fig. 1-1. A porous carbon felt is frequently used for the electrode in either a flow-through or flow-by configuration in order to increase the available surface area for the electrochemical reaction to occur. An ion exchange membrane similar to Nafion is used to separate the anolyte and catholyte solutions and prevent cross-contamination of the solutions while allowing the ion transport necessary for the reaction to proceed. As previously mentioned, since the electrochemical reaction occurs entirely within the power stack region it is possible to scale the amount of power a flow battery system can produce by changing the stack size, while separately varying the energy storage capacity of the system by changing the tank size.

This separation of system power and storage capacity as design variables has several advantages. In a conventional battery architecture the fraction of inactive material (current collector, separator, etc.) in the system is constant, and therefore for applications with high energy to power ratios more inactive materials than are strictly necessary to meet the power requirements must be used in order to meet the energy requirements. It is possible to somewhat mitigate this effect by designing cells for either high energy, low power applications (e.g. by using thicker electrodes), or
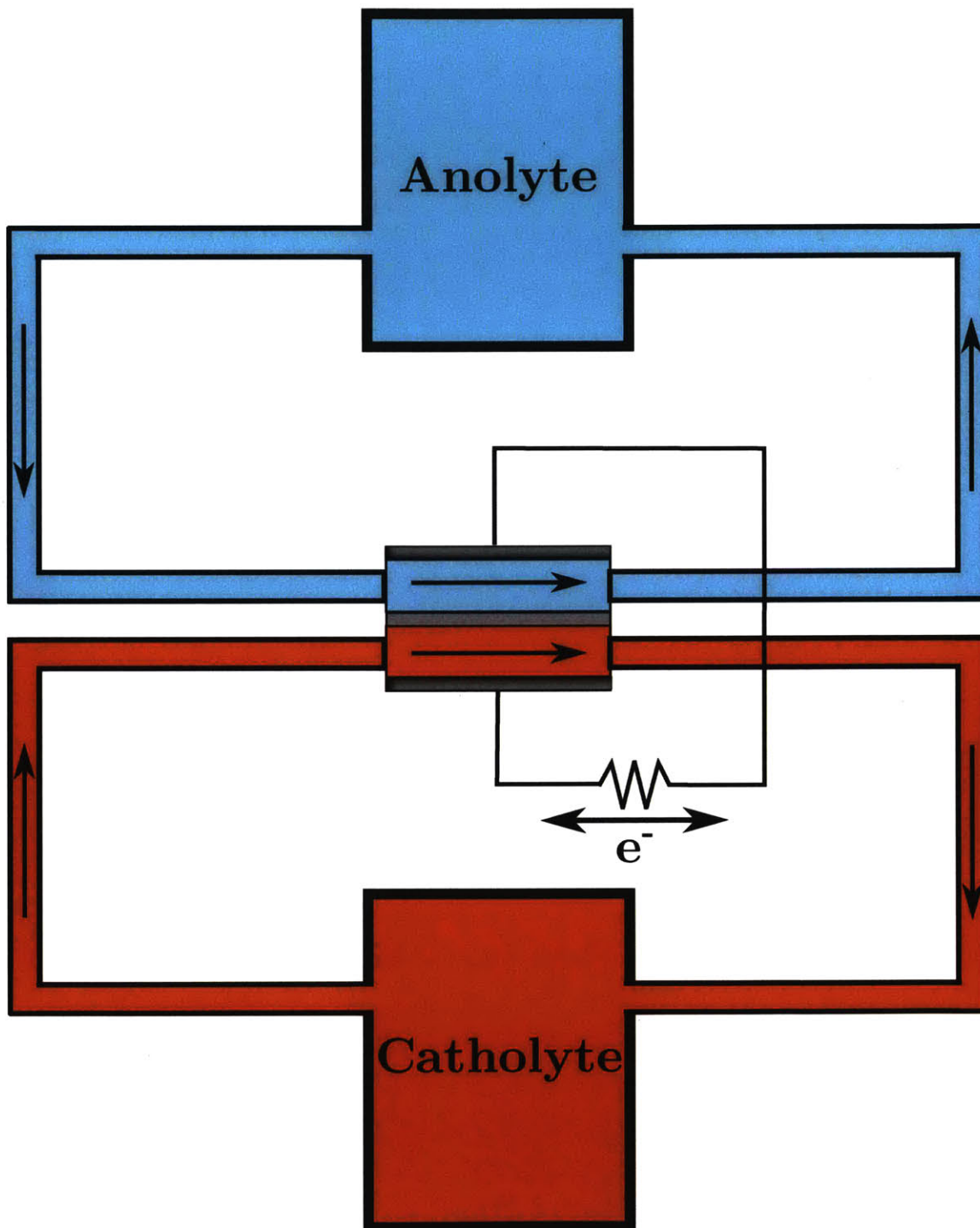
Figure 1-1: Schematic of a redox flow battery system. The anolyte and catholyte are stored in external tanks and pumped through a power stack where power is extracted from the system.

high power, low energy applications (e.g. thinner electrodes), however the fraction of inactive components remains relatively high in practice. For example, in Li-ion battery systems the inactive components typically compose $\approx 30 - 50\%$ of the total system mass [19]. In contrast, flow battery systems may be designed to target a specific energy to power ratio by scaling the size of the cell stack to meet power requirements, and the size of the electrolyte storage tanks to meet the energy requirements. This has the potential to significantly reduce the fraction of inactive components in the overall system, potentially leading to higher energy density and lower costs. This advantage is particularly noticeable for applications requiring high energy to power ratios. As the energy to power ratio increases the size of the storage tanks increases relative to the size of the stack, and therefore the overall system energy density asymptotically approaches the energy density of the active electrolyte solutions.

These characteristics make redox flow batteries of particular interest for grid-scale storage applications where energy density is relatively unimportant, but low costs are extremely important. Several demonstration scale redox flow battery systems have been installed for grid scale storage around the world, including a 50 KW/200 kWh system built by Kashima-Kita Electric Power in 1995 and more recently a 4 MW/6 MWh demonstration system built by Sumitomo Electric Industries for use at the 32 MW Tomamae wind farm in Japan [20]. Additionally, redox flow batteries remain an active area of research, particularly in terms of increasing cell stack power density to reduce total stack size and therefore cost, and in exploring new chemistries to potentially improve system level energy density [14–17].

1.1.2 Lithium-Ion Batteries

Lithium-ion batteries first appeared commercially in the 1990s, and subsequently have come to dominate the portable electronics industry due to their excellent volumetric and specific energy density [21]. The fundamental operation of a Li-ion battery consists of the transport of Li^+ between a cathode material with a low chemical potential for Li, and an anode material with a high chemical potential for Li. As in
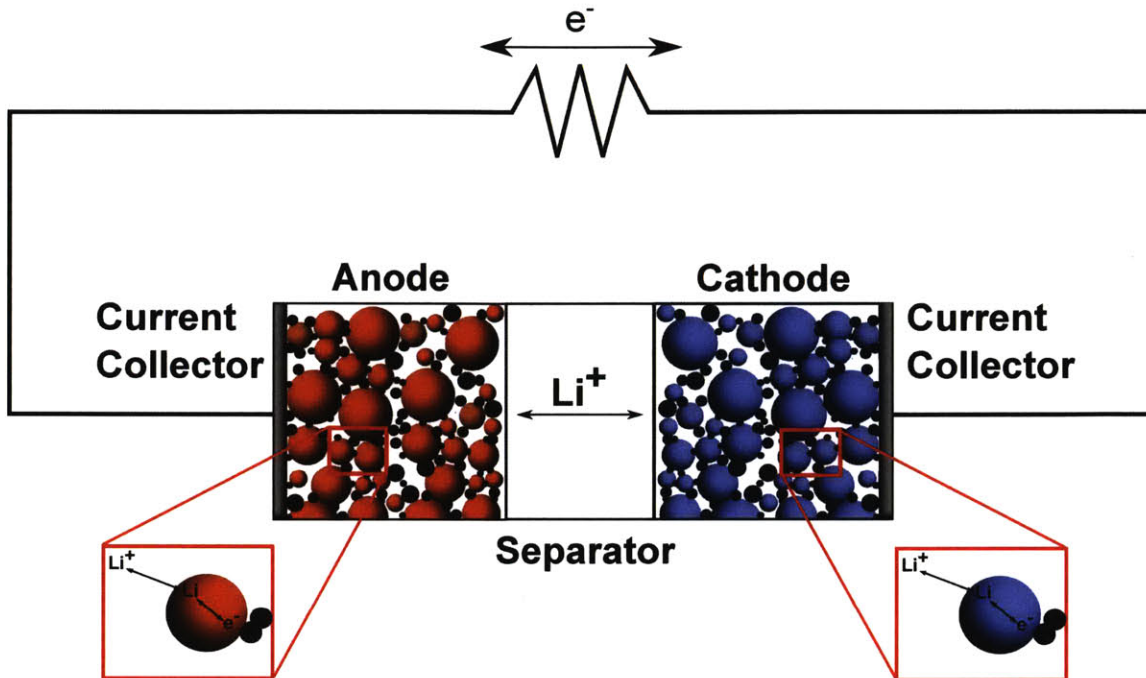
Figure 1-2: Schematic of a Li-ion battery. In addition the dual-intercalation arrangement depicted some Li batteries are constructed using a Li metal anode with a mechanically tougher polymer separator to reduce dendrite formation on charge.

any battery system, the Li^+ ions pass between anode and cathode directly through a separator material, while the electrons needed for the electrochemical reaction to occur are forced to travel through the external circuit. A schematic depicting the operation of a Li-ion battery is presented in Fig. 1-2. Li-ion cells are created by either spiral-winding or stacking of the current collector-anode-separator-cathode-current collector sandwich to create cylindrical or prismatic cells respectively. In contrast to redox flow batteries, both the specific energy and specific power of a Li-ion battery are determined by the particular cell configuration. Therefore, in order to meet system level design specifications additional cells are needed to increase either the total power or total storage capacity, i.e. system power and energy capacity are linked variables.

The first Li-ion batteries used $LiCoO_2$ as the intercalation compound on the cathode side and matched it against a carbonaceous anode material [21]. This combination results in a 3.5V cell with a specific energy around 130 Wh/kg [22]. More recently a great deal of research has been performed with the goal of improving both an-

ode and cathode performance. On the cathode side a variety of new materials have been tested with various goals such as improved rate performance, higher capacity, higher voltage, improved safety and reduced cost; some examples include $LiFePO_4$, $LiNi_{1/3}Mn_{1/3}Co_{1/3}O_2$, $LiMn_2O_4$ spinel, etc. [23, 24]. Significant effort has also been put into improving anode materials. One of the major challenges for constructing fast-charging Li-ion batteries is the deposition of Li metal in the anode during high-rate charging. One approach that has been taken to circumvent this problem is the use of higher voltage anode materials, in particular lithium titanate ($Li_4Ti_5O_{12}$) has been given a great deal of attention in this regard [25–27]. Another potential anode material that has received a lot of attention is Si. Si is very exciting as an anode material because of its extremely high specific capacity, around 1170 mAh/g on the first discharge [22]. Unfortunately, during the intercalation process Si undergoes 400% volumetric expansion which leads to rapid capacity fade [28]. This rapid capacity fade has thus far greatly limited Si's practical applications as an anode material, however many researchers are attempting to address the issue through various alloying and nano-structuring techniques [22, 29–31].

While these new advancements are promising, it is still expected to be a significant challenge for conventional Li-ion batteries to meet the needs of PHEV and EV applications, particularly the specific energy (> 200 Wh/kg) and cost targets [7]. The inactive materials needed to construct a working Li-ion cell (current collector, separator, binder, etc.) are a significant cost driver and also reduce the practical specific energy of a full cell since only 30-50% of the total mass of a cell consists of the active storage material [19]. As a result, reducing the amount of inactive material present in a cell is an attractive method of improving energy density. The two primary methods available to decrease the amount of inactive material are increasing electrode thickness and decreasing electrode porosity, however both of these negatively impact rate capability. Therefore no significant reduction in the fraction of inactive material present in a Li-ion cell is expected in the near future.
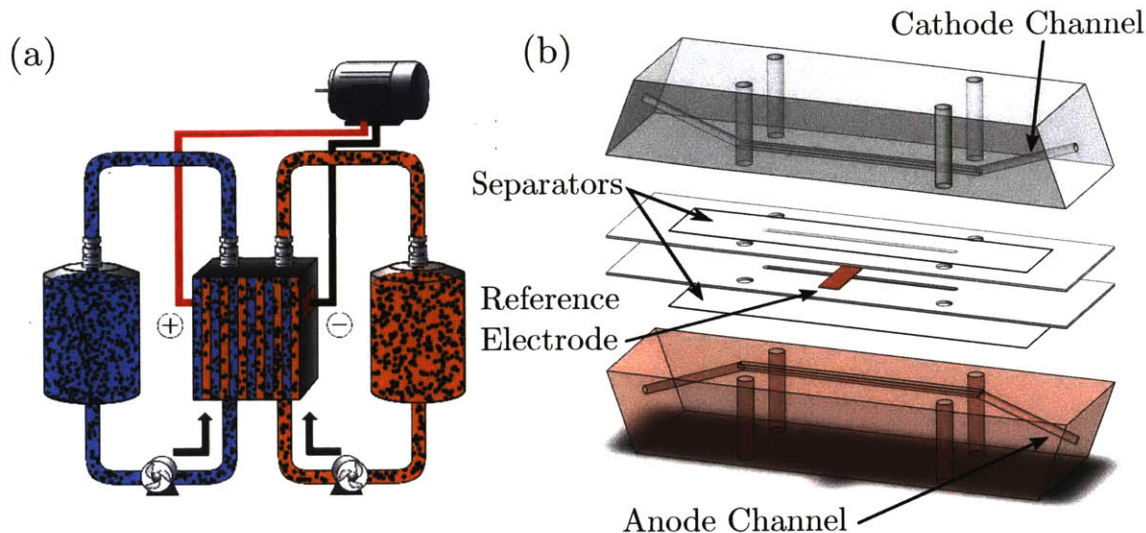
Figure 1-3: Schematic of Semi-Solid Flow Battery. (a) Similar to a conventional flow battery the "electrolytes" are stored in external tanks and pumped through a power stack where the electrochemical reaction occurs. In an SSFC the "electrolytes" are composite suspensions consisting of the liquid electrolyte solvent, active storage particles, and particles of conductive carbon additive. (b) CAD drawing of a lab-scale SSFC test cell.

1.1.3 Semi-Solid Flow Batteries

Semi-solid flow batteries (or semi-solid flow cells, SSFCs), are a novel energy storage system that was recently introduced [12]. The main innovation behind SSFC systems is the use of suspensions containing solid storage compounds and conductive carbon additive as the "electrolyte" in a flow battery system. This enables the use of Li-ion battery materials in a flow cell architecture. The advantage of this approach in comparison to conventional redox flow batteries is the ability to reach much higher energy density, upwards of 200 Wh/kg is projected to be feasible. The advantage compared to conventional Li-ion cells is in the flexibility to vary system power and storage capacity independently that is gained by using the flow battery architecture. This flexibility is expected to enable higher energy density and lower costs than conventional Li-ion cells by reducing the amount of inactive material in the system.

Figure 1-3 shows a schematic of an SSFC system in (a), and a CAD rendering of a lab scale test cell in (b). As in a conventional redox flow battery system the energy

22

storage material is stored in external tanks and pumped through a power stack where the electrochemical reaction takes place and power is extracted. However, there are several important differences to note between SSFCs and conventional redox flow batteries. In a redox flow battery the energy storage material consists of ions dissolved in a liquid (typically aqueous) electrolyte. In a SSFC the energy storage material is a composite suspension containing three key components. The first component is the liquid electrolyte that suspends the solid components. All published work so far uses non-aqueous electrolytes common in Li-ion batteries (e.g. $LiPF_6$ dissolved in an alkyl carbonate mixture), however aqueous SSFCs are possible. The electrolyte serves to provide ionic conductivity to the semi-solid suspension. Suspended in the electrolyte are two types of solid particles, the active storage material (e.g. $LiCoO_2$ (LCO), $LiFePO_4$ (LFP), etc.) and a conductive carbon black additive. The conductive carbon black additive forms a fractal percolating network which allows electronic conductivity throughout the semi-solid suspension [32]. This carbon network also serves to stabilize the active storage particles and prevent them from settling out of the suspension.

Since these semi-solid suspensions are both ionic (through the electrolyte) and electronic (through the carbon network) conductors the design of the power stack differs somewhat from that of a conventional redox flow battery. In a conventional redox flow battery the liquid electrolyte provides the ionic conductivity, just as in an SSFC. However since the liquid electrolyte is not electronically conductive the electrochemical reaction can only take place at the surface of the current collector. As a result, a porous carbon felt or mesh is commonly used to increase the electrode surface area available for the reaction. In an SSFC this porous carbon electrode is unnecessary because the semi-solid electrode suspension itself is electronically conductive. Therefore every particle of active storage material that is connected to the conductive carbon network is already electrochemically active. Another important difference in cell design is in the type of material needed for the separator. Conventional redox flow batteries must use Nafion, or a similar ion conducting membrane, to prevent cross-contamination of the electrolyte solutions. SSFCs can use much cheaper porous membranes since only the solid particles need to be prevented from crossing

over between anode and cathode.

While the conductive carbon network is essential for providing the electronic conductivity necessary for a functioning battery and stabilizing the active storage particles in suspension, it does have one major drawback. The viscosity of the semi-solid electrode suspensions used in SSFCs is $\approx 10^3$ times greater than that of the aqueous electrolytes used in conventional redox flow batteries [12, 32, 33]. This greatly increases the amount of energy needed to pump the semi-solid electrode suspensions, and as a result has important implications for efficient operation of an SSFC.

In summary, SSFCs are a novel energy storage system designed to combine the high energy density possible using Li-ion chemistry with the flexible system architecture of redox flow batteries. By combining the advantages of these two types of energy storage system it is hoped that SSFCs can achieve higher energy density at a lower cost than either type of system on its own, and therefore serve as a viable system for both EV and grid scale storage.

1.2 Model Development

A dynamic 3D model of flow battery operation that couples ionic flux, electronic current, and hydrodynamic flow is presented here. Furthermore, a non-Newtonian flow model is included, and the model is capable of computing time-dependent non-uniform current density distributions during galvanostatic operation. The model is first presented for the general case, and then simplifying assumptions are applied to facilitate numerical simulation and to treat specific chemistries.

Initially, a model that tracked individual active particles was considered in order to be able to model morphological changes in the semi-solid suspensions as a result of flow. However, early work made it clear that the computational requirements for such a model would be too high, and as a result a volume-averaging approach based off of the porous-electrode model of Newman and co-workers [34–38] was adopted. This volume-averaging approach has been very successfully applied to modeling both Li-ion and redox flow battery systems, and therefore is expected to be similarly applicable

24
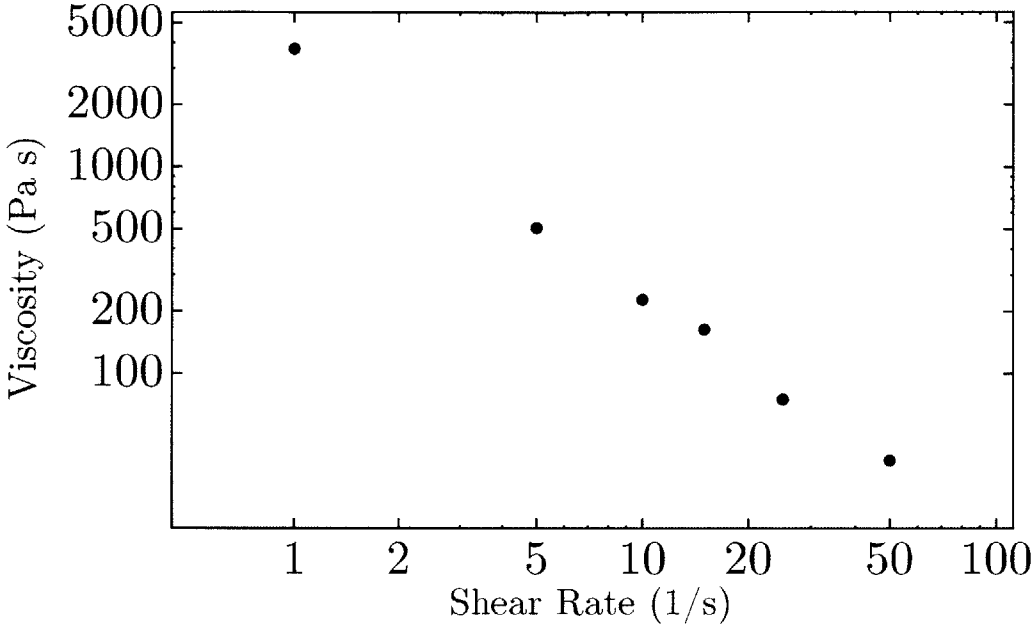
Figure 1-4: Viscosity vs. Shear Rate for a SSFC electrode suspension (20 vol% LiNi$_{1/3}$Mn$_{1/3}$Co$_{1/3}$O$_2$ with 3.5 vol% C45 carbon in Diakin electrolyte) exhibiting Non-Newtonian shear thinning behavior. Axes are log scale.

to SSFC systems.

Since the entire semi-solid electrode suspension is flowing, convection terms are added corresponding to macroscopic motion of the slurry to mass transport equations for both the salt concentration in the electrolyte and the concentration of lithium in the active intercalation particles. The computational domain corresponds to a half-cell configuration as illustrated in Fig. 1-5 (i.e., a lithium metal negative electrode provides a reference electrode of constant lithium chemical potential across the mid-plane of the cell). The method can obviously be extended to full-cell configurations in which flowing semi-solid electrodes on both sides of the separator exhibit coupling between hydrodynamics and electrochemistry (Both cell types were utilized in the experiments of Duduta et al. [12]).

1.2.1 Flow Modeling

At desirable solids loading fractions, the SSFC suspensions exhibit non-Newtonian shear-thinning behavior [12]. The flow of the active suspension is modeled using the

incompressible Navier-Stokes equations with a power law viscosity:

$$\mu = C\dot{\gamma}^{n-1} \tag{1.3}$$

$$\rho\left(\frac{\partial \vec{u}}{\partial t} + \vec{u} \cdot \nabla \vec{u}\right) = -\nabla p + \nabla \cdot \left(\mu(\nabla \vec{u} + (\nabla \vec{u})^T)\right) \tag{1.4}$$

where μ is the viscosity, $\dot{\gamma}$ the shear rate, p the pressure, and $\vec{u}$ the fluid velocity. Model parameter definitions, symbols and values are given in Table 1.1. The slurry and its rheological behavior are assumed to be homogeneous at all times. The local velocities of the solid and liquid phases in the suspension are assumed to be the same. The rheological yield stress is assumed to be zero. The constant, C, and exponent, n, in the viscosity function are obtained by fitting to experimental data reported elsewhere [12]. The density, ρ, is computed from the volume fractions and densities of the suspension components. For stoichiometric flow the Reynolds number is of order 10^{-4} to 10^{-6} , and therefore the flow is assumed to be laminar. The cell charge rate corresponding to those stoichiometric flow Reynolds numbers is 5C - C/10, spanning a realistic range for battery operation. No-slip boundary conditions are implemented at the current collector walls and the separator interface. Laminar boundary conditions are applied at the inlet and outlet, with a prescribed flow rate Q at the inlet and pressure $p = 0$ at the outlet.

1.2.2 Electrochemical Modeling

Bulk Equations

Semi-Solid Electrode

The electrostatic potential in the solid particulate phase is modeled by combining Ohm's law with a current source term corresponding to the local electrochemical reaction rate:

$$\nabla \cdot (\sigma \nabla \phi_s) - F a_s j_n = 0 \tag{1.5}$$
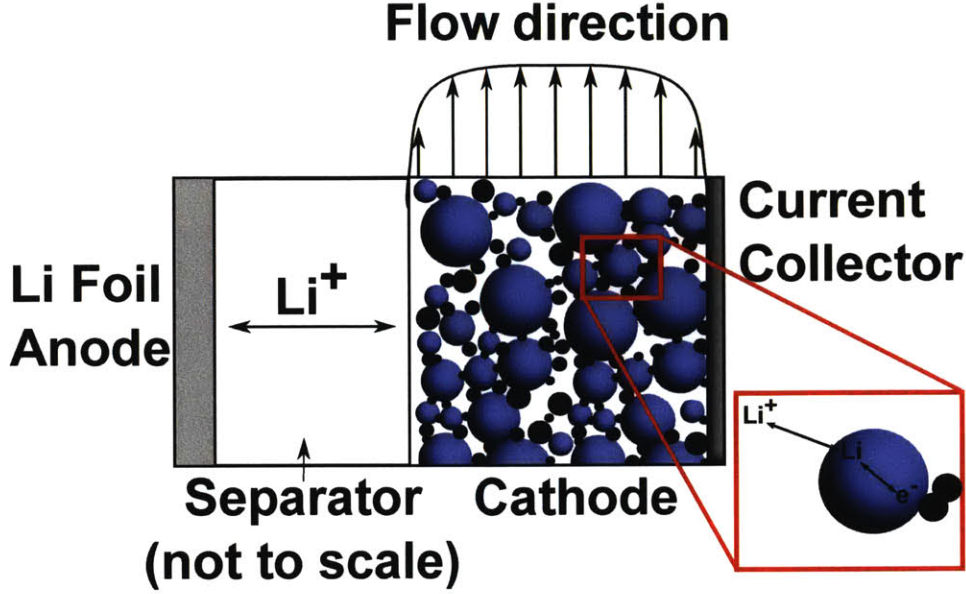
Figure 1-5: Schematic showing modeled regions of an SSFC

Here σ is the electronic conductivity of the solid phase, ϕ_s is the potential in the solid phase, F is Faraday's constant, a_s the specific surface area of the intercalation particles, and j_n the reaction rate at the particle surface. Within the electrolyte phase, the potential, ϕ_e, is given by [35]:

$$\nabla \cdot \left(\kappa_{\text{eff}} \nabla \phi_e - \frac{\kappa_{\text{eff}} RT}{F} \left(1 + \frac{\partial \ln f_a}{\partial \ln c_e} \right) \left(1 - t_+^0 \right) \nabla \ln c_e \right) + F a_s j_n = 0 \qquad (1.6)$$

where κ_{eff} is the effective ionic conductivity of the electrolyte, t_+^0 is the transference number, f_a is the activity coefficient of the dissolved salt species, and c_e is the salt concentration described below. Because the electrolyte is assumed to be electrically neutral in its bulk there is no charge convection in the system.

The concentration in the electrolyte phase and the Li concentration in the solid phase are modeled by applying mass conservation and including convective terms. The salt concentration, c_e, is given by:

$$\frac{\partial c_e}{\partial t} = \nabla \cdot (D_{\text{eff}} \nabla c_e) - \frac{\vec{i_e} \cdot \nabla t_+^0}{z_+ \nu_+ F} + \frac{a_s j_n (1 - t_+^0)}{\epsilon} - \vec{u} \cdot \nabla c_e \qquad (1.7)$$

where ϵ is the volume fraction of the electrolyte. Valoen and Reimers [39] demon-

strated experimentally that t_+^0 is independent of c_e in a similar electrolyte so the $\vec{i_e} \cdot \nabla t_+^0$ term is neglected as a simplifying assumption. In addition, a regular solution model for the salt is assumed: $\frac{\partial \log f_a}{\partial \log c_e} = 0$ in Eq. 1.6.

In principle the intercalated lithium concentration, c_s, may be modeled as a scalar field on a four dimensional space where the fourth coordinate, r, is the radial position within a spherical particle at position $\vec{x}$. The concentration will evolve by diffusion within each particle and through convection of the particles in the suspension.

$$\frac{\partial c_s}{\partial t} = \left[D_s \frac{\partial^2 c_s}{\partial r^2} + \frac{2D_s}{r} \frac{\partial c_s}{\partial r} \right] - \vec{u} \cdot \nabla_x c_s \tag{1.8}$$

In order to make the problem more tractable, solid state diffusion is assumed not to be a limiting process (valid for low charge rates) and therefore the solid phase's Li concentration is treated as uniform within each particle. This reduces the mass conservation equation for the intercalated lithium to a convection equation with a source term corresponding to the electrochemical reaction rate:

$$\frac{\partial c_s}{\partial t} = -\frac{a_s j_n}{1 - \epsilon} - \vec{u} \cdot \nabla c_s \tag{1.9}$$

Finally, the local reaction rate, j_n, is given by a Butler-Volmer expression [35]:

$$j_n = i_0 \left[\exp\left(\frac{\alpha e(\phi_s - \phi_e - \phi_{eq})}{k_B T} \right) - \exp\left(\frac{-\alpha e(\phi_s - \phi_e - \phi_{eq})}{k_B T} \right) \right] \tag{1.10}$$

Separator

In the separator region no electrochemical reaction takes place, and c_e and ϕ_e are the only relevant variables. The model equations simplify to:

$$\nabla \cdot \left(\kappa_{\text{eff}} \nabla \phi_e - \frac{\kappa RT}{F} \left(1 - t_+^0 \right) \nabla \ln c_e \right) = 0 \tag{1.11}$$

$$\frac{\partial c_e}{\partial t} = \nabla \cdot \left(D_{\text{eff}} \nabla c_e \right) \tag{1.12}$$

In both the semi-solid electrode and separator, the effective ionic conductivity and diffusivity are modeled by a Bruggeman dependence on electrolyte volume fraction:

$$\kappa_{\text{eff}} = \kappa \epsilon^{3/2} \tag{1.13}$$

$$D_{\text{eff}} = D \epsilon^{3/2} \tag{1.14}$$

Boundary Conditions

As in the porous electrode theories, the current is carried entirely in the solid phase at the current collector and entirely in the electrolyte phase at the separator interface. Therefore, zero salt-flux and ionic-current boundary-conditions are applied at the current collector (the current collector interface is the entire shaded region in Fig. 1-5) for c_e and ϕ_e in Eqs. 1.7 and 1.6. Similarly, a zero current boundary-condition is applied to the solid phase potential equation at the separator interface. At the inlet of the channel, the salt concentration and intercalated lithium-concentration are both fixed at the inlet storage tank values given in Table 1.1, and zero current boundary-conditions are applied to both the solid and electrolyte phase potentials. At the channel outlet, zero diffusive mass-flux boundary conditions are applied to both mass conservation equations, and zero current boundary conditions for both potential equations. Zero flux boundary conditions are applied to the c_s mass conservation equation at the current collector and separator—semi-solid electrode interface. Additionally, a symmetry boundary condition is applied to all equations along the midplane of the channel.

The constant current density boundary conditions typically used for the solid phase potential at the current collector and electrolyte phase potential at the lithium foil anode cannot model the spatial variation in current density present during sto-ichiometric flow rate operation. Instead the experimental approach to galvanostatic operation is mimicked, in which the testing apparatus uses a feedback loop to control the applied voltage in order to maintain a constant current. A potentiostatic boundary condition is applied with an *a priori* estimate of the applied electrical potential

at the current collector boundary, ϕ_{applied}, and the estimate is iteratively refined until the galvanostatic constraint:

$$I_{\text{applied}} = \int_{\text{CC}} \vec{j} \cdot \hat{n} dA \tag{1.15}$$

is satisfied, where I_{applied} is the desired current, $\vec{j}$ is the electronic current density, $\hat{n}$ is the unit normal to the current collector surface, and $\int_{\text{CC}}$ represents integration over the entire current collector interface.

The second electrochemical reaction present in the system occurs at the Li-foil surface where Li^+ ions in solution are either plated onto or dissolved from the foil. Therefore, Eq. 1.12 should have a constant flux boundary condition for c_e and Eq. 1.11 should have a constant current boundary condition for ϕ_e. The magnitudes of the salt flux and ionic current depend on the local electrochemical reaction rate at the foil surface. This local reaction rate will depend on the value of ϕ_e and can be modeled using a Butler-Volmer term for the lithium anode as in [38].

$$-D_{\text{eff}} \nabla c_e \cdot \hat{n} = -\frac{1 - t_0^+}{\epsilon} \cdot i_0^n \left(\exp \left(\frac{-e\phi_e}{2k_BT} \right) - \exp \left(\frac{e\phi_e}{2k_BT} \right) \right) \tag{1.16}$$

$$-\kappa_{\text{eff}} \nabla \phi_e \cdot \hat{n} = -F \cdot i_0^n \left(\exp \left(\frac{-e\phi_e}{2k_BT} \right) - \exp \left(\frac{e\phi_e}{2k_BT} \right) \right) \tag{1.17}$$

Where possible this boundary condition is used in the form shown in Eqn. 1.17, however for the stoichiometric flow simulations in Chapter 2 it resulted in some numerical instability. In the simulations that were unstable using the Butler-Volmer boundary condition for the anode a constant potential, $\phi_e = 0$, is applied for Eq. 1.11 at the anode surface. The salt flux is uniformly set to the average value:

$$-D_{\text{eff}} \nabla c_e \cdot \hat{n} = -\frac{1 - t_0^+}{\epsilon} j_{ave} \tag{1.18}$$

where $\hat{n}$ is the unit normal to the anode surface and j_{ave} is the average current density. This alternative boundary condition is a justifiable approximation because the kinetics of the semi-solid electrode are of primary interest, not the kinetics of the

Parameter	Symbol	Value	Source
Suspension electronic conductivity	σ	1 mS/cm	Ref. [32]
System temperature	T	298 K	
Electrolyte transference number	t_+^0	0.38	Ref. [39]
Butler-Volmer exponent	α	1/2	

Table 1.1: Values of model parameters used throughout work.

lithium foil anode.

Model and Solver Parameters

The COMSOL Multiphysics software is used to implement a finite element numerical solution of the model described above. The simulated region is discretized using a tetrahedral mesh with elements of maximum side length 50 μm. Linear Lagrange elements are used for all variables. Approximately 1.3 million elements are present in the complete mesh. Each simulation step is run until the nonlinear solver converges to a relative tolerance of 10^{-5}.

For each simulation, the flow profiles described by Equation 1.4 are stored and the solution is used as input for the convection terms in Equations 1.7 and 1.9. Equations 1.5, 1.6, 1.7, and 1.9 are used to model electrochemical behavior in the semi-solid electrode region by solving for the four variables ϕ_e, ϕ_s, c_e, and c_s as well as the applied potential ϕ_{applied}. Equations 1.11 and 1.12 are solved for ϕ_e and c_e in the separator region. Because the model is strongly non-linear, the computational time required to obtain a steady-state solution depends on the quality of the *a priori* initial conditions. Time-dependent simulations are run starting from a uniform salt concentration and state of charge distribution for a time corresponding to $2\tau_{\mathrm{flow}}$, and the result is used as the initial condition for the steady-state solution.

Table 1.1 presents the values for the model parameters used in the simulation. Valoen and Reimers [39] measured transport properties of an electrolyte containing $LiPF_6$ in a mixture of propylene carbonate, ethylene carbonate, and dimethyl carbonate as a function of salt concentration and temperature, and their results are used for κ and D in Eqs. 1.13 and 1.14. The simulations utilize an exchange current density

of the form

$$i_0^{\text{LCO}} = k_p c_s^\alpha c_e^\alpha \tag{1.19}$$

with $k_p = 6.2 \times 10^{-10} \text{mol}/(\text{m}^2\text{s})$ as reported by Zhang, Guo and White [38].

1.3 Effect of Pumping Power Losses on Viable Modes of SSFC Operation

As mentioned in Section 1.1.3, the semi-solid electrode suspensions used in SSFCs are quite viscous, on the order of 1000 cP compared to 1 cP for water. This high viscosity leads to much higher pumping losses than are seen in conventional redox flow batteries, and therefore alternative modes of operation must be considered for SSFCs to achieve efficient performance. Conventional redox flow batteries are typically operated in a two-tank configuration with constant flow of the electrolyte so that the change in state-of-charge (SOC) during a single pass through the power stack is $\approx 10\%$ [13]. This helps prevent shunt currents by maintaining a relatively even SOC throughout the system. However, two alternative modes of operation using a four-tank configuration are possible. The first is stoichiometric flow operation. During stoichiometric flow the electrolyte is pumped continuously at a slow flow rate so that 100% of the SOC is utilized in a single pass through the power stack. The second is intermittent flow operation, in which charge and discharge is performed while the semi-solid electrode is not flowing, and pumping is performed in between charge or discharge cycles to bring fresh material into the power stack.

A preliminary analysis of pumping energy losses was performed using Star-CCM+ software to model steady state flow through the cell described by Duduta *et al.* of a 22.4% LCO and 0.6% Ketjen carbon black suspension. Fitting the power-law viscosity function described in Section 1.2.1 to experimental viscosity data for this suspension yields a coefficient $C = 7.41505\text{Pa} \cdot \text{s}$ and an exponent $n = 0.130188$. The pressure gradient needed to drive flow through the tubing at several different flow rates was obtained from the CFD simulations and was used to calculate the power needed to

Flow Rate (mL/min)	$P_{continuous}$ (mW)	$E_{circulate}$ (mJ)	Continuous flow loss (%)	Intermittent flow loss (%)
15	2.36	3.78	22.06	0.60
10	1.41	3.38	13.18	0.54
5	0.63	3.01	5.89	0.48
1	0.10	2.39	0.93	0.38

Table 1.2: Pumping energy losses as a function of flow rate for both continuous and intermittent flow modes.

drive the flow continuously through 20 cm of tubing, $P_{continuous}$, as well as the energy needed to circulate the suspension through 20 cm of tubing a single time, $E_{circulate}$ [12].

$$P_{continuous} = \frac{\partial P}{\partial x} \cdot 20cm \cdot Q \qquad (1.20)$$

where $\frac{\partial P}{\partial x}$ is the pressure gradient and Q the flow rate.

$$E_{circulate} = \frac{\partial P}{\partial x} \cdot 20cm \cdot V_{20} \qquad (1.21)$$

where V_{20} is the total suspension volume contained in 20 cm of tubing. By comparing the resulting values with the 10.7 mW discharge power obtained during continuous flow operation and 1.26 J of energy storage in the suspension contained in 20 cm of tubing the losses for continuous and intermittent flow operaton are computed. The results are presented in Table 1.2.

Based on these calculations, which are done for a suspension with relatively low loading of both carbon and active material (and therefore relatively low viscosity), continuous flow losses can be upwards of 20% of the energy stored in an SSFC system. This is unacceptably high for a practical energy storage system, as a result either intermittent or stoichiometric flow will be the operational mode of choice for a practical SSFC system. Therefore, much of the work in this thesis is focused on addressing issues important to either stoichiometric or intermittent flow that are less important for conventional redox flow batteries operating at a high continuous flow rate.

Chapter 2

Active Material Selection for Stoichiometric Flow Operation

2.1 Motivation

There have been two basic architectures for flow batteries. The earliest designs had four external tanks [40]: during discharge, two tanks containing fresh aqueous electrolytes were pumped into the stack and then the depleted fluids were stored in separate tanks. During charge, the flow direction and electrode polarity was reversed. Subsequent designs have two tanks—one for each aqueous electrolyte—in which the state-of-charge (SOC) is changed continuously by utilizing a fluid flow-rate that is fast compared to the rate at which power is extracted. These two architectures illustrate two extremes in operating mode: total SOC depletion in a single pass of the fluids through the stack (four-tank), and incremental SOC depletion (two-tank). The single-pass/four-tank design has the advantage of lower pressure $\times$ volumetric flow energy dissipation, but as is shown, may give rise to additional dissipative currents due to in-plane SOC gradients within an electrode. The multiple-pass/two-tank design eliminates these "shunt currents" at the expense of more mechanical dissipation.

There are two important time scales that characterize the operating modes of a flow battery, τ_{charge} and τ_{flow}. τ_{charge} is the time required to charge a single volume of the semi-solid electrode material contained within the active stack, and for a rect-
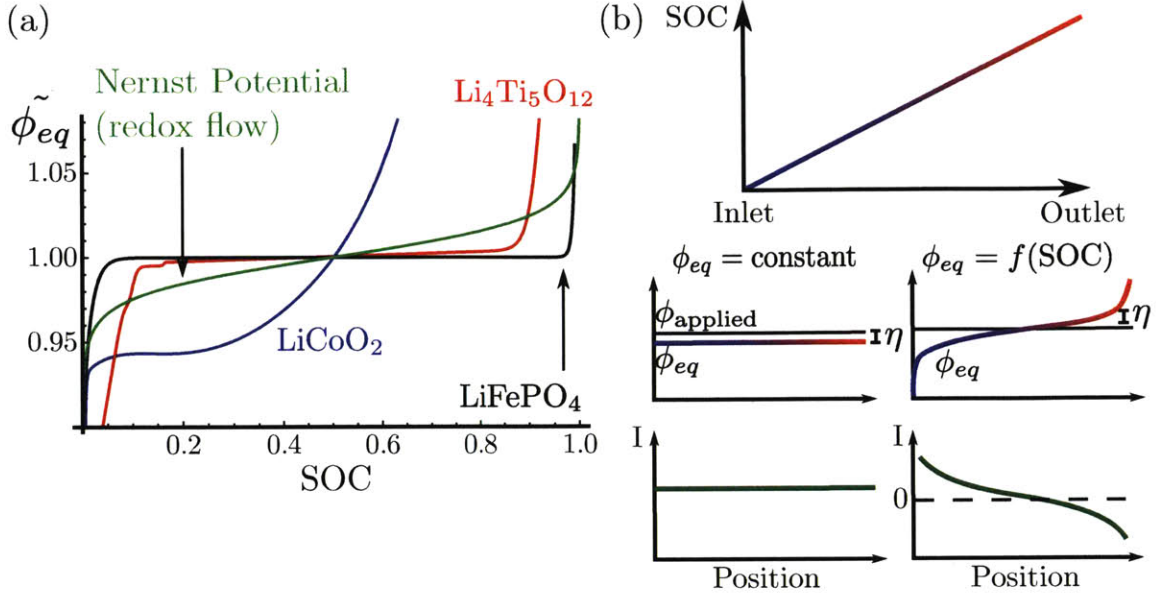
Figure 2-1: Comparison of the equilibrium voltages of several Li-ion storage compounds and conventional aqueous flow battery systems as a function of state of charge. b) Depiction of how a ϕ_{eq} function that varies with SOC leads to non-uniform current density distributions in stoichiometric operation

angular cross-section flow channel of width δ and length ℓ, $\tau_{charge} = (\delta^2 \ell \kappa_V \phi_{eq})/P$ where κ_V is the volumetric charge storage capacity of the semi-solid electrode, ϕ_{eq} is the equilibrium voltage, and P is the power being extracted from the cell. τ_{flow} is the residence time of a fluid volume in the active cell stack, given by $\tau_{flow} = (\delta^2 \ell)/Q$ where Q is the semi-solid electrode's volumetric flow rate. The dimensionless ratio $\tau^* = \tau_{charge}/\tau_{flow}$ determines the relative importance of electrochemical and flow effects. During high flow-rate operation (when $\tau^* \gg 1$) flow effects dominate and act to homogenize the semi-solid electrodes' charge-state. As κ_V and ϕ_{eq} are increased and the flow rate is decreased, τ_{charge} approaches τ_{flow} so $\tau^* \approx 1$, whereupon considerations of heterogeneous state-of-charge within the cell become more important. Such considerations are particularly relevant to SSFCs since a principal advantage of the approach is the ability to provide volumetric capacities an order of magnitude or more above that of the aqueous chemistries [12]. An additional cause of heterogeneity is that the equilibrium voltage, ϕ_{eq}, is generally not constant over a system's full SOC range. As our results demonstrate, differences between $\phi_{eq}(SOC)$ functions are

expected to play an important role in battery performance.

Conventional redox flow batteries that use aqueous redox solutions are limited to < 2 V cell voltage and ≈ 40 Wh/L energy-density based on solubility and electrolysis limitations [13]. Their voltage versus state of charge functions, $\phi_{eq}(SOC)$, are monotonically varying, corresponding to a Nernstian dependence of voltage on reactant concentration. The innovation of Duduta et al. [12] is a flow battery that combines the high energy-density of rechargeable batteries using solid storage electrodes with the architecture advantages of redox flow batteries. SSFCs of the lithium-ion type (other semi-solid chemistries can also be adopted) utilize flowable mixtures of solid Li-ion storage compound particles suspended in a liquid non-aqueous electrolyte. The semi-solid electrode suspension is made electronically conductive by co-suspending nanoscale conductive particles (e.g., carbon black) along with storage compound particles in the electrolyte. In SSFCs, conductive particle networks replace the static current collectors (e.g., carbon felt) used in conventional flow batteries. Depending on the choice of storage material, the solids fraction of the suspension, and the cell voltage of the electrochemical couple, a 20-30 fold increase in the energy density of the flow electrodes (e.g., catholyte + anolyte) over aqueous redox chemistries is conceivable [12]. The increased energy density also permits a slower volumetric flow rate at the same power; however, the viscosities are significantly higher and the suspension rheology is generally non-Newtonian.

The fundamental design and operational challenge in any flow battery system is determining the optimal flow and charge/discharge rates for operation. Since fast flow rates ($\tau^* \gg 1$) increase pumping dissipation, while low flow rates ($\tau^* \approx 1$) may give rise to shunt currents, conventional flow batteries with low-viscosity (≈ 1 cP) aqueous electrolytes use fast flow. In contrast, the particulate suspensions used in SSFCs are significantly more viscous (≈ 1000 cP), so minimizing pumping losses by operating with slow flow is important. Pumping-energy dissipation is reduced by operating in stoichiometric flow mode ($\tau^* = 1$) where the charge and flow rates are matched such that material is fully charged or discharged in a single pass through the reaction stack. This both minimizes the pressure drop needed to drive the flow and the total

displacement of fluid since each unit volume of active material passes through the cell only once per usage cycle. Because the state of charge at the stack inlet and outlet differ greatly in low flow rate operation, a four tank system is preferred.

However, stoichiometric flow produces a variation of SOC along the length of the flow channel. If the ϕ_{eq}(SOC) function is not a constant, then these gradients in SOC correspond to gradients in ϕ_{eq}. Assuming low current collector resistance such that the electrical potential in the current collector is constant along the entire flow channel, gradients in ϕ_{eq} correspond to gradients in the overpotential that is applied to the redox medium. This in turn causes a variation in the current density along the channel. (An early model of the Zn-Br flow battery system by Lee and Selman [41] addresses a different non-uniformity in current distribution along the flow channel that is due to concentration polarization.) Avoiding current density nonuniformities is another reason aqueous flow batteries are often operated at high flow rates [13]. Correspondingly, previous models have generally assumed that the current density is spatially uniform along the channel; this assumption appears in the recent models for vanadium redox and soluble lead-acid flow batteries by Shah *et al.* [42, 43]. Here this assumption is relaxed and furthermore it is shown that the selection of electrochemically active materials based on their ϕ_{eq}(SOC) can reduce or eliminate spatial current non-uniformities. The basic concept is illustrated in Fig. 2-1. The equilibrium potential vs. state-of-charge (SOC) of solid storage compounds such as those developed for rechargeable lithium batteries offers a wide range of behavior. Some, such as LCO have an equilibrium potential that varies continuously with state-of-charge, not unlike the aqueous electrolyte solutions used in conventional flow batteries. This is indicative of a continuous solid solution of the working ion across the SOC range. Others, such as LFP and $Li_4Ti_5O_{12}$ (LTO), have a flat potential vs. SOC curve due to two-phase co-existence that pins the lithium chemical potential at a constant value. In some compounds, solid solution behavior occurs over one SOC range and fixed-potential behavior over another. By selecting cathode and anode materials that together provide a relatively flat cell voltage vs. SOC, it is possible to maintain a spatially uniform current density along the flow cell while still taking

37
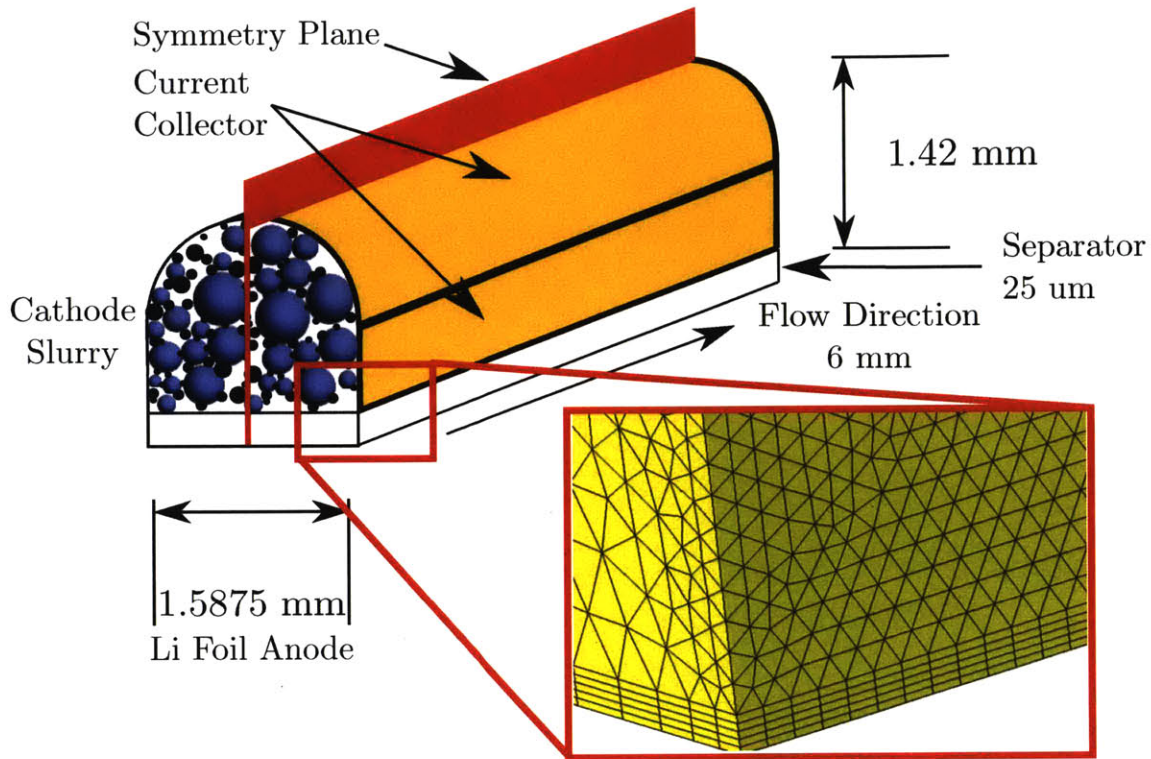
Figure 2-2: Depiction of the channel geometry used for the modeling work in this chapter. A portion of the computational mesh used is also shown.

advantage of the low mechanical dissipation of the stoichiometric flow mode.

2.2 Model Setup

2.2.1 Geometry and Mesh

The simulations run in this chapter all adopt the half-flow cell geometry used for the experiments reported in Duduta et al. [12]. This flow channel geometry is depicted in Fig. 2-2. In order to reduce the computational requirements for these simulations the computational domain is split in half by the symmetry plane parallel to the flow direction, as depicted in Fig. 2-2. In addition, the computational domain only extends for 6mm along the flow direction. The modeled volumetric flow rate is correspondingly reduced to match the shorter channel length.

The computational domain is meshed using the COMSOL Multiphysics software.

A tetrahedral mesh is used for the semi-solid cathode region with a maximum element size of 50 μm. In order to resolve steep gradients near the channel inlet the mesh is locally refined there, with a maximum element size of 10 μm on the inlet boundary. Similarly, the mesh is refined to a maximum size of 20 μm on the current collector boundary. The triangular mesh present on the interface between separator and semi-solid cathode regions is used as the basis for a swept mesh in the separator region. Five elements parallel to the sweep direction were found to be sufficient to resolve the gradients in the separator region. A portion of the computational mesh near the channel inlet region is shown in Fig. 2-2, and the transition from a tetrahedral to swept mesh is apparent at the cathode-separator interface. The local refinement of the mesh on the current collector boundary is also evident.

2.2.2 Model and Solver Parameters

The values of parameters used for the simulations in this chapter are listed in Table 2.1. Parameters not listed use the same values as given in Table 1.1. The equilibrium voltage functions used for the LCO and LFP simulations are both taken from the literature. For the LCO simulations the equilibrium voltage function suggested by Doyle and Fuentes is used:

$$V_{eq}^{LCO}(Q) = B_1 + B_2 Q + B_3 Q^2 + B_4 Q^3 + B_5 Q^4 + B_6 Q^5 + B_7 \exp\left(-B_8 Q^{B9}\right) \quad (2.1)$$

where $Q = 1 - x_{Li}$ is based on a theoretical capacity of 274 mAh/g [37]. For the LFP simulations a fit to the data presented by Srinivasan and Newman is used:

$$\begin{aligned}
V_{eq}^{LFP}(x_{Li}) =&\, 3.42715 + \exp\left(-\frac{x_{Li} + 0.00742855}{0.00500267}\right) \\
&- \exp\left(\frac{x_{Li} - 1.00844}{0.0156781}\right)
\end{aligned} \quad (2.2)$$

where x_{Li} is the fraction of intercalated Li based on a theoretical capacity of 0.02095 mol/cm^3 (155 mAh/g) [44].

Parameter	Symbol	Value	Source
Viscosity coefficient	C	13.1238 Pa·s	Ref. [12]
Viscosity exponent	n	0.192876	Ref. [12]
Electrolyte volume fraction	ϵ	0.7	
Electrolyte volume fraction in separator	ϵ_{sep}	0.5	
Inlet salt concentration	c_e^{inlet}	1600 mol/m^3	
Inlet intercalated lithium concentration	c_s^{inlet}	0.9 c_{max}	
LCO V_{eq} coefficients	B_1	3.855 V	Ref. [37]
	B_2	1.247 V	
	B_3	-11.152 V	
	B_4	42.818 V	
	B_5	-67.711 V	
	B_6	42.508 V	
	B_7	-6.132 V	
	B_8	-7.657	
	B_9	115.0	

Table 2.1: Model parameter values used for stoichiometric flow modeling simulations

2.3 Results

2.3.1 State of Charge and Current Density Distributions

Figure 2-3 shows a comparison of the steady-state SOC (where SOC, state of charge, is defined as 1-x_{Li} where x_{Li} is the fraction of occupied lithium sites) and current-density distributions for two SSFC cathode active particles: LiCoO$_2$ (LCO) and LiFePO$_4$ (LFP). Each simulation models a C/20 charge rate at stoichiometric flow rate for a suspension containing 30% active particles.

For the LCO case, where ϕ_{eq} only plateaus over a small range of SOC between 0.7 and 1.0, Figure 2-3 shows that the current-density is highly concentrated near the inlet where the incoming uncharged material has a lower ϕ_{eq} and the overpotential is at its maximum value. Additionally, the state of charge plot shows that the LCO reaches a maximum of SOC $\approx$ 0.4 (where SOC is defined as SOC $= 1 - x$ for Li$_x$CoO$_2$, and does so prior to the midpoint of the channel. Full utilization of the theoretical 155 mAh/g capacity corresponds to SOC $\approx$ 0.57; thus, the LCO system is only able to access 70% of its theoretical capacity when operating in stoichiometric flow mode.
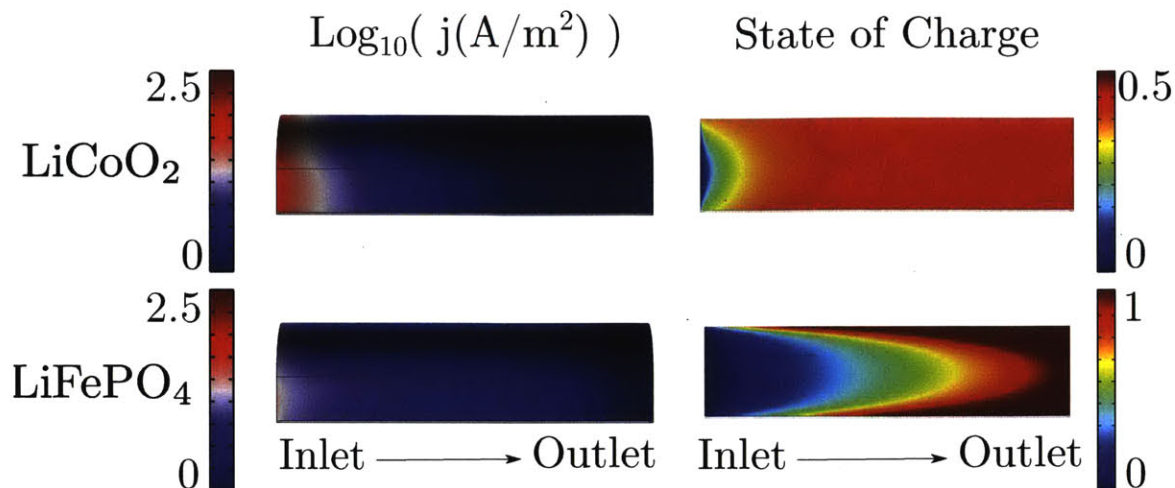
Figure 2-3: Comparison of the steady state current density and state of charge distribu- tions along a flow channel in an SSFC using $LiCoO_2$ active particles and one using $LiFePO_4$ active particles. Both systems are charging in stoichiometric flow mode at C/20 rate. Current density images depict a projection of the current collector inter- face, while state of charge images are taken on the midplane of the channel. Note that complete charging of $LiCoO_2$, corresponding to 0.57 SOC (155 mAh/g capacity), is never reached. In contrast, $LiFePO_4$ uniformly reaches complete SOC at steady state. See text for details.

The extraction of charge current is also highly inefficient, with the current density being below 0.1 mA/cm^2 over about 50% of the current collector length downstream of the inlet. This current density corresponds to a C/115 rate. The non-uniformity in the current density distribution may also introduce undesirable thermal effects since the *IV* power losses are concentrated over a narrow region close to the inlet. Ultimately these inefficiencies combine to give a steady state charge voltage of 4.15 Volts. A simulation of steady state discharge at the same current and flow rates results in a voltage of 3.89 Volts, corresponding to voltage efficiency of 93.7%. Defining the average polarization as half the difference between the charge and discharge voltages gives 0.13V.

In contrast, the LFP model system exhibits more efficient behavior. The current density is not perfectly uniform, particularly near the channel outlet where ϕ_{eq} rises sharply as the material approaches full charge, but it is much more uniform than in the LCO case. The maximum current density for the LFP system is 2.24 mA/cm^2, only 4
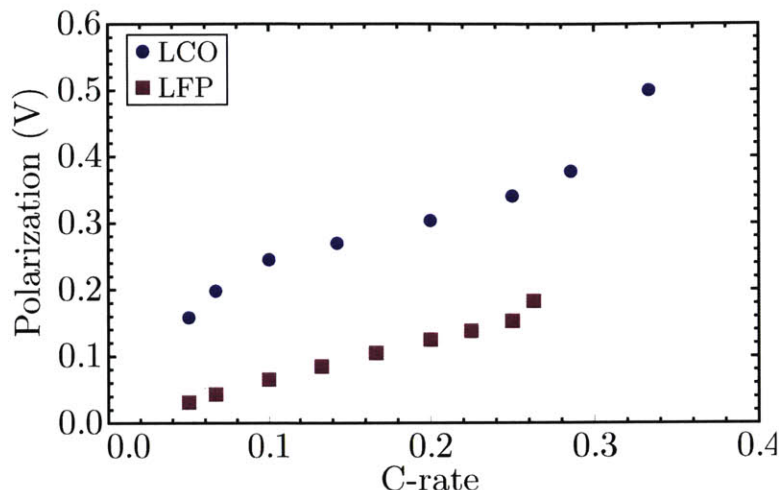
Figure 2-4: Comparison of the scaling of polarization with C-rate for LCO and LFP SSFCs undergoing stoichiometric charging. The inflection point near C/4-C/5 in each curve is caused by growing salt concentration gradients reducing the average ionic conductivity of the electrolyte. Total salt depletion at the anode occurs near C/3-C/4 for both LCO and LFP systems in the modeled channel geometry, leading to simulation divergence at higher rates.

times larger than the average current density. (The maximum current density in the LCO case is 17.8 mA/cm^2, about 30 times greater than the average value.) Similarly, the state of charge gradients in the LFP system are more broadly distributed than in the LCO case, corresponding to more uniform charging of the active particles. At the outlet, the LFP material uniformly reaches its theoretical capacity under equivalent flow and galvanostatic conditions to the LCO case. (The entry gradient would be even further reduced if the entering material is slightly charged so that ϕ_{eq} is closer to the plateau value.) These differences in current density distribution and state of charge gradients combine to result in a potential of 3.47V on charge and 3.39V on discharge at the same current and flow rate, corresponding to voltage efficiency of 97.7%. The polarization for the LFP system is 0.04V, only 30% of the value for the LCO case running at the same C/20 rate in stoichiometric mode.

This difference in polarization becomes more pronounced as the current and flow rate increase. Figure 2-4 depicts the scaling of the polarization with increasing C-rate for LFP and LCO SSFCs during stoichiometric charging. Polarization values are calculated based on the calculated voltage from steady-state charge simulations

and the midpoint voltage of the C/20 steady-state charge and discharge simulations. The LFP active material system is predicted to to exhibit lower polarization at all simulated rates, and the polarization grows faster with rate for the LCO active material SSFC. Both polarization curves exhibit an inflection point around C/4-C/5 rate, this results from growing salt concentration gradients that decreases the ionic conductivity of the cell and therefore increase the rate of polarization growth. The electrolyte ionic conductivity function exhibits a peak conductivity of 12 mS/cm near 1 M concentration, falling off to $\approx$ 1 mS/cm as the salt concentration increases to 4.5 M or falls to 0 M. As a result the growing salt concentration gradients reduce the average ionic conductivity of the electrolyte leading to increasing ohmic losses in the electrolyte phase and a faster increase in the total cell polarization. Above $\approx$ C/3-C/4 rate both the LCO and LFP systems exhibit total salt depletion at the anode in the modeled channel geometry, leading to simulation divergence when attempting to model higher rates.

2.4 Discussion

2.4.1 Comparison to 1D scaling model

The simulations thus demonstrate the effects of $\phi_{eq}(SOC)$ on flow battery operation: the variation of state of charge—therefore variation in the voltage—along the flow channel is proportional to the slope of $\phi_{eq}(SOC)$. An analysis of the simple model suggested in Fig. 2-1b qualitatively agrees with the steady state results from the full model in Fig. 2-3, and provides some useful scaling relations.

In this simple model, consider an idealized chemistry where the equilibrium potential varies linearly with state of charge with slope a, $\phi_{eq}(SOC) = aSOC + \phi_0$. Treating the system as 1 dimensional with length L and linear flow rate v gives:

$$\frac{\partial SOC}{\partial t} = \frac{j}{\kappa_L} - v\frac{\partial SOC}{\partial x} \tag{2.3}$$

where j is the local current per unit length, and κ_L is the semi-solid electrode capacity

43

per unit length. Assuming j varies linearly with the overpotential, η, and that the system is at steady state yields:

$$0 = \frac{k(\eta_0 - aSOC)}{\kappa_L} - v\frac{\partial SOC}{\partial x} \tag{2.4}$$

Solving this ODE with the boundary condition $SOC(0) = 0$ results in:

$$SOC(x) = \frac{\eta_0}{a}\left(1 - \exp\frac{-kax}{\kappa_L v}\right) \tag{2.5}$$

which leaves η_0 as an undetermined variable. η_0 may be determined by integrating the current density along the length of the cell and equating it to the total applied current. Finally using the dimensionless length $\tilde{x} = x/L$ yields:

$$
\begin{aligned}
SOC(x) &= \frac{I}{\kappa_L v}\frac{\exp\left(\frac{akL}{\kappa_L v}(1 - \tilde{x})\right)\left(\exp\left(\frac{akL}{\kappa_L v}\tilde{x}\right) - 1\right)}{\exp\left(\frac{akL}{\kappa_L v}\right) - 1} \\
&= \frac{1}{\tau^*}\frac{\exp\left[B(1 - \tilde{x})\right]\left(\exp[B\tilde{x}] - 1\right)}{\exp(B) - 1}
\end{aligned} \tag{2.6}
$$

where $I/(\kappa_L v) = 1/\tau^*$ and the second dimensionless group is $B = akL/(\kappa_L v)$. Recall that τ^* is the ratio relating the time required to charge a volume of semi-solid electrode material and the time for the same volume to flow through the active stack region. When $\tau^* = 1$ the semi-solid electrode should charge in a single pass (stoichiometric flow), and as τ^* increases the expected SOC of the semi-solid electrode at the end of the active stack decreases. As seen in Fig. 2-5, τ^* limits the value of SOC at the outlet of the flow channel.

The physical significance of B is not as immediately clear as that of τ^*. It is the product of two terms: L/v, which is the residence time of the electrolyte in the active region, and a term ak/κ_L which represents an inverse time constant for current extraction. A high value of B therefore corresponds to steep gradients in SOC, as shown by Fig. 5. While these results are obtained by modeling a positive semi-solid electrode, the same general effects obviously apply to negative semi-solid electrodes. In any flow battery with two flowing electrodes, the $\phi_{eq}(SOC)$ of each can be inde-

44
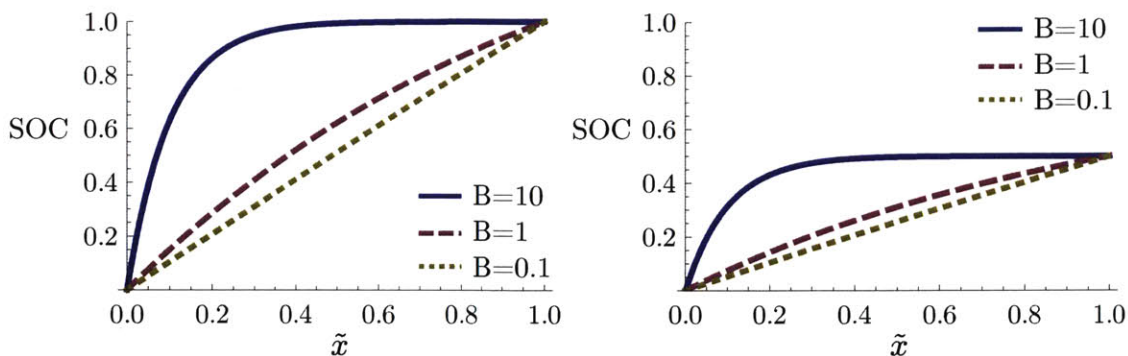
Figure 2-5: Steady-state SOC profiles as a function of dimensionless position x (x = 0 is the inlet, x = 1 is the outlet) as predicted by the one-dimensional scaling model. Curves are solutions to Eq. (19) for values of the dimensionless parameter B = 0.1, 1, and 10. * = 1 in (a) and * = 2 in (b). As B increases the steady state SOC profile becomes more non-linear.

pendently selected to obtain a ϕ_{eq}(SOC) for the cell of various shapes. By selecting a material that has a flat ϕ_{eq}(SOC) and utilizing electrochemical cycles with an SOC-swing that remains in the flat region of ϕ_{eq}(SOC), detrimental effects are mitigated. While these simulations were obtained for cathodes the conclusions obviously also apply to anodes within flat regions of their ϕ_{eq}(SOC). It would be advantageous to control the SOC swings in the flowing anode and cathode independently by altering the flow rates independently to balance capacity.

2.4.2   Implications for other flow battery systems

The modeling work performed in this chapter has focused on semi-solid flow batteries, however it is important to note that the general conclusions are expected to apply to other flow battery systems when operating in a low flow rate ($\tau^* \approx 1$) mode of operation. For any flow battery system where V_{eq} is a function of the state of charge (for example in conventional redox flow battery systems V_{eq} varies logarithmically with the concentration of active species according to the Nernst equation) a non-uniform current density distribution is expected to develop when τ^* is sufficiently small that the electrolyte undergoes a significant change in state of charge in a single pass through the power stack. Conventional redox flow batteries are largely able to

avoid this problem by operating at high flow rates ($< 10\%$ change in SOC in a single pass), however high flow rate operation may not be viable for new high energy density chemistries being considered for use in flow batteries that are more viscous than the conventional aqueous electrolytes.

For any novel flow battery chemistries where pumping losses are similar to the semi-solid suspensions focused on in this work it will be important to consider operating in either stoichiometric or intermittent flow mode to reduce losses. In order to effectively operate in stoichiometric flow mode new chemistries that have flat V_{eq} profiles, similar to LFP, are attractive. Additionally, for chemistries that are both viscous enough that they must be operated at low flow rates and exhibit large changes in $V_{eq}(SOC)$ there are two possibilities that may reduce the development of non-uniform current density distributions. The first is to flow the anode and cathode electrolytes in opposite directions so that highly charged cathode material (at a high V_{eq}) is paired with highly discharged anode material (also at a high V_{eq}) and highly discharged cathode material (at a low V_{eq}) is paired with highly charged anode material (also at a low V_{eq}). This could help to even out the average cell potential over the length of the flow channel and therefore minimize the non-uniformities that would otherwise develop in the current density distribution. The second possibility is to split the power stack into multiple regions that are electrically insulated from one another. Then each region of the stack could be at a different voltage, and the current drawn from each region could be varied to control the range of SOC present in each region. This approach is equivalent to operating at a higher τ^* in each region of the stack and using the multiple regions in series to enable low flow rate operation and approach $\tau^* = 1$ when considering the stack as a whole.

Chapter 3

Extended Electrochemically Active Zone (EAZ) Effects on Intermittent Flow Operation

3.1 Motivation

As discussed in Section 1.3, the high viscosity of the semi-solid suspensions used as the energy storage materials in SSFC systems limits the potentially viable operational modes in comparison to conventional aqueous flow battery systems with comparatively less viscous electrolytes. Chapter 2 focused on understanding the continuous stoichiometric flow mode, this chapter will address important considerations for operating a flow battery system in an intermittent flow mode. In particular, the goal of this chapter is to understand the extent of the electrochemically active zone (EAZ) in a SSFC power stack.

In a conventional redox flow battery the electrolyte solutions used as the energy storage medium are ionically conductive and act as the medium for ion transport as the electrochemical reaction proceeds within the power stack. However, these electrolytes are not electronically conductive, and therefore conventional redox flow batteries use a porous carbon mesh in either a flow-through or flow-by configuration

within the power stack. This porous carbon mesh provides electronic conductivity in the system, enabling transport of electrons from the external circuit to the interface with the electrolyte solution so that the electrochemical reaction can occur. In contrast, the semi-solid suspensions that serve as the energy storage medium in SSFC systems are mixed conductors; the liquid electrolyte solvent provides ionic conductivity and the network formed by the active storage compound particles and conductive additive particles that are co-suspended in the electrolyte provides electronic conductivity throughout the suspension [12]. Since the suspensions are mixed conductors, they effectively serve as liquid wires that transport both ions and electrons. In principle this suggests that at very slow charge or discharge rates the entire storage tank in an SSFC system is electrochemically active without any flow as a result of ion and electron transport through the suspension in the pipes connecting the storage tanks to the active power stack. This concept is depicted in Fig. 3-1. In practice, it is unlikely that an SSFC would be run at a rate slow enough for the entire storage tank to be involved in the electrochemical reaction, but it is probable that the EAZ will extend beyond the immediate power stack region (as defined by the location of the current collectors) and into the piping feeding the power stack. As a result it is important to understand the extent of this extended-EAZ region under practically relevant operating conditions.

The extended-EAZ region is expected to be most important for intermittent flow operation of SSFCs. During intermittent flow operation the electrode suspensions in an SSFC are charged or discharged while stationary, and pumping is performed intermittently to replace fully charged or discharged suspension with fresh material as depicted in Fig. 3-2. In order to operate effectively in an intermittent flow mode, it is important to know what volume of active suspension needs to be pumped into the active cell between charge or discharge operations. If too large a volume is moved during each pumping operation then some of the active suspension present in the system will be unutilized, effectively reducing the energy density of the SSFC system. On the other hand, if too small of a volume of suspension is moved then the power stack will contain suspension at different states of charge during electrochemical operation,

SSFC | Conventional Flow Battery

	Electronically Conductive
	Ionically Conductive
	Mixed Conductor (Electrochemical Reaction Possible)
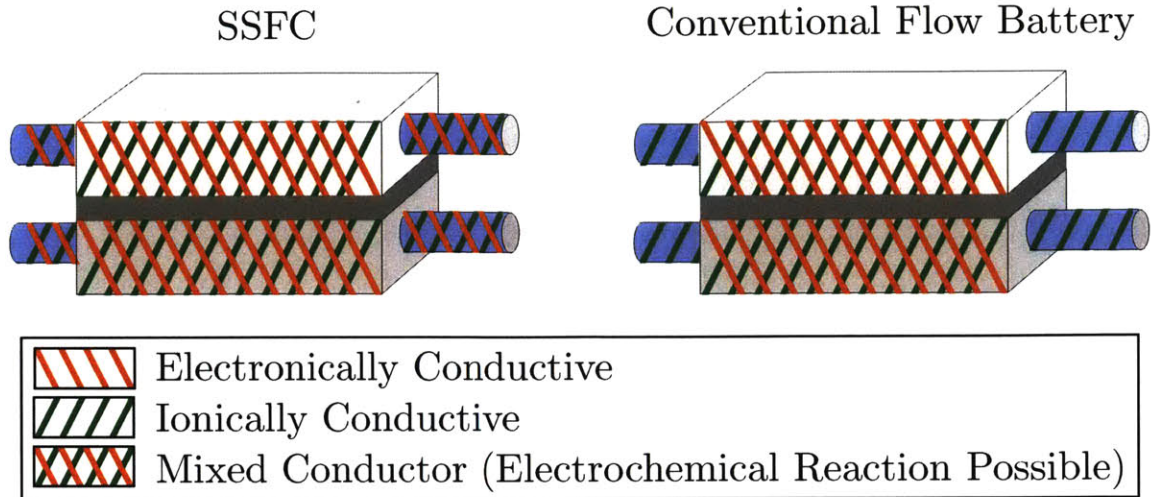
Figure 3-1: The semi-solid suspensions used in SSFC systems are mixed ionic and electronic conductors, and therefore provide a pathway for both ion and electron transport between the power stack and storage tanks in an SSFC system. In contrast, the electrolytes in conventional flow battery systems are only ionic conductors, and therefore the electrochemically active zone is confined to the power stack region where electronic conductivity is provided by a porous carbon mesh current collector.

which can negatively impact performance as seen in Chapter 2. Since it is expected that the EAZ will extend beyond the immediate power stack region in SSFC systems, it is important to characterize the size of this extended-EAZ to properly calibrate the volume of suspension to be pumped between charge or discharge operations during intermittent flow operation.

In addition to its importance for understanding how to operate SSFCs in intermittent flow mode, studying the extent of the extended-EAZ also provides an opportunity for model validation by comparison with experimental data. Comparing model results to experimentally tested voltage profiles obtained at various rates using the same cell geometry demonstrates that the porous electrode model used in this work successfully captures the relevant physics governing the electrochemical performance of SSFCs. Also, by varying the model parameters and observing the effects on the resulting predicted voltage profile it is possible to study the sensitivity of the model.

Intermittent Charge Process
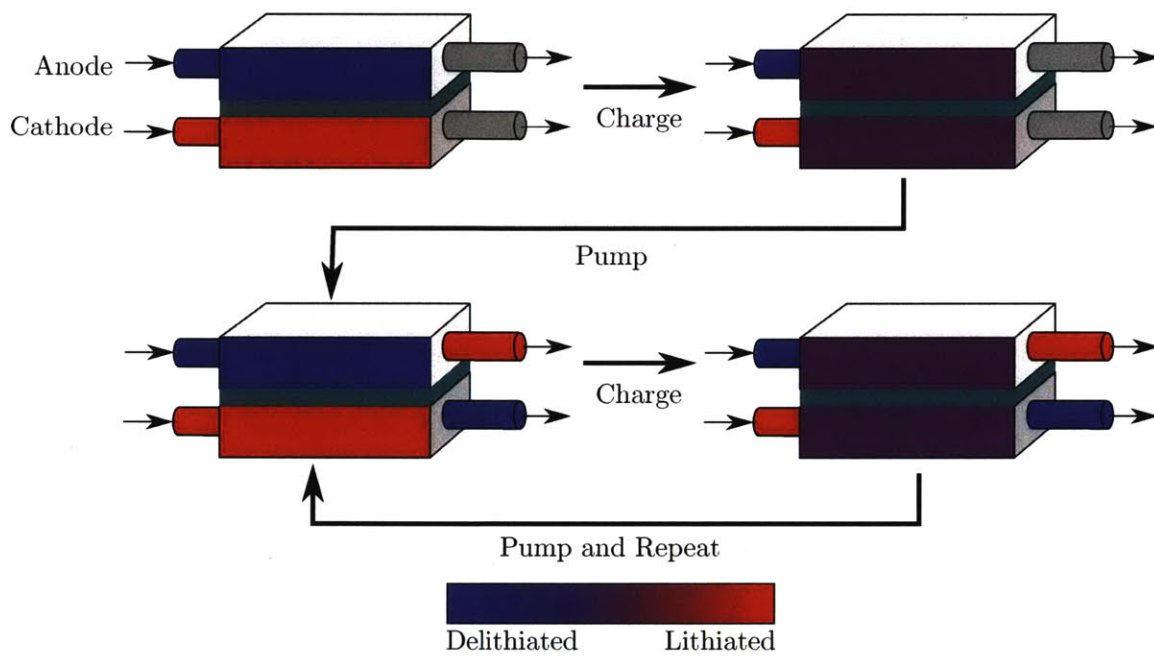
Figure 3-2: Schematic demonstrating intermittent flow operation of an SSFC. Active suspension is charged or discharged while stationary within the power stack region. Once the full capacity of a slug of material is utilized it is pumped out of the power stack and replaced with fresh suspension.

3.2 Model Setup

3.2.1 Experimental Comparison

One of the main goals of modeling the extended-EAZ is to use this work for model validation by comparison with experimental results. Therefore, it is important to understand the experiments that the model predictions are compared to. The simplest possible experiment to ascertain the size of the extended-EAZ region would be to cycle an SSFC suspension against a Li-metal anode and observe the usable capacity obtained from the system. Assuming that the extended-EAZ region is significant, one would expect to observe more capacity than expected based on the amount of active material in the active cell region and its theoretical capacity. This greater than theoretical capacity effect was commonly seen in early experimental testing of SSFC suspensions, however there are a number of alternative possible explanations for the data. For example, electrolyte evaporation could lead to a higher volume fraction of active storage material in the suspension than expected, and therefore a larger volumetric capacity. Therefore, simply cycling SSFC suspensions in a single cell geometry is insufficient to understand the extent of the EAZ.

Dr. Yajie Dong recently developed a new cell design for use in SSFCs where the bulk of the cell is composed of non-conductive PVDF, with the current collector region consisting of a thin layer of gold sputtered onto the PVDF flow channel [45]. Since this cell design uses sputtering to deposit the gold current collector, it is trivial to control the amount of the flow channel that the current collector is formed on by masking off a portion of it during the sputtering procedure. This innovation provides the basis for our experimental design intended to measure the size of the extended-EAZ region.

The experimental design used to study the extended-EAZ is depicted in Fig. 3-3. The basis for this design is the assumption that the size of the extended-EAZ region depends on the average charge or discharge rate applied to the suspension in the active cell, but not on the total current applied to the cell. Therefore by electrochemically cycling SSFC suspensions of the same composition at the same average rate, but in cells with progressively shorter lengths of sputtered gold current collector it

51
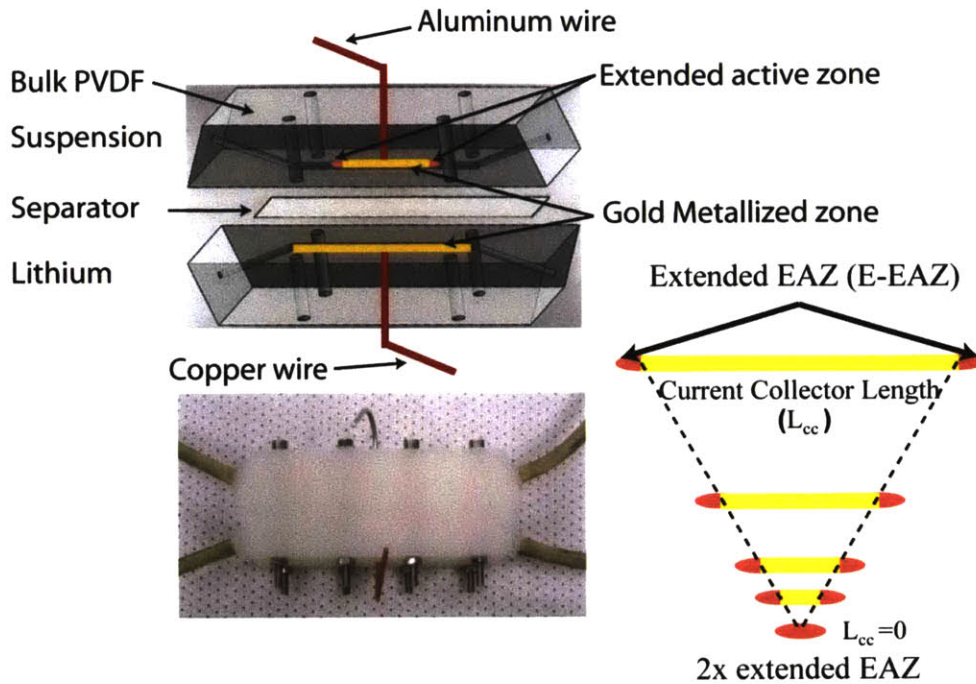
Figure 3-3: Experimental setup for measuring extent of EAZ. Figure courtesy of Dr. Yajie Dong. E-EAZ size will be extrapolated based on the scaling of capacity with current L_{CC}.

should be possible to extrapolate the amount of capacity used in the extended-EAZ region from the y-intercept of a plot of total usable capacity as a function of current collector length, L_{cc}. This experimental design controls for uncertainty in suspension composition since the theoretical capacity of the suspension used is irrelevant for determining the extended-EAZ size from the experimental results.

3.2.2 Current Collector Interfacial Resistance

In order to obtain good agreement with experimental data, it was determined that the model must incorporate an interfacial resistance at the boundary between the semi-solid suspension and the current collector. Incorporating this interfacial resistance requires some slight modifications to the equations and boundary conditions described in Section 1.2.2. In addition to the semi-solid cathode and separator regions, the current collector region is now also modeled explicitly rather than solely as a boundary condition. The only relevant variable within the current collector region is the solid

phase potential, ϕ_s, which follows Ohm's law:

$$\nabla \cdot (\sigma_{CC} \nabla \phi_s) = 0 \tag{3.1}$$

where σ_{CC} is the electronic conductivity of the gold current collector material. A constant surface resistance boundary condition is then applied to the interface between the semi-solid cathode and current collector volumes:

$$\phi_s^{CC} - \phi_s^{Cathode} = \rho_s(\hat{n} \cdot \vec{j}) \tag{3.2}$$

where $\phi_s^{CC} - \phi_s^{Cathode}$ is the potential drop across the interface, ρ_s is the surface resistance in $\Omega \cdot m^2$, $\hat{n}$ is the unit normal to the interface, and $\vec{j}$ is the local current density. Finally, the constant total current (but not constant current density) boundary condition described by Equation 1.15 is applied at the external boundary of the current collector volume.

3.2.3 Geometry and Mesh

In order to properly compare model predictions to experimental results, a Solidworks model of the cell geometry used in the experimental EAZ tests is used to create the computational domain for the simulations. This geometry is depicted in Fig. 3-4. The length of the current collector boundary is varied between simulations to match the particular experiment that is being modeled, but the Li-foil anode extends over the entire separator boundary in all cases, as in the experimental setup.

Each geometry is meshed using tetrahedral meshes in the semi-solid cathode regions. The triangular meshes on the cathode-separator and cathode-current collector interfaces are then used to generate swept meshes in the separator and current collector volumes. During the initial EAZ modeling work a single mesh was used for all time steps, an example of which is shown in Fig. 3-4. Within the volume of the cathode region adjacent to the current collector a maximum size of 40 μm is used in order to accurately model the sharp gradient between lithiated and delithiated LTO.
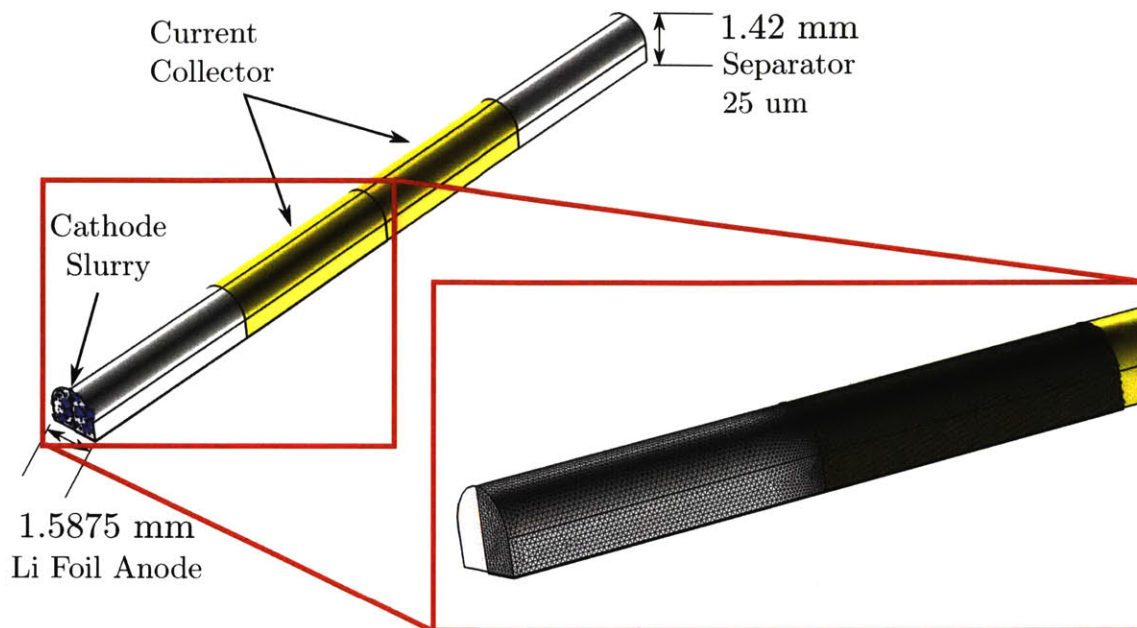
Figure 3-4: Schematic of the modeled geometry used for extended-EAZ simulations.

In order to reduce computational memory and processing time requirements a coarser mesh is used in the extended-EAZ region of the semi-solid cathode suspension. There a maximum tetrahedral element size of 100 μm is used, with an element growth factor of 1.05 to smoothly transition element sizes between the current collector and extended-EAZ regions. While this meshing procedure is effective for achieving successfully converged simulations, it leads to models with ≈ 2 million elements resulting in very long solution times on the order of 2-3 days for a single lithiation or delithiation. In order to reduce solution times while still obtaining accurate solutions the new time-dependent adaptive meshing feature from COMSOL v4.2 is used.

Time-Dependent Adaptive Meshing

The main challenge in meshing the modeled volume for extended-EAZ simulations is using a fine enough mesh to accurately capture the sharp boundary that develops between lithiated and delithiated LTO regions, while minimizing the total number of computational elements to achieve reasonable solution times. As seen in Fig. 3-5, the position of the boundary between lithiated and delithiated LTO regions moves

54

during the course of the cycling process. Ideally, a fine mesh would be used near the boundary location in order to accurately capture the steep gradients in c_s, with a much coarser mesh used away from that boundary where the gradients are significantly smaller. Unfortunately, this is not possible when using a single mesh to simulate a full lithiation-delithiation cycle. In order to accomplish this goal a time-dependent adaptive meshing procedure is used.

The time-dependent adaptive meshing procedure works by dividing a simulation up into several time intervals and using a different mesh for each interval. The particular mesh used for each time segment is generated dynamically by first simulating the time segment using a coarse mesh. The results of this coarse mesh simulation are then used to locally refine the mesh based on the local value of a user-specified error indicator function. Since the steepest gradient that needs to be captured in these simulations is the boundary between lithiated and delithiated region, the magnitude of ∇c_s is used as the error indicator function.

For all extended-EAZ simulations taking advantage of the time-dependent adaptive meshing procedure the interval length is determined based on the charge rate of the system being modeled. For each simulation the interval length between mesh refinements is given by $\tau_{\text{charge}}/10$, where τ_{charge} is defined as the total capacity in the current collector region divided by the applied current. The coarse mesh for the initial simulation of each time interval uses a tetrahedral mesh with maximum element size 200 μm in the semi-solid suspension region, with the resulting triangular meshes on the suspension-separator and suspension-current collector interfaces being swept outwards to discretize the separator and current collector volumes respectively. This coarse mesh results in $\approx$ 40000 elements depending on the particular current collector length being modeled. The coarse mesh is then refined based on the value of the error indicator function from the initial simulation until the total number of elements is increased by approximately a factor of 2.

Figure 3-5 depicts the resulting meshes used for an example simulation of a C/11 lithiation for a 12 mm current collector. It is clear in the figure that the mesh is locally refined near the boundary between lithiated and delithiated LTO suspension,

t = 10000 s

t = 30000 s

t = 45000 s

t = 50000 s

t = 60000 s

Delithiated   Lithiated
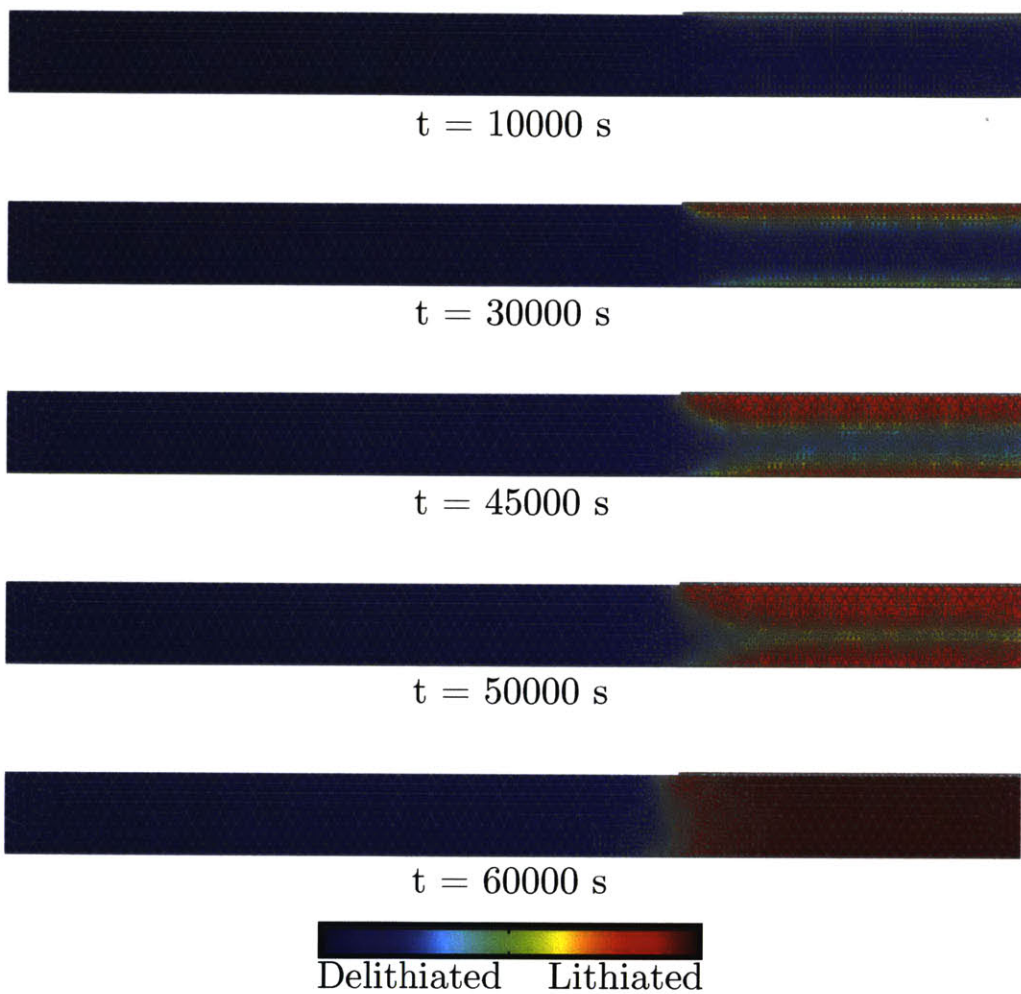
Figure 3-5: Meshes generated for a single extended-EAZ simulation demonstrating time-dependent adaptive meshing procedure. Images are from a C/11 lithiation for a 12 mm current collector. Mesh elements are outlined in gray and colored corresponding to the local intercalated Li fraction.

and that as this boundary moves during the lithiation process the mesh is refined with it. For this particular example, the time dependent adaptive meshing procedure generates refined meshes containing $\approx$ 220000 elements, in comparison using the single mesh procedure described earlier results in a mesh with 1.9 million elements. This reduction in the number of elements needed by nearly a factor of 10 results in simulation times on the order of 12 hours for the time-dependent adaptive meshing procedure compared to several days for the prior single mesh procedure.

3.2.4 Model and Solver Parameters

The values of parameters used for the extended-EAZ simulations are listed in Table 3.1. Parameters not listed use the same values as given in Table 1.1 The equilibrium voltage function used for LTO is taken from the work of Christensen, Srinivasan, and Newman:

$$
\begin{aligned}
V_{eq}(x_{Li}) =\, & 2.8441 - 1.3368 x_{Li} + 0.40438 \exp{-253.88 x_{Li}} \\
& - 0.14647 \tanh{36.507(x_{Li} - 0.03346)} \\
& - 0.0015515 \tanh{309.09(x_{Li} - 0.7982)} \\
& - 0.76112 \tanh{79.778(x_{Li} - 0.8658)} \\
& + (1.906 - 1.3224 x_{Li}) \tanh{79.554(x_{Li} - 0.86628)}
\end{aligned}
\tag{3.3}
$$

where x_{Li} is the fraction of intercalated Li based on a theoretical capacity of 174 mAh/g [46].

3.3 Results

3.3.1 Sample Time Evolution and Comparison to Experiment

Figure 3-6 depicts a comparison between the voltage profile predicted by the model to the experimentally observed voltage profile during lithiation at a C/11 rate with a

Parameter	Symbol	Value
Suspension electronic conductivity	σ	1 mS/cm
Electrolyte volume fraction	ϵ	0.8
Electrolyte volume fraction in separator	ϵ_{sep}	0.5
Initial salt concentration	c_e^0	1600 mol/m^3
Specific surface area	a_s	4.18 1/m
Initial intercalated Li concentration	c_s^0	$0.01 c_s^{theoretical}$
Exchange current density coefficient	k_p	0.042 A/cm^2
Current collector resistance	ρ_s	7.10 m$\Omega \cdot$ m^2

Table 3.1: Model parameters used for extended-EAZ simulations throughout this chapter.

6 mm current collector. Figure 3-6 also shows the time evolution of the intercalated Li fraction, x_{Li}, at several points in time that are labelled on the voltage profile. The predicted voltage profile matches reasonably with the experimental result, though the voltage plateau does end slightly earlier in the experiment and the slope of the tail region prior to reaching the voltage cutoff is shallower in the experimental data. The difference in the tail region slopes is explored more thoroughly in Section 3.3.3.

In both the experimental and modeled voltage profiles three distinct regions are evident: the initial voltage drop, the plateau region, and the tail region. By observing the evolution of x_{Li} at several points in each region of the voltage profile each can be correlated to different changes in the distribution of intercalated Li within the semi-solid electrode region. The initial voltage drop corresponds to the lithiation of the suspension within the current collector region up to the onset of the plateau in equilibrium voltage (V_{eq}) near $x_{Li} = 0.075$. Then during the plateau region of the voltage profile a "phase boundary" develops within the semi-solid electrode separating regions that are lithiated up to the end of the plateau in V_{eq} near $x_{Li} = 0.86$ and regions that remain near the onset of the plateau. As time passes the position of this "phase boundary" moves inwards towards the middle of the electrode volume. The existence of this "phase boundary" is a result of both the plateau in $V_{eq}(SOC)$ for LTO as well as the difference in the electronic and ionic conductivity of the suspension being used. The electronic conductivity of the modeled suspension is 1 mS/cm, while the ionic conductivity is $\approx$ 10 mS/cm at the initial electrolyte concentration of 1.6 M. The
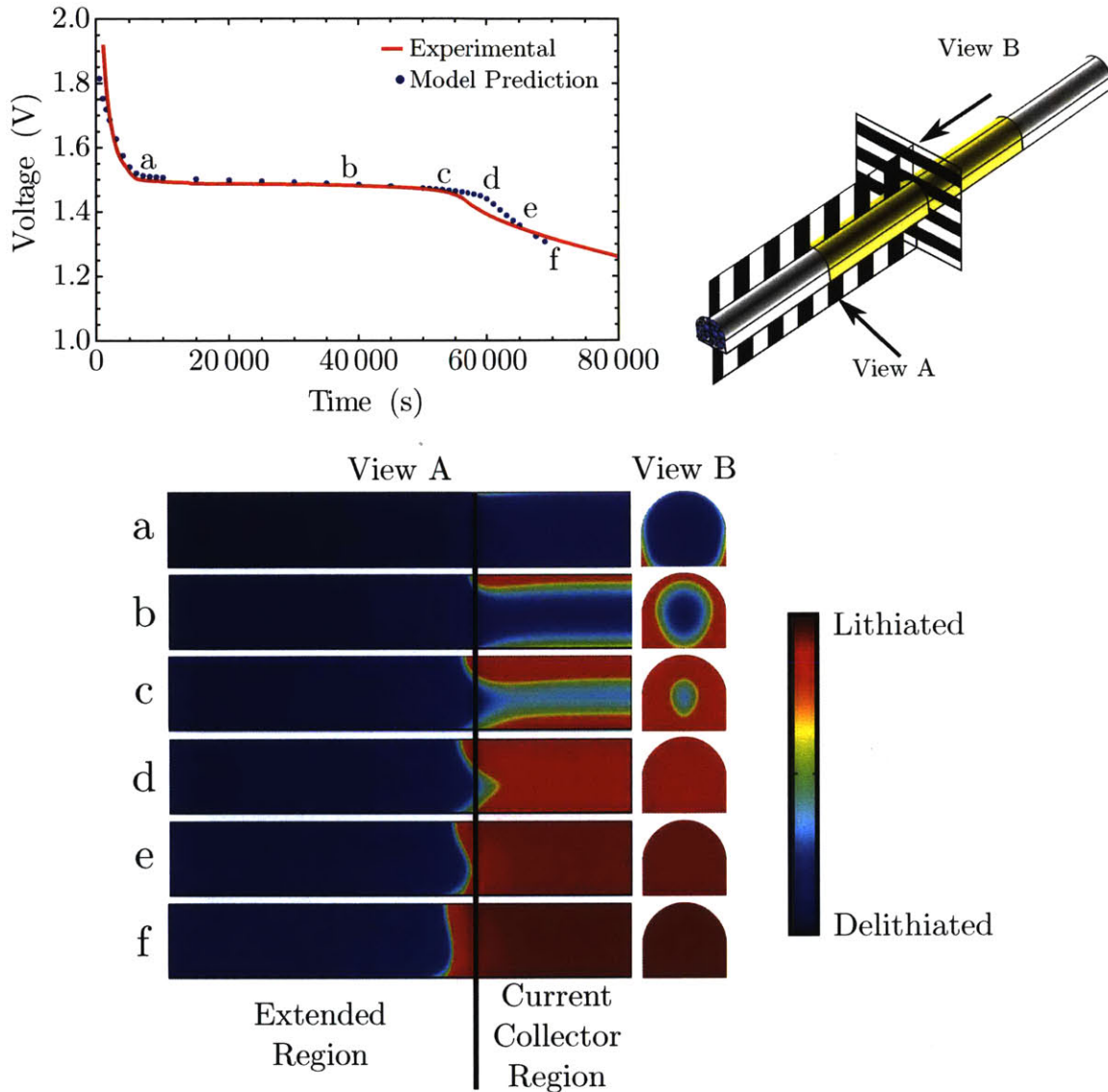
Figure 3-6: a) Comparison of experimental and modeled voltage profiles for an extended-EAZ experiment run at C/11 with a 6 mm current collector.

b) Time evolution of x_{Li} for the same simulated experiment. Two regimes are apparent, first the LTO capacity in the current collector region is filled to the end of the plateau region, then a "phase boundary" develops between lithiated and delithiated regions which moves progressively outwards into the extended region.

lower electronic conductivity leads to preferential lithiation near the current collector boundary to minimize the ohmic drop due to electronic current traveling through the semi-solid electrode.

The end of the plateau region of the voltage profile is reached once the majority of the active particles in the current collector volume are lithiated up to $x_{Li} \approx 0.86$. At this point the tail region of the voltage profile begins. During the tail region the applied voltage falls off linearly and the phase boundary that has developed between lithiated suspension in the current collector volume and delithiated suspension in the extended-EAZ region moves progressively outward. As this occurs the majority of the electrochemical reaction is happening at the location of the "phase boundary" and the primary change is the gradual increase in distance that electrons must travel from the current collector to the "phase boundary" position in order for the reaction to occur. Based on this information, it is possible to conclude that the slope of the tail region is controlled primarily by the electronic conductivity of the suspension used, as well as the total current being applied to the cell.

3.3.2 Evidence for Two Regimes of extended-EAZ

The observations made in Section 3.3.1 about the different regions of the observed voltage profiles, and the understanding of how they relate to changes in the distribution of x_{Li} within the active cell lead to a good qualitative understanding of an important phenomenon seen throughout the experimental tests of the extended-EAZ run by Yajie Dong. This phenomenon can be seen in Fig. 3-7, which shows the experimental voltage profiles for lithiation performed at C/11 rate using cells with different lengths of current collector. In this experimental data it is clear that the size of the tail region depends strongly on the length of the current collector used: for the 24mm and 47 mm cells only a short tail region is apparent in the voltage profile, whereas for the shorter 6 mm and 12 mm current collector cells the tail region is a significant fraction of the total capacity. This occurs because the slope of the tail region is a function of both the electronic conductivity of the suspension used and the *total* current applied to the cell. For the 24 mm and 47 mm current collector experiments

the voltage drop that results from all of the current traveling to the phase boundary in the extended-EAZ region where the electrochemical reaction could continue occurring requires applying a voltage lower than the cutoff voltage used. Therefore the lithiation process ends as the capacity within the current collector volume is filled and no significant tail region is observed in the voltage profile. In contrast, the 6 mm and 12 mm current collector experiments have lower *total* currents being applied, and therefore the "phase boundary" between lithiated and delithiated regions can move outwards into the extended-EAZ region a significant distance without reaching the cutoff voltage. This understanding is further supported when observing that the length of the tail region for the 6 mm current collector cell is roughly twice that of the 12 mm cell which is a result of the *total* applied current being half as large allowing the "phase boundary" to move approximately twice as far into the extended-EAZ volume before reaching the cutoff voltage.

Based on this understanding of the extended-EAZ behavior it is possible to conclude that the initial assumption which the experimental design is based on does not hold true. That is, the size of the extended-EAZ is not solely a function of the current *density* applied to a cell, it can also depend on the *total* current being applied. Therefore, one must conclude that there are two distinct regimes of extended-EAZ behavior that can be observed: a current *density* controlled regime (as observed for the 24 mm and 47 mm experiments which exhibit similar extended-EAZ capacity), and a *total* current controlled regime (as observed from the long tail regions seen in the 6 mm and 12 mm experimental data). Further evidence for this conclusion is seen in the results shown in Fig. 3-8.

Figure 3-8 compares the spatial distribution of intercalated Li from several simulations to demonstrate the existence of the current *density* and *total* current regimes of extended-EAZ behavior. On the left is a comparison between two simulations run at the same current density (C/11 rate) using different current collector lengths, showing the extent of lithiation at the end of the plateau in the voltage profile in each case. In each case a similar degree of lithiation is observed in the extended-EAZ volume of the cell, as is expected for the current *density* controlled regime based on
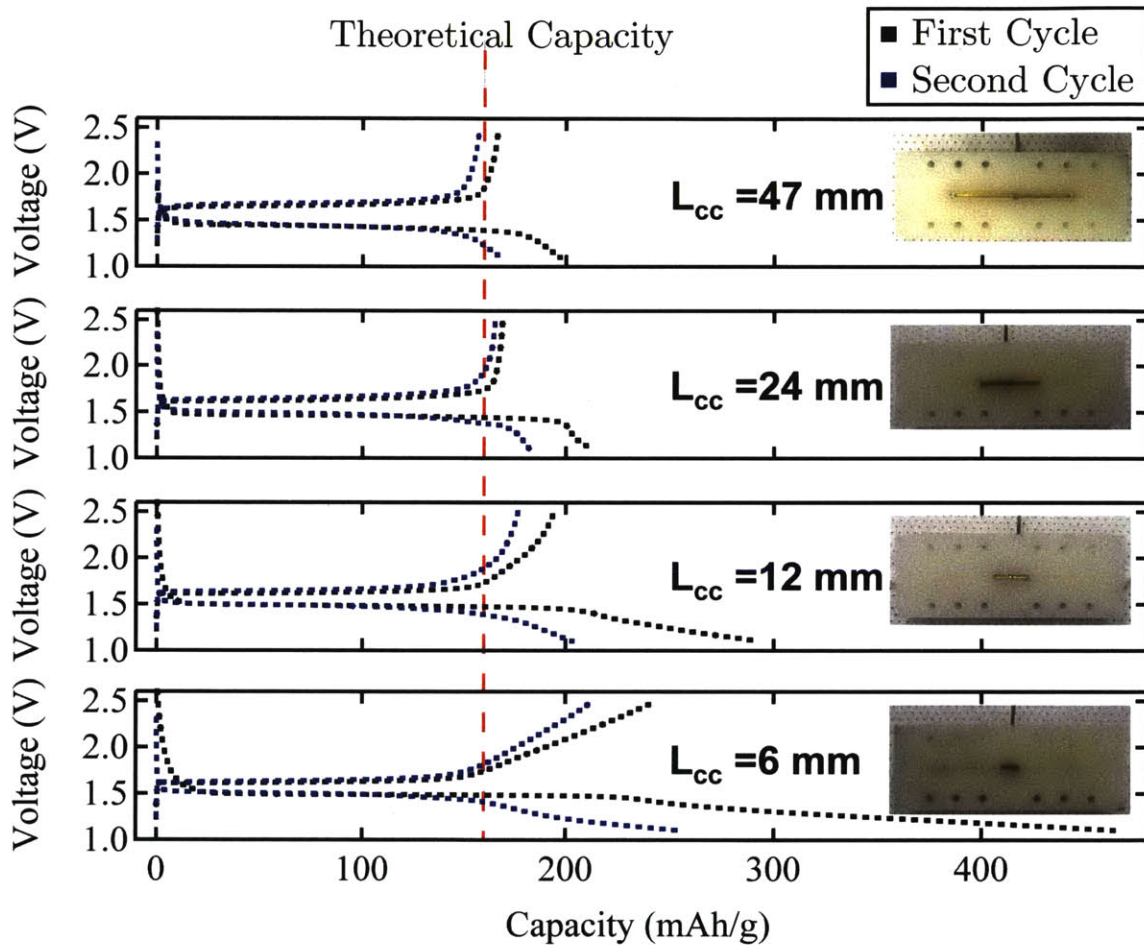
Figure 3-7: Experimental data from extended-EAZ cycling at C/11 rate for several current collector lengths. Data for longer current collectors exhibits similar extended-EAZ capacity, corresponding to a current-density controlled extended-EAZ regime. Shorter current collectors exhibit long "tail" regions corresponding to the total current controlled regime of extended-EAZ. Image courtesy of Yajie Dong.

A) Current density regime

6 mm Current Collector, C/11

12 mm Current Collector, C/11

B) Total Current Regime

6mm current collector, C/11

12mm Current Collector, C/22
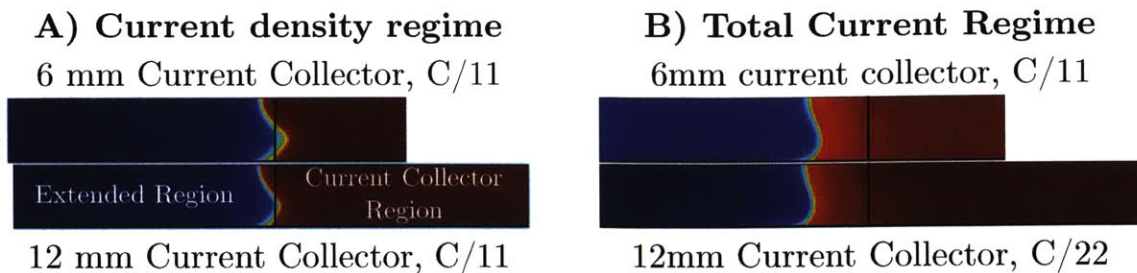
Figure 3-8: Comparison of the distribution of x_{Li} demonstrating the two regimes of extended-EAZ: a) Simulations at a C/11 rate at 2 different current collector lengths show similar extent of lithiation beyond the current collector upon lithiation to 1.4 Volts, corresponding to the current-density controlled regime. b) Simulations using the same total current but different current collector lengths show similar extent of lithiation beyond the current collector upon lithiation to 1.2 Volts, corresponding to the total current controlled regime.

the experimental results from the 24 mm and 47 mm current collector experiments. On the right is a comparison between two simulations with different current *densities*, but the same *total* current as a result of different current collector lengths. Once again, the degree of lithiation in the extended-EAZ region is very similar between these two cases, corresponding to the existence of a *total* current controlled regime of extended-EAZ behavior.

3.3.3 Evidence for Anisotropic Conductivity

A second interesting result from the comparison between model predictions and experimental data deals with the difference in the slope of the tail region of the voltage profile noted in Section 3.3.1. Figure 3-9 (a) compares the voltage profiles from simulations to the experimental results for both 6 mm and 12 mm current collector systems undergoing lithiation at a C/11 rate. In both cases the slope of the voltage profile fits well with the experimental data through the plateau region, however the slope of the tail region is steeper for both sets of model data than in their respective experimental comparisons. Section 3.3.1 shows that the plateau region of the voltage profile corresponds to the movement of the "phase boundary" between regions of lithiated and delithiated suspension inwards to the center of the cell. As this "phase

a) Isotropic Conductivity

b) Anisotropic Conductivity
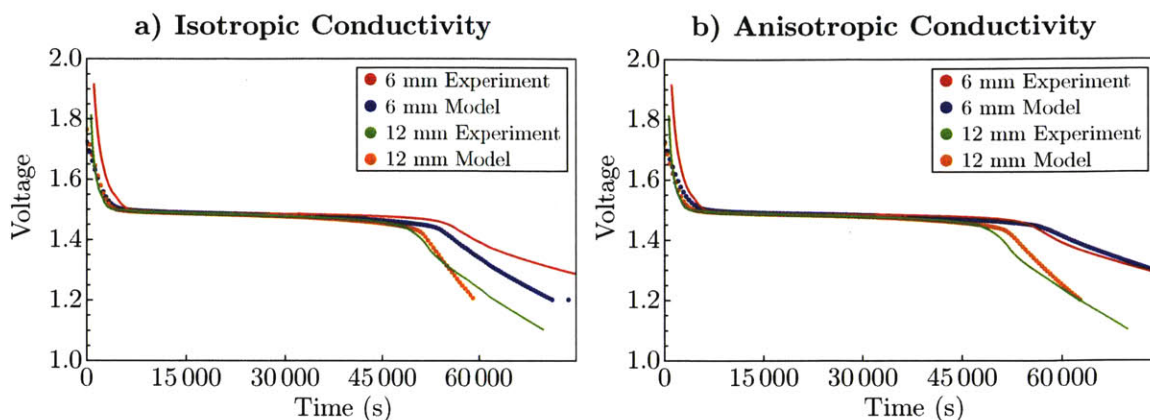
Figure 3-9: Comparison of experimental and model result voltage profiles during lithiation at a C/11 rate for both 6 and 12 mm current collectors. a) shows the model results when using an isotropic 1 mS/cm electronic conductivity. b) shows the model results when using an anisotropic electronic conductivity of 2 mS/cm parallel to the flow direction, and 1 mS/cm perpendicular.

boundary" moves inwards electrons must travel progressively farther from the current collector to the boundary region where the intercalation occurs, leading to a roughly linear increase in the electronic ohmic potential drop as a function of time through the plateau region. Thus, the slope of the voltage profile on the plateau is proportional to the electronic conductivity of the suspension perpendicular to the flow direction and the current density being applied to the system. Since the modeled and experimental voltage profiles match well in the plateau region, one can conclude that the 1 mS/cm electronic conductivity used for the simulations is a good estimate for the suspension used experimentally.

However, it is noted that the slope of the tail region is too steep in the model predictions compared to the experimental data. As discussed in Section 3.3.1 the slope of this tail region is proportional to the electronic conductivity of the suspension used *parallel* to the flow direction, and to the total current applied to the cell. The model predictions using an isotropic 1 mS/cm electronic conductivity result in a steeper tail region than experimentally observed, suggesting that the electronic conductivity of the suspension used in the experiment is higher than 1 mS/cm *parallel* to the flow direction. Combining this with the prior observation that the plateau voltage profiles match well between model and experiment suggests that the suspensions

exhibit *anisotropic* electronic conductivity. Figure 3-9 (b) shows a comparison of the model prediction and experimentally observed voltage profiles for the same C/11 lithiation of 6 mm and 12 mm current collector cells using an anisotropic electronic conductivity of 2 mS/cm parallel to the flow direction and 1 mS/cm perpendicular to the flow direction. This results in a noticeably improved agreement between prediction and experiment, particularly in the tail region of the voltage profile.

While it is clear from the results presented that inputting an anisotropic electronic conductivity into the simulations leads to better agreement with experimental results it is important to understand how that anisotropy develops to justify its presence in the model. The development of anisotropic electronic conductivity has previously been observed experimentally by Dr. Bryan Ho. He demonstrated that flowing the suspensions used as SSFC electrodes induces shear-rate driven particle segregation based on particle size [32]. This particle segregation leads to both regions in the bulk of the suspension that are locally enriched in the conductive carbon black additive, and more significantly in the formation of a thin layer of carbon black-rich material along the walls of the flow channel. This thin layer of conductive carbon black in turn leads to significantly higher electronic conductivity measured parallel to the direction of flow compared to perpendicular to the flow direction. In the most extreme case the conductivity parallel to the flow direction was 800 times greater than perpendicular to the flow direction [32]. In general, Ho's results demonstrate that the degree of anisotropy observed increases with both flow rate and total distance of flow; since the experimental tests of the extended-EAZ region only involve flow of the suspension from a syringe into the experimental test cell the relatively small anisotropy ratio of 2 used to obtain a good fit between model predictions and experimental results is reasonable.

This experimental observation of anisotropic electronic conductivity justifies its use in modeling the extended-EAZ behavior. The combination of experimental observation and the improved fit between model prediction and experimental results strongly suggests that anisotropic electronic conductivity plays a significant role in understanding the extended-EAZ. Additionally, the degree of anisotropy observed

here is relatively small compared to the more extreme cases observed in Ho's work, suggesting that the extended-EAZ size may be significantly larger for suspensions that have been flowed over a longer distance and therefore developed higher conductivity parallel to the direction of flow.

3.3.4 First Cycle Capacity Loss

The final important result from Dong's experiments that this modeling work seeks to explain is the significant coulombic inefficiency consistently observed in the first cycle of extended-EAZ experiments. Figure 3-10 shows the capacity obtained on both lithiation and delithiation as a function of current collector length for both the first and second cycles of experimental testing. From the experimental data two things are apparent: first that the coulombic efficiency of the first cycle is markedly lower than that of the second cycle, and second that the amount of capacity lost in the first cycle appears to be independent of the current collector length and total capacity of the cell. These two facts suggest the mechanism roughly depicted in Fig. 3-10 b) as a possible explanation for the observed coulombic inefficiency in the first cycle. The suggested mechanism proposes that the size of the extended-EAZ differs between lithiation and delithiation, with the lithiation extended-EAZ being larger. If that is the case it is expected that after the first delithiation some suspension in the extended-EAZ remains lithiated, leading to a low coulombic efficiency in the first cycle. Additionally, since the capacity that is not delithiated is all within the extended-EAZ, the magnitude of the capacity loss is expected to be independent of the current collector length as is observed experimentally. Then on the second lithiation only the capacity that was delithiated in the first delithiation can be relithiated, leading to a lower coulombic inefficiency for the second cycle than the first.

This mechanism seems to provide a good qualitative explanation for the observed experimental results, however on its own it makes no quantitative predictions. Additionally, it is not immediately clear whether or not the size of the extended-EAZ should differ between lithiation and delithiation, and if so why it should be smaller on delithiation. In order to address this question a single lithiation-delithiation cycle
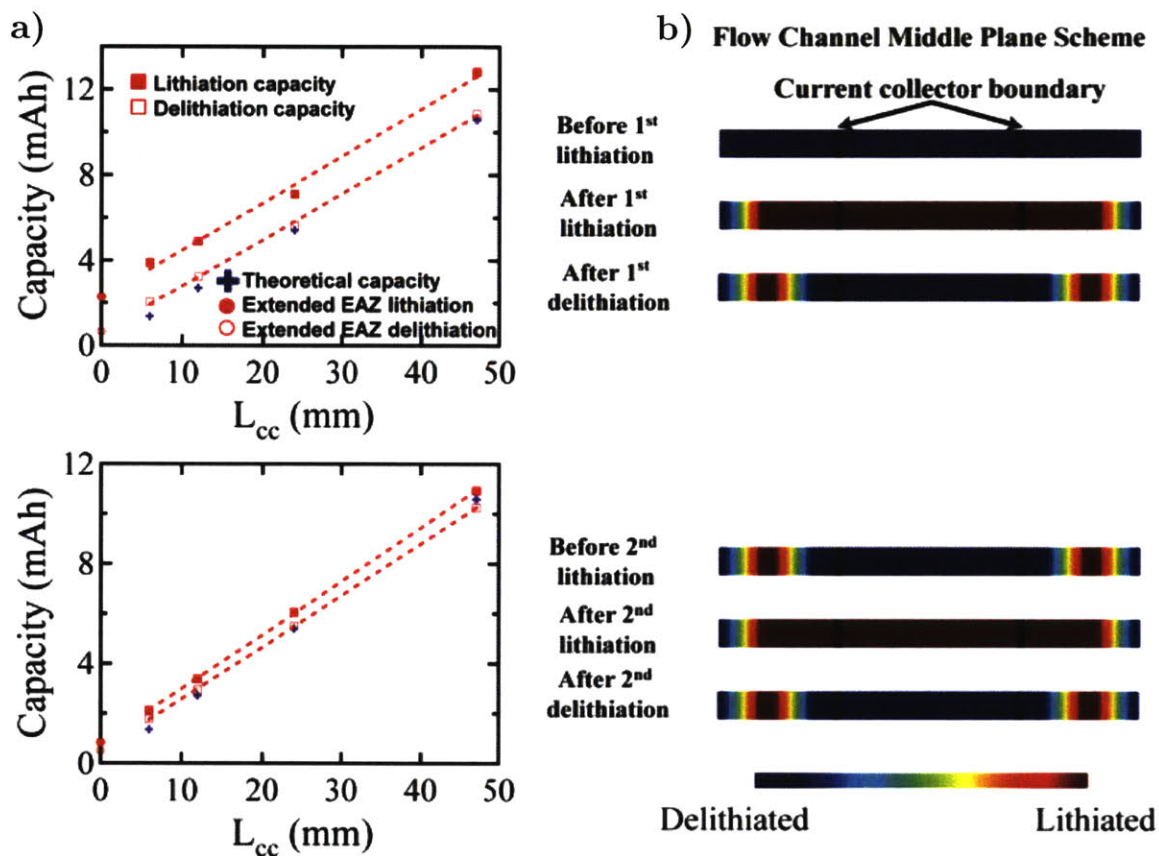
Figure 3-10: a) Comparison of the coulombic efficiency of the first and second cycles of extended-EAZ experiments at C/11 rate as a function of current collector length. b) Schematic depicting a possible explanation for the differing coulombic efficiency between first and second cycles based on a difference in the size of the extended-EAZ upon lithiation and delithiation. Figure courtesy of Dr. Yajie Dong.
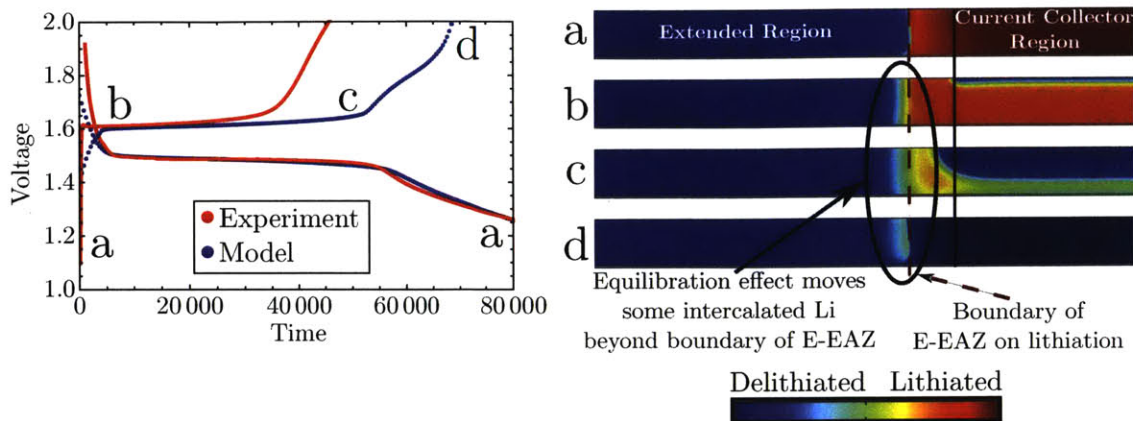
Figure 3-11: Comparison of modeled and experimental voltage profiles on both lithiation and delithiation at C/11 for a 6 mm current collector. Plots of the spatial distribution of intercalated lithium at several points during delithiation are shown. Some intercalated lithium is still present in the extended-EAZ region once the delithiation cutoff voltage is hit, leading to some coulombic inefficiency in the first cycle. However, the experimental data exhibits significantly greater first cycle coulombic inefficiency suggesting that there is an additional effect that is not being captured by the model.

at C/11 is simulated for a cell with 6 mm of current collector. Figure 3-11 compares the modeled and experimental voltage profiles on both lithiation and delithiation and shows the spatial distribution of intercalated Li at several points in time during the delithiation process.

From the results shown in Fig. 3-11 it is apparent that the model does predict a noticeable capacity difference between the first lithiation and first delithiation of 5%. However, the experimentally observed delithiation capacity is only 73.8% of the model prediction, suggesting that there is an additional effect that is not being captured by the model. The most likely explanations for the additional coulombic inefficiency present in the experimental data are the presence of a side reaction that is not included in the model, or possibly a morphological change in the suspension during lithiation that breaks the connection of some active LTO particles to the conductive carbon network. An additional piece of evidence supporting the presence of an unmodeled side reaction or morphological change during lithiation is the experimental observation that LTO suspensions often become stuck (i.e. no longer flowable) after cycling. Despite this inconsistency between model and experiment for the delithiation process,

68

understanding the origin of the first cycle coulombic inefficiency predicted by the model is still of interest since it would not be expected *a priori*.

The predicted capacity difference between lithiation and delithiation is best understood from the distributions of intercalated Li shown at four different times during the delithiation process in Fig. 3-11. At the start of delithiation there is a relatively sharp "phase boundary" between lithiated and delithiated suspension in the extended-EAZ as seen in Fig. 3-11a. As the delithiation process proceeds the suspension closest to the current collector delithiates first and a second "phase boundary" develops in Fig. 3-11b. This second "phase boundary" then moves from the current collector to the separator, and outwards into the extended-EAZ in Fig. 3-11c. This closely resembles the lithiation process seen in Section 3.3.1 where the suspension nearest the current collector is lithiated first as a result of the suspension electronic conductivity being lower than the ionic conductivity. While this process is occurring notice that the original "phase boundary" between lithiated and delithiated suspension in the extended-EAZ is becoming progressively more diffuse. This is a result of an equilibration process between nearby active particles with differing states of charge, and is ultimately the cause of the first cycle capacity loss predicted by the model. This point is seen most clearly in Fig. 3-11d which shows the distribution of intercalated Li at the end of the delithiation process. All of the suspension in the current collector region and the suspension in the extended-EAZ up to the same position as the "phase boundary" at the end of lithiation (as marked by the dashed red line) has been delithiated. However, some still lithiated suspension remains farther from the current collector in the extended-EAZ, and it is this capacity that leads to the first cycle coulombic inefficiency. Finally, compare the distribution of intercalated Li in Fig. 3-11d to the schematic explanation in Fig. 3-10 after the first delithiation. From this comparison it seems that the initial hypothesis is a reasonable explanation for some of the difference between the coulombic inefficiency seen in the first and second experimental cycles.

69

3.4 Discussion

3.4.1 Implications for Intermittent Flow Operation

There are three main conclusions to be drawn based on these modeling results and the comparison with experimental work, each of which has important implications for operating an SSFC in intermittent flow mode. First, two different regimes of extended-EAZ behavior exist. The first regime is present in all SSFC systems and results in a smaller extended-EAZ. It results from the gradual drop off in the solid phase potential at the boundary of the current collector and extended-EAZ, leading to some lithiation or delithiation occurring in the suspension immediately adjacent to the active current collector volume. Since this process occurs while the suspension within the current collector region still has available capacity, and therefore the majority of the current goes into the main active cell volume, the size of the extended-EAZ in this regime is a function of the average current *density* applied to the cell as well as the suspension conductivity. This is the regime seen in Fig. 3-8a.

The second regime is only relevant for cells operating with small *total* applied current, either as a result of running at low rate or using a short current collector. In contrast to the first extended-EAZ regime where some of the electrochemical reaction is occurring outside the current collector volume throughout the entire charge or discharge process, this second regime only becomes important at the end of a charge or discharge. Once the capacity within the current collector region of the cell is fully utilized it is possible for all of the current applied to the cell to travel into the extended-EAZ to continue the electrochemical reaction, this process results in the second regime of extended-EAZ behavior. However, since all of the applied current is traveling into the extended-EAZ in this regime the ohmic potential drop in the solid phase can be very large, therefore this regime is only apparent when the potential drop resulting from the total current of the cell traveling from the current collector to the edge of the first regime of extended-EAZ is small enough that it does not reach the cutoff voltage for the cell. When this is the case the electrochemical reaction continues until the boundary between lithiated and delithiated suspension is

sufficiently far out into the extended-EAZ that the cutoff voltage is reached, as seen in Fig. 3-8b. This leads to a potentially large extended-EAZ, whose size is primarily dependent on the total current applied and the electronic conductivity of the suspension used. Because the extended-EAZ in this regime is relatively larger compared to the total capacity available in the current collector region larger losses are observed. In particular, the first cycle capacity loss that is consistently seen experimentally represents a significantly larger percentage of the total system capacity for smaller cells that operate in this total-current extended-EAZ regime than for the larger cells operating in the second regime. As a result in a practical SSFC system it is preferable to operate in the first regime of extended-EAZ behavior.

The second major conclusion of this chapter relates to the development of anisotropic conductivity in SSFC suspensions. Prior work to characterize SSFC suspensions has shown that flow induces size-dependent particle segregation that elevates their electronic conductivity parallel to the flow direction and reduces it perpendicular to that direction [32]. The comparison of model prediction and experimental data in this work provides further confirmation of this effect, and additionally demonstrates that it is particularly important for determining the size of the extended-EAZ resulting from the second (total current controlled) regime of behavior. Since higher electronic conductivity parallel to the flow direction increases the size of the extended-EAZ, which is seen to reduce system efficiency, it is important to minimize this effect. Therefore, when operating an SSFC in intermittent flow mode it is important to take measures to prevent the particle segregation effect, for example by roughening the surface of the flow channel, *in situ* sonication of the suspension, and minimizing both the total flow distance and flow rate in the system [32].

The third conclusion relates to the consistent observation of significant first cycle coulombic inefficiency in extended-EAZ experiments. Based on comparing modeling predictions with the experimental results, it is believed that a significant portion of this effect is not the result of true capacity loss, instead it occurs because of an equilibration effect in the extended-EAZ. This equilibration leads to the migration of Li farther into the cell inlet or outlet beyond the extent of the extended-EAZ region.

71

Therefore much of the observed "capacity loss" upon the first delithiation should be recoverable by simpling flowing the suspension into the active cell and continuing the delithiation process. This result implies that when operating in intermittent flow mode higher capacity will be observed for the first plug that is charged or discharged than for subsequent plugs (which have already had some of their capacity utilized when they were in the extended-EAZ as the prior plug was charged or discharged).

3.4.2 Model Shortcomings

While a great deal of insight can be gleaned from the results of this modeling work, and particularly the comparison with experimental observations, the model does have some shortcomings. In particular, two effects are consistently not captured completely by the model. First, at the end of the plateau region during lithiation the model predicts a smooth transition in the voltage profile between the slope of the plateau region and the slope of the tail region. However, the experimental data consistently exhibits a steeper drop off in the applied voltage for a short period of time at the end of the plateau prior to the profile leveling off to the slope of the linear tail region. Figure 3-12 shows an example system where this is particularly apparent. The cause of this inconsistency is not immediately apparent, but is likely to be relatively unimportant based on the small difference between the model prediction and experimental results.

The second consistent difference between model predictions and experimental observations relates to delithiation, and is a more significant effect than the small difference seen on lithiation. Two major differences are observed between the predicted and observed voltage profiles on delithiation: first, the observed voltage reaches the plateau value nearly immediately upon the start of the delithiation process while the model predicts a more gradual voltage increase; second, the model predicts significantly more capacity upon delithiation than is observed. Both of these effects are seen in Fig. 3-11. One possible explanation is that these effects result from some side reaction that is not incorporated in the model. A better understanding of these inconsistencies between model and experiment on delithiation would be valuable.
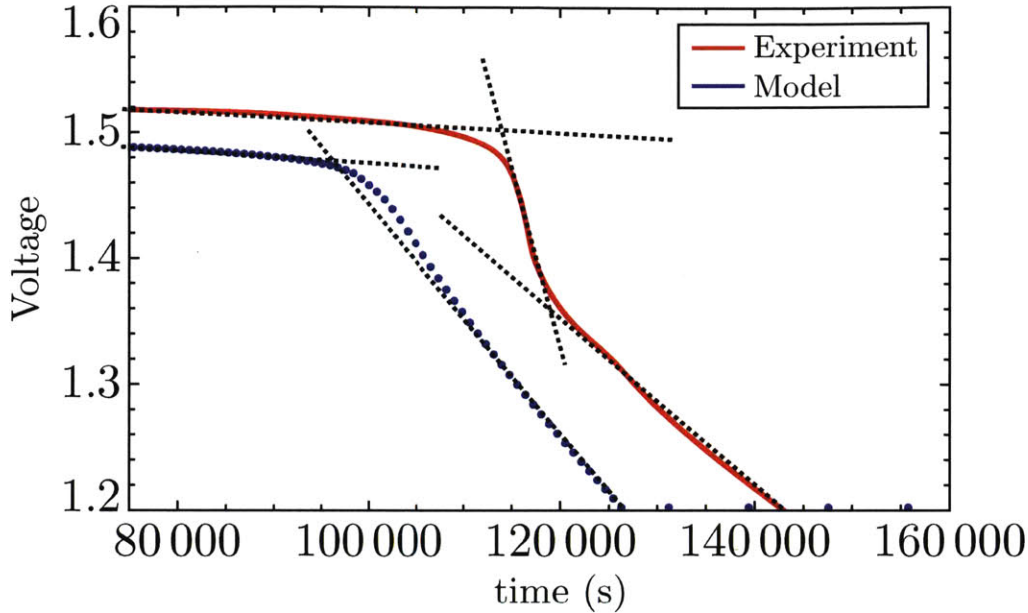
Figure 3-12: Comparison of modeled and experimental voltage profiles near the end of the plateau region for a 12 mm current collector cell at C/22 rate. Dashed lines are visual guides indicating the "knee" present in the experimental data that is not captured by the model.

3.4.3 Model Sensistivity to Input Parameters

While many of the parameters used in the model have been tested experimentally and have a great deal of literature data available, in particular the electrolyte transport properties, less data is available regarding the electronic properties of the novel SSFC suspensions [39]. As a result, it is of interest to examine the sensitivity of the model to those parameters. In particular some measurements are available of suspension electronic conductivity and interfacial resistance from the characterization work of Ho, however that was performed on slightly different formulations than were used for the extended-EAZ experiments and therefore can only provide order of magnitude estimates. In order to reach good agreement between model predictions and experimental results, simulations with several different values for the electronic conductivity and interfacial resistance were performed. The results are presented below to provide an understanding of the model's sensitivity to those parameters.
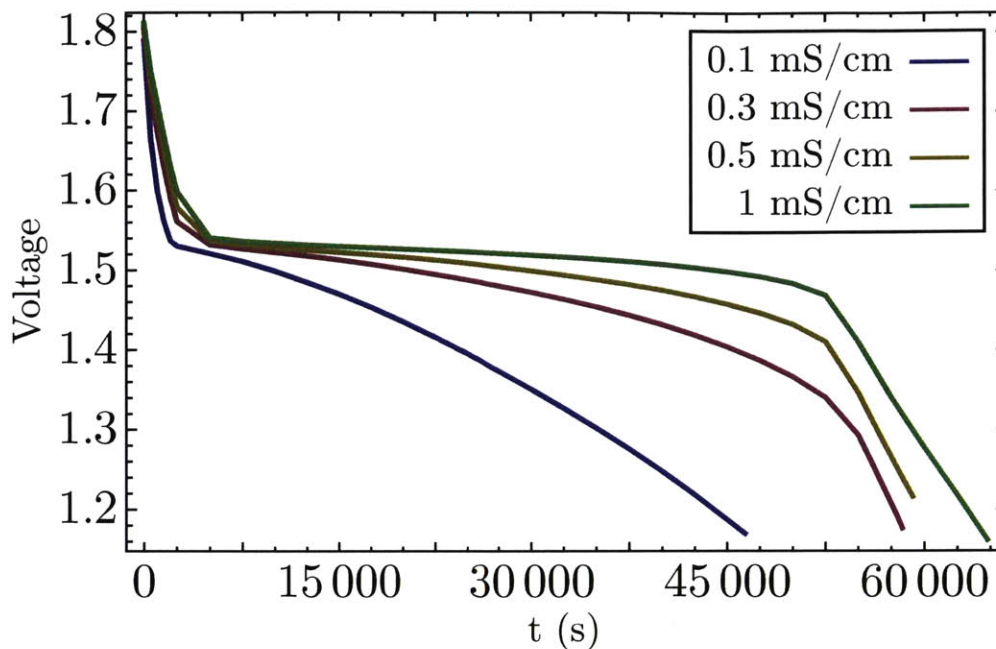
Figure 3-13: Modeled voltage profiles for lithiation in a 12 mm current collector at C/11 rate using several different electronic conductivity values.

Electronic Conductivity

Figure 3-13 compares simulated voltage profiles for lithiation at C/11 rate in a cell with a 12 mm length current collector using several different values for σ. Based on these results it is apparent that the value σ has a large effect on the resulting voltage profile produced from the model. In particular, the value of σ primarily affects the slope of the voltage plateau and the tail region. For very small values of σ (e.g. the 0.1 mS/cm curve) the polarization resulting from the ohmic drop in the conductive carbon network is so large that the cutoff voltage is hit before the end of the plateau region.

This behavior is reasonably explained by considering what occurs during the lithiation process. As seen in Fig. 3-6 during the plateau portion of the voltage profile a "phase boundary" has developed separating regions of lithiated material near the current collector and unlithiated material in the center of the channel, and over time this "phase boundary" moves inwards towards the center of the flow channel. During this process the intercalation reaction is always occurring at the location of the
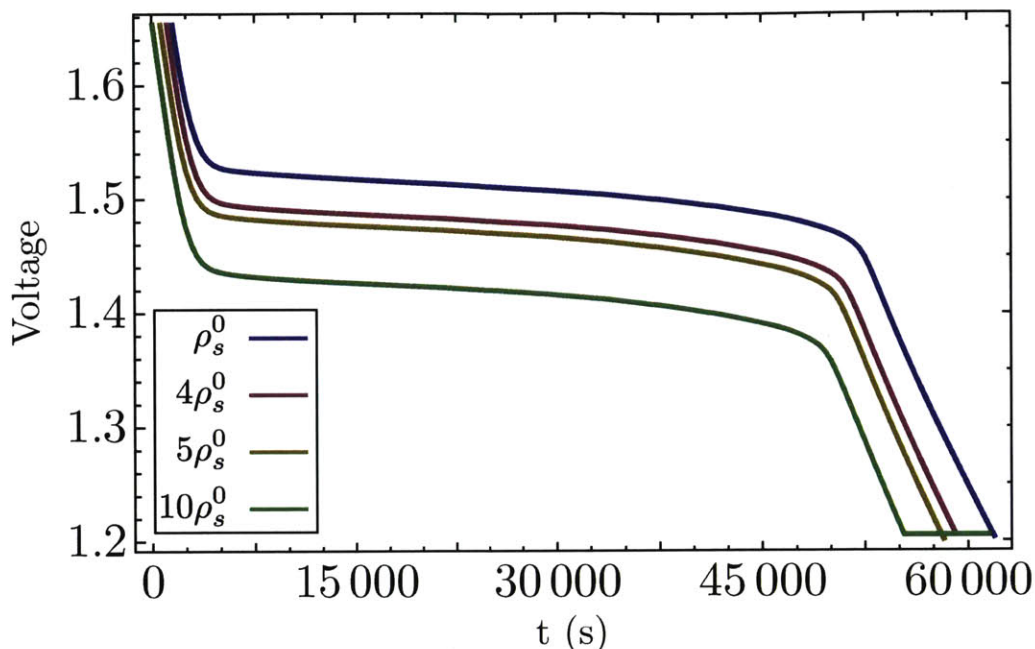
Figure 3-14: Modeled voltage profiles for lithiation in a 12 mm current collector cell at C/11 rate using several different interfacial resistance values. The lowest tested interfacial resistance was $\rho_s^0 = 0.00177\ \Omega \cdot m^2$.

"phase boundary", so as a result the overpotential needed to drive the reaction is expected to remain roughly constant over the whole plateau. However, as the "phase boundary" moves inwards the electron travel distance from the current collector to the location of the intercalation reaction is constantly increasing, and therefore the ohmic potential drop in the conductive network is also increasing. As a result, it is expected that the slope of the plateau in the voltage profile should be proportional to σ, as is seen in the results in Fig. 3-13.

Current Collector Interface Resistance

Figure 3-14 compares simulated voltage profiles for lithiation at C/11 rate in a cell with a 12 mm current collector using several different values for the interfacial resistance. The interfacial resistance adds a roughly constant polarization throughout the entire voltage profile resulting in a shift up or down in voltage and little change in the shape of the profile as ρ_s varies. In addition to the main voltage shift effect, there is a slight change in the position of the end of the plateau region apparent in

Fig. 3-14. As the interfacial resistance increases the additional polarization leads to less usable capacity on the plateau of the voltage profile.

Chapter 4

Model-Driven Optimization of SSFC Flow Channel Design

4.1 Motivation

One of the primary advantages of developing a continuum model for SSFC performance that can be solved using finite element methods (FEM) is the flexibility that FEM provides for applying the model to a variety of geometries. In the past porous electrode based models have been used for optimization of Li-ion battery electrodes, in particular for optimizing electrode thickness and porosity to improve energy density or rate capability [35, 37, 46]. The fuel cell community has also had great success using FEM to solve continuum models and perform more complex two- and three-dimensional geometry optimization of flow channels than is needed for conventional Li-ion battery geometries [47–50]. Recently some work has been done in the flow battery community to develop predictive continuum models in both two and three dimensions, however as of yet little focus has been placed on leveraging the modeling capability to optimize the flow channel geometry [42, 43, 51].

The goal of the work presented in this chapter is to demonstrate the viability of using the model for SSFC operation developed in this thesis as a design tool for improving system performance by optimizing flow channel geometry. In general, decreasing flow channel size will improve rate capability for a given SSFC suspension,

however it will both make pumping more difficult and increase the amount of inactive material needed in the system potentially decreasing overall system energy and power density. Therefore an optimized channel geometry will balance these effects.

In this chapter a procedure for optimizing flow channel geometry is developed with the goal of maximizing a figure of merit created to characterize the performance of a given channel geometry. Several possible candidate geometries are explored, each containing variable geometric design parameters (e.g. channel width and channel depth) that must be optimized. Since the optimized flow channel geometry will vary for different active SSFC suspensions depending on their material properties a single representative suspension is selected for all of the optimization work in this chapter. Model data for a simple planar geometry at several rates is compared to experimental results as validation prior to performing the optimization procedure. Results of the optimization procedure are presented for each candidate geometry, and subsequently a single geometry is selected to be used in the construction of a medium-scale (1 kW/1 kWh) SSFC system to meet ARPA-E project milestones.

4.2 Optimization Procedure

4.2.1 Model Parameters and Validation

The suspension selected for performing the channel geometry optimization contains 20 vol% $LiNi_{1/3}Mn_{1/3}Co_{1/3}O_2$ (NMC) as the active storage material and 3.5 vol% C45 carbon black as the conductive additive co-suspended in a commercial Diakin electrolyte. This suspension was selected based on it's reliability and good performance in prior experimental testing. The first step in determining the optimum channel geometry is to determine the properties of the suspension of interest and run test simulations in a simplified channel geometry to compare with experimental results in order to validate the model.

Table 4.1 contains a list of the values used for the model parameters in the geometry simulations. The electrolyte transport properties are once again based on the

Parameter	Symbol	Value
Suspension electronic conductivity	σ	4 mS/cm
Electrolyte volume fraction	ϵ	0.8
Electrolyte volume fraction in separator	ϵ_{sep}	0.5
Initial salt concentration	c_e^0	1300 mol/m^3
Specific surface area	a_s	$1.2 \cdot 10^5$ 1/m
Initial intercalated Li concentration	c_s^0	$0.999c_s^{\text{theoretical}}$
Exchange current density coefficient	k_p	6 mA/cm^2
Current collector resistance	ρ_s	3.04 m$\Omega \cdot$ m^2

Table 4.1: Model parameters used for geometry optimization simulations

published experimental results of Valoen and Reimers [39]. The volume fraction of active particles, ϵ_s, is known from the suspension composition, as is the initial salt concentration in the electrolyte. The three important model parameters that remain are the suspension electronic conductivity, σ, the interfacial resistance between the suspension and current collector, ρ_{surf}, and the equilibrium voltage function of the NMC active material, $V_{eq}(x_{Li})$. Electronic conductivity measurements performed by Dr. Nir Baram on the suspension result in $\sigma = 4$mS/cm, therefore that value is used in the modeling work. Some prior work on modeling NMC electrodes using porous electrode theory is available, however attempts to use the V_{eq} functions published therein resulted in poor agreement with the experimental tests of the NMC suspension of interest [52, 53]. In order to obtain good agreement with the experimental results for the NMC suspension the equilibrium voltage function is determined from fitting to a very slow cycle at C/40 rate performed by Dr. Nir Baram. The resulting equilibrium voltage function is given by:

$$V_{eq}^{NMC}(x_{Li}) = 4.74113 + 0.593962(x_{Li} - 1.47008)^2 + 0.559608(x_{Li} - 3.16779)$$
$$- \exp\left[61.022(x_{Li} - 0.996101)\right]$$

where x_{Li} is the fraction of intercalated Li based on a maximum capacity of 159.654 mAh/g of NMC. Figure 4-1 compares the fitted equilibrium voltage function to the C/40 experimental data.

In order to validate the model, and determine the value of the suspension-current
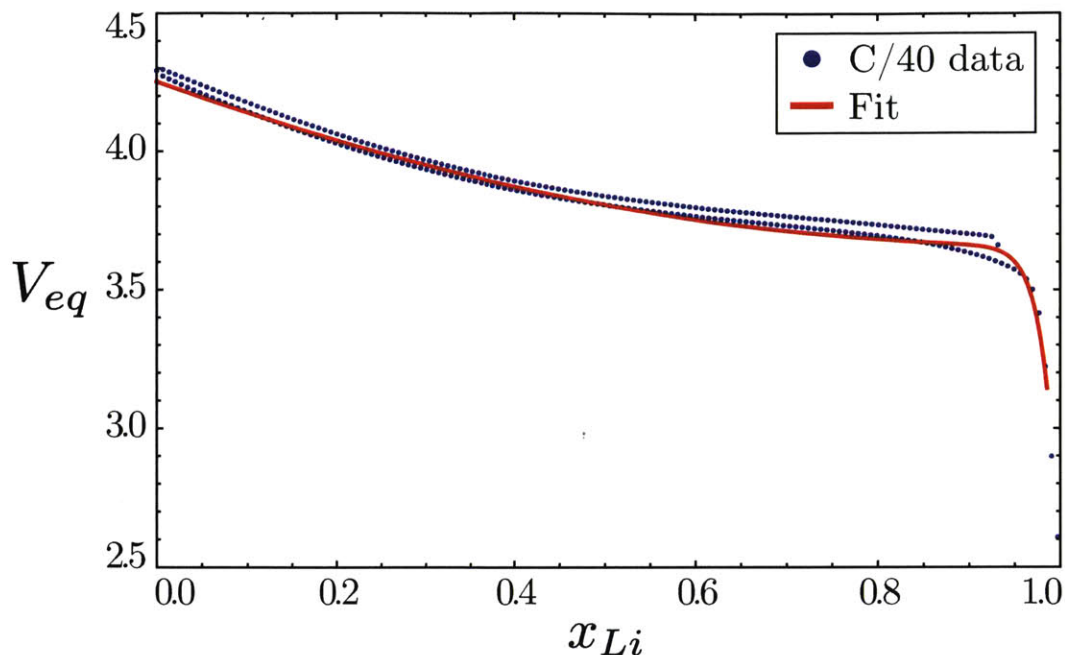
Figure 4-1: Voltage profile obtained from Dr. Nir Baram for a low rate C/40 cycle of the 20% NMC suspension compared with the fitted equilibrium voltage profile.

collector interfacial resistance, simulations using the above parameters were performed for cycles run at C/10, C/5, and C/3 for comparison with experimental results using the 20% NMC suspension in a Swagelok cell with a 0.508 mm thick cathode against a Li-foil anode. Based on these results a surface resistivity of 0.0030397 Ω/m^2 is observed to give good agreement between model predictions and experimental data. Figure 4-2 compares the predicted and observed voltage profiles for both charge and discharge at each of the three tested rates. Based on the good agreement between model prediction and experimental observation, the model is believed to be usable for optimization of the flow channel geometry.

4.2.2 Figure of Merit

In order to obtain an optimum channel geometry it is necessary to determine how the "performance" of a given channel is measured. In general, a number of reasonable figures of merit may be used to quantify "performance". In this section the reasoning behind selection of the particular figure of merit used in this work is elucidated.
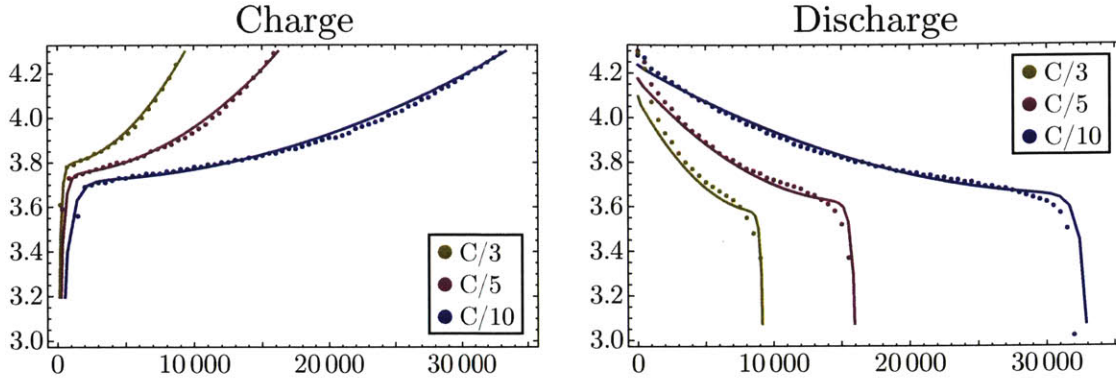
Figure 4-2: Comparison of model predictions and experimental data for cycling at C/10, C/5, and C/3 of the 20% NMC suspension against a Li foil anode in a Swagelok cell with a 0.508 mm thick electrode. Filled circles are experimental data, solid lines are model predictions. Experimental data courtesy of Dr. Nir Baram

In general flow battery systems contain three primary components: the electrolytes (or semi-solid suspensions for SSFCs) that are the active storage material, the storage tanks, tubing, and pumping system, and finally the power stack where the electrochemical reaction takes place. Ultimately the system level energy density is limited by the energy density of the active storage material, the remaining inactive components are necessary to move energy in and out of the electrolytes but also serve to reduce system energy and power density. In addition, the inactive components of a flow battery system (storage tanks, pumping apparatus, power stack components, etc.) are a significant fraction of the overall cost of the system (20-50% depending on power to energy ratio) [54, 55]. As a result, one of the main goals in designing a flow battery power stack is to minimize the amount of inactive material in the system.

When designing a flow battery system generally two requirements must be met, a system level energy requirement (e.g. 1 kWh), and a system level power requirement (e.g. 1 kW). The energy requirement primarily affects the size of the storage tank needed, and is relatively unimportant for the power stack design. In contrast, the system level power requirement determines how large of a power stack is needed, and therefore the main focus of optimizing flow channel design should be to maximize the amount of power that can be obtained from the minimum possible amount of inactive components. Therefore, the figure of merit used to quantify performance in

this work is designed to favor flow channel configurations that can provide high power with small amounts of inactive material (e.g. current collector, separator, etc.). The figure of merit, F, used to accomplish this is:

$$F = \frac{P_{\text{specific}}}{\epsilon_{\text{inactive}}} \cdot \eta_{energy} \cdot \eta_{\text{capacity}} \tag{4.1}$$

where P_{specific} is the specific power on discharge in W/g, $\epsilon_{\text{inactive}}$ is the fraction of inactive mass for the flow channel configuration, η_{energy} is the round-trip energy efficiency of cycling in the flow channel configuration, and η_{capacity} is the percentage of the theoretical capacity obtained on discharge.

This figure of merit quantifies performance by favoring flow channel designs which maximize power per mass of inactive components and achieve high energy efficiency, as well as good utilization of the available capacity of the active storage material. Therefore, F should be a good metric for selecting flow channel designs that minimize the size of the power stack needed to meet system level requirements, while still enabling good system level energy density based on high utilization of the active storage material's theoretical capacity. As a point of reference the SAFT VL45E Fe Li-ion battery has a specific power of 183 W/kg, assuming 30% mass fraction of inactive components and 90% theoretical capacity (conservative estimates designed to maximize F) gives a figure of merit of $F = 0.55$ W/g [19, 56]

4.2.3   Candidate Geometries and Meshing

The first step in optimizing flow channel geometry is the selection of a (or several) potential candidate geometries and determining the characteristic geometric parameters that can be varied to affect performance. During initial planning for this work some more complex three-dimensional flow channel geometries were considered with the goal of inducing convection-driven mixing in the active electrode suspensions in order to complement diffusive transport of Li^+ and potentially improve performance. Two main factors led to the abandonment of this idea: first, the high viscosity of the electrode suspensions used in SSFCs forces the use of low flow-rate modes of operation
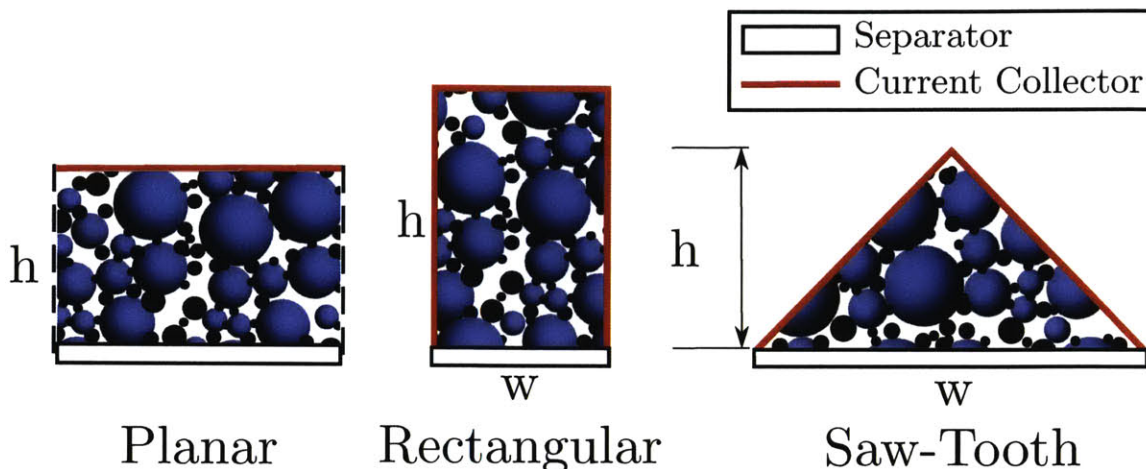
Figure 4-3: Candidate flow channel geometries to be used as the repeat unit in a full stack design.

which greatly limits the potential of convection-driven mixing, and second, experience using the full three-dimensional model to study stoichiometric flow operation and the extended-EAZ suggests that the time needed to run those simulations is too long to effectively perform a geometric optimization in three dimensions.

As a result, the goal for optimizing the flow cell geometry was simplified to optimizing the cross-section of the flow channel with the intention of using the performance-optimized cross-section as the repeat unit for constructing a full size SSFC power stack. Working with the plan of optimizing the flow channel cross-section three candidate geometries were tested: a planar flow channel that extends over the entire area of the power stack as is typical in conventional redox flow batteries, a rectangular cross section flow channel, and a saw-tooth cross-section flow channel. The only geometric parameter present for the planar flow channel is the height, h of the electrode, the rectangular channel is characterized by the channel height, h, and width, w, and finally the saw-tooth channel is also characterized by the height, h, and width, w. Each candidate flow-channel cross-section, as well as their relevant geometric parameters, is shown in Fig. 4-3.

Each of these candidate geometries has some potential advantages and disadvantages. The planar channel geometry is the most straight-forward to manufacture and requires the least amount of current collector material for a given h. However, for

many of the SSFC suspensions that have been tested the electronic conductivity and suspension-current collector interfacial resistance have been seen to be performance limiting and therefore the additional current-collector interface and potentially reduced electron transport distances of the rectangular and saw-tooth cross-sections may be advantageous. Another potential problem with the planar channel geometry is the lack of support for the separator membrane potentially leading to the separator buckling due to pressure imbalances between the suspensions on the anode and cathode sides during flow. Both the rectangular and saw-tooth cross-section channels provide regular support for the separator membrane and the greater current collector area is likely to allow for deeper flow channels compared to the planar cross-section which may lead to an overall reduction in the amount of inactive material needed. The goal of the saw-tooth cross-section is to obtain the advantages of larger current-collector area and membrane support from the rectangular cross-section while packing more efficiently as a repeat unit to reduce the amount of current collector material used.

Mass of Inactive Components

In order to calculate the figure of merit, F, from Eqn. 4.1 to be able to optimize each channel as a function of its geometric parameters the mass of inactive components for each candidate geometry must be calculated as a function of the channel size. To accomplish this it is important to consider how each candidate geometry would be used as the repeat unit in a full cell stack in order to accurately assign the correct amount of inactive mass to an individual repeat unit. Figure 4-4 depicts an example power cell stack constructed using each candidate channel geometry. In addition, assumptions must be made about both the material and thickness of the current collector and separator.

Tonen E20MMS will be assumed as the separator material. Tonen E20MMS has a thickness of 20 μm, and a mass per unit separator area of 13 g/m^2. The current collector is assumed to be constructed of Al with a thickness of 0.1 mm, the density of Al is 2.70 g/cm^3. Based on the power stack designs in Fig. 4-4 and the assumptions
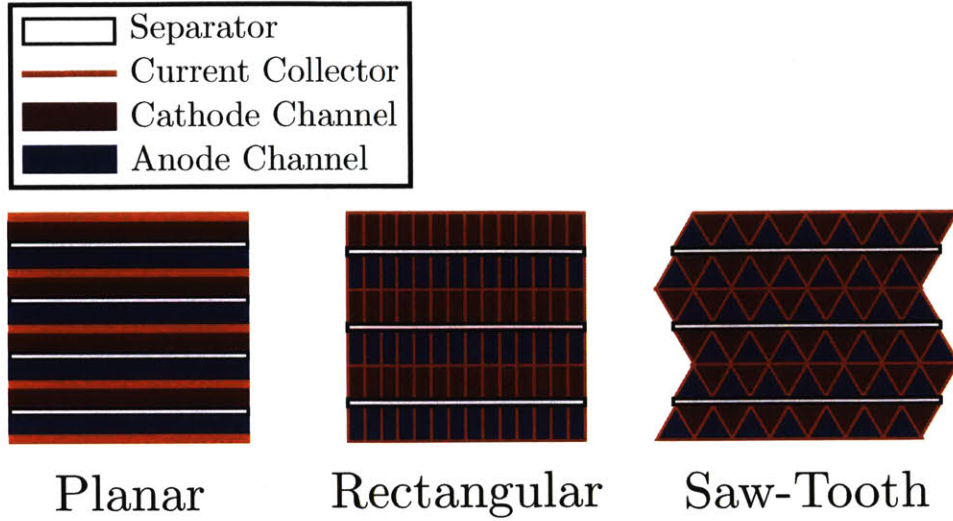
Figure 4-4: Example configurations of bipolar power stacks constructed using each of the three candidate channel geometries as the repeat unit.

about current collector and separator materials it is now possible to compute the denominator of the figure of merit, F, for each candidate channel geometry. For the planar channel geometry the resulting mass of inactive material (per unit separator area) is:

$$m_{\text{inactive}}^{\text{planar}} = \rho_{\text{Al}} \cdot t_{CC} + \rho_{sep} \tag{4.2}$$

where ρ_{Al} is the density of Al, t_{CC} the thickness of the current collector, and ρ_{sep} the mass per unit area of the separator material. Similarly, the result for the rectangular cross-section candidate geometry is:

$$m_{\text{inactive}}^{\text{rect}} = \rho_{\text{Al}} \cdot (2h + w) \cdot t_{CC} + \rho_{sep} \tag{4.3}$$

And finally, the result for the saw-tooth cross-section is:

$$m_{\text{inactive}}^{\text{saw-tooth}} = \rho_{\text{Al}} \cdot t_{CC} \cdot \sqrt{4h^2 + w^2} + \rho_{sep} \tag{4.4}$$

4.2.4 Parametric Geometry Sweep Procedure

In order to determine the optimum channel geometry the goal is to maximize $F(h)$ for the planar candidate geometry, and $F(h, w)$ for the rectangular and saw-tooth

85

candidates. Therefore simulations must be run for several values of h for the planar geometry and several pairs of (h, w) for the rectangular and saw-tooth geometries. This is accomplished using COMSOL's parametric geometry sweep feature to simulate a single charge-discharge cycle for a specified list of geometric parameters. Each cycle starts with the NMC cathode at 0.1% state of charge ($x_{Li} = 0.999$) uniformly throughout the cathode region. The cell is then galvanostatically charged at a C/3 rate until the cutoff voltage of 4.3 V is reached. At the end of charging the simulation state is stored and used as the initial conditions for a galvanostatic discharge simulation at D/3 down to a cutoff voltage of 2.5 V.

Simulations of the planar candidate geometry were performed using values of h ranging from 0.5 mm to 1.5 mm in increments of 0.1 mm and from 0.5 mm to 1.75 mm in increments of 0.25 mm. For the rectangular candidate geometry a range of w from 0.5 mm to 4.0 mm in increments of 0.5 mm was used, and a range of 0.5 mm to 1.5 mm in increments of 0.25 mm was used for h. Finer increments of 0.1 mm were used from $h = 1.0$ mm to 1.5 mm to better resolve the point where anode salt depletion occurs. The saw-tooth candidate geometry was simulated over a range of 0.5 mm to 4.0 mm for w and a range of 0.5 mm to 2.5 mm for h with 0.5 mm increments for both w and h. Additionally, finer increments of 0.1 mm were used for h from 1.5 mm to 2.0 mm between $w = 2$ mm and $w = 3$ mm with increments in w of 0.25 mm. This was done to better resolve the point where salt depletion at the anode begins to dominate. The C/3 rate was selected to perform the optimization simulations to correspond to milestone requirements for the ARPA-E project that this work is a part of. For a more complete optimization it is possible to run the parametric sweep over the rate applied to the cell in addition to varying geometric parameters. Since smaller channels are likely to be capable of running higher rates with similar polarization to larger channel sizes finding the optimum rate for each channel geometry could provide a more useful optimum geometry for real world performance. The main downside of attempting to find the optimum rate for each set of geometric parameters is computational time.

4.3 Results

4.3.1 Planar Geometry

The planar flow channel geometry is similar to the geometry of conventional Li-ion battery electrodes, and as a result rate performance is expected to fall off as h^2. This is a result of two factors: as h increases and the electrode becomes thicker the current density (per unit separator area) applied to the system must increase proportionately to maintain the same C-rate. If the resistance of the cell were the same this would lead to a linear increase in polarization and therefore decrease in rate performance, however because the electrode is thicker both the ion and electron transport distances (and therefore the cell resistance) also increase proportionally to h. This combined increase in both current density and cell resistance as electrode thickness is increased cause the polarization to increase, and rate performance to fall off, as h^2.

Figure 4-5 shows the voltage profiles on charge and discharge resulting from simulations of C/3 cycling of planar channel geometries of varying h. The increase in polarization and corresponding loss of capacity as h increases is readily apparent. The thickest geometry tested ($h = 1.75$ mm) can only access $\approx 10\%$ of the theoretical capacity of the suspension at C/3. Considering these results and based solely on electrochemical performance the lowest possible value for h is desirable.

However, while Figure 4-5 shows the expected decreases in electrochemical performance as h increases, no conclusions about the optimum channel geometry can be drawn without considering the cost associated with smaller channels. Using smaller channels has two main drawbacks: higher pressures are needed to pump the suspension electrodes, and more inactive material is needed (per unit separator area). While higher pumping pressures are undesirable, they are relatively unimportant for optimizing channel geometry because pumping energy losses are so low ($< 1\%$) when operating in stoichiometric or intermittent flow modes. However, the higher fraction of inactive material used is extremely important for designing a cost-effective flow battery system with good energy density.

The figure of merit, $F(h, w)$, discussed in Section 4.2.2 is used to account for the
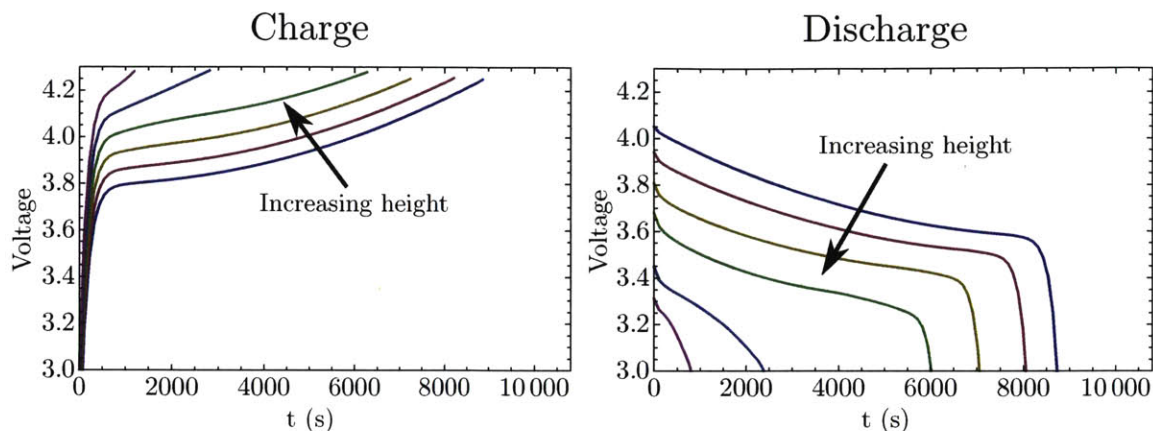
Figure 4-5: Modeled voltage profiles upon charge and discharge for planar candidate channels with $w = [0.5, 0.75, 1.0, 1.25, 1.5, 1.75]$ mm. Higher polarization and lower discharge capacity are observed as channel height increases. All simulations are for C/3 rate.

amount of inactive material used in each candidate channel geometry in addition to its electrochemical performance. $F(h)$ is calculated based on the results of the C/3 cycle simulations for each set of geometric parameters, and the results are shown in Fig. 4-6. Starting from $h = 0.5$ mm it is advantageous to increase the channel thickness because the higher capacity per unit separator area, and therefore higher current density at C/3, increase the power density of the cell design significantly. However, increasing h is only effective at improving performance (as measured by $F(h)$ up to ≈ 1.1 mm. Beyond this point the increasing polarization and decreasing usable capacity seen in Fig. 4-5 become the dominant factor by decreasing the efficiency of the cell, η, leading to a drop in the figure of merit. Based on this model data $h = 1.1$mm appears to be the optimal flow channel thickness for the modeled NMC suspension in a planar flow geometry.

4.3.2 Rectangular Geometry

The rectangular cross-section channel geometry has two main design goals. First, the current collector fins provide additional stability to the flexible membrane material to help prevent buckling. Second, the additional current collector should improve electrochemical performance in two ways. The additional current collector-suspension
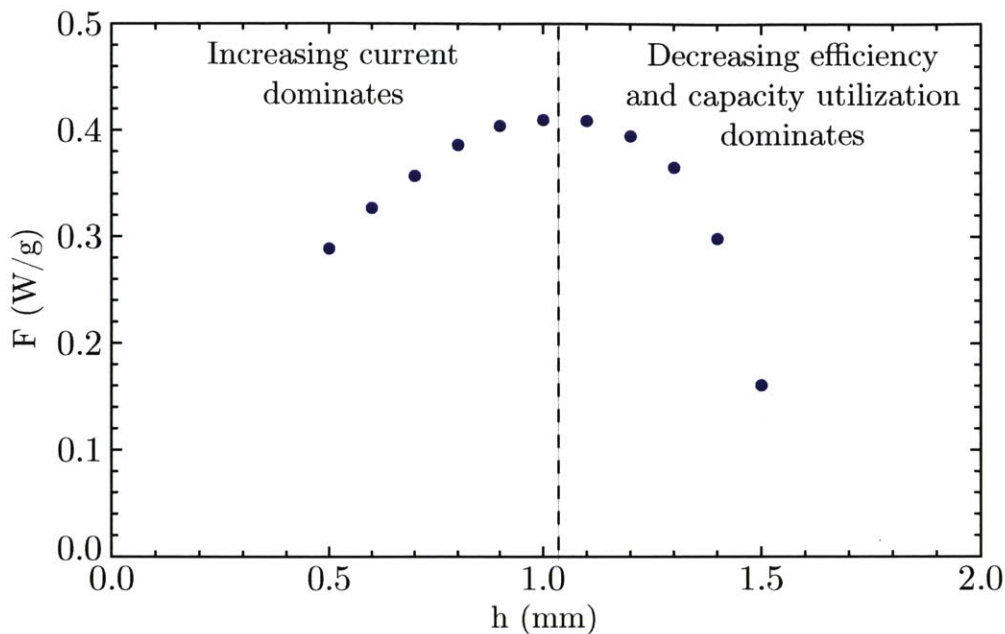
Figure 4-6: Plot showing the effect of h on the figure of merit, F. Data points are calculated based on a single simulated charge/discharge cycle run at C/3 rate.

interface compared to the planar channel geometry is designed to reduce the potential drop across that interface since the larger current collector surface area will reduce the current density across the interface. The current collector fins also serve to reduce the electron transport distance (and therefore ohmic drop in the conductive matrix), in particular this should allow for better performance from channels with larger h when compared to the planar channel geometry.

While the goal is to improve electrochemical performance relative to the planar channel geometry, performance is still expected to decrease as both geometric parameters (w and h) increase. As w increases the electron transport distance from the current collector to the center of the channel increases, leading to larger ohmic losses as a result of the electronic current transport in the carbon network. Additionally, as w increases the ratio of current collector surface area to membrane surface area decreases. Since the current density (per unit separator area) remains constant at constant C-rate this results in a larger potential drop across the current collector-suspension interface and therefore higher polarization. Figure 4-7 shows modeled voltage profiles of both charge and discharge for rectangular channels with $h = 1$ mm

Figure 4-7: Modeled voltage profiles upon charge and discharge for rectangular candidate channels with $h = 1$ mm and $w = [0.5, 1.5, 2.5, 3.5]$ mm. Higher polarization and lower discharge capacity are observed as channel width increases as a result of longer electron transport distances and larger ohmic potential drop at the current collector-suspension interface. All simulations are for C/3 rate.

and varying width. As the channel width increases higher polarization and lower capacity utilization are apparent, particularly for the discharge simulations.

Decreased electrochemical performance is also expected as the channel height (electrode thickness) increases. As h increases the current density (per unit separator area) must increase proportionally to maintain the same C-rate, leading to an increase in polarization. Additionally, as h increases the Li$^+$ transport distance increases. This results in larger ionic resistance in the cell and can lead to salt depletion within regions of the electrode that dramatically decreases the usable capacity of the cell. As a result of these two factors increasing h leads to greater decreases in electrochemical performance than increasing w. These effects are seen in Fig. 4-8, which shows modeled voltage profiles on charge and discharge for rectangular channels with $w = 0.5$ mm and varying width. As was the case in Fig. 4-7 the increase in polarization and decrease in usable capacity is larger on discharge than on charge.

While electrochemical performance is observed to decrease as h increases as expected, one must compare the results to the planar channel geometry to observe the benefits of the additional current collector material in rectangular geometry. Comparing the polarization on both charge and discharge for the rectangular geometries in Fig. 4-8 to the polarization for the planar channels in Fig. 4-5 makes it clear that
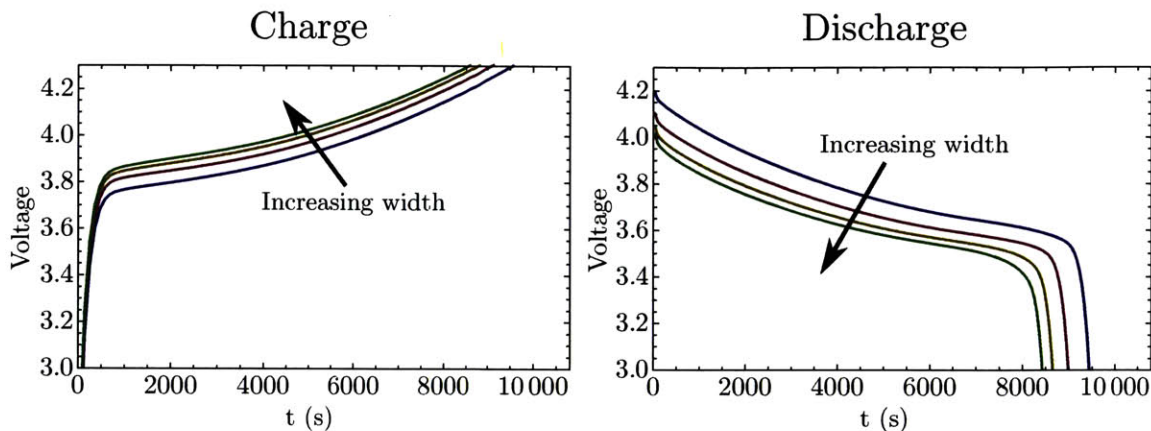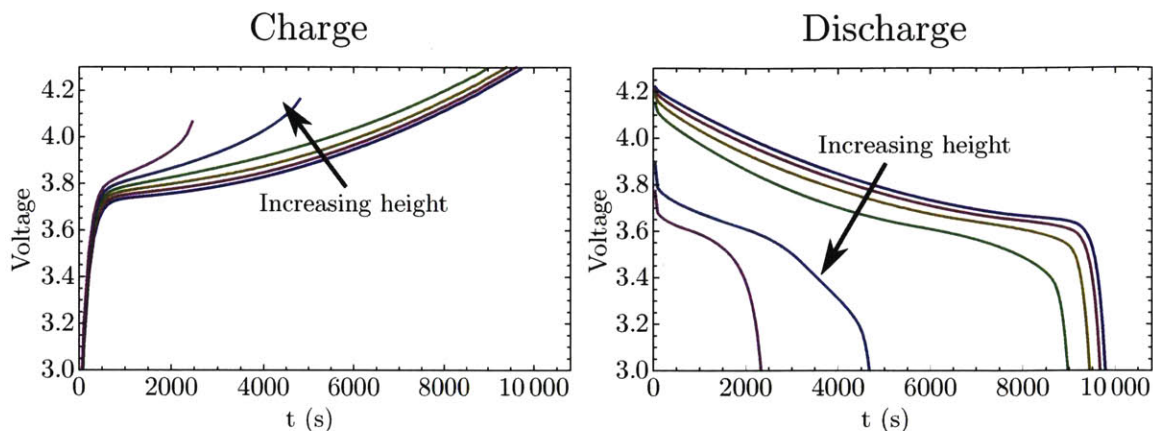
Figure 4-8: Modeled voltage profiles upon charge and discharge for rectangular candidate channels with $w = 0.5$ mm and $h = [0.5, 0.75, 1.0, 1.25, 1.5, 1.75]$ mm. Higher polarization and lower discharge capacity are observed as channel height increases. All simulations are for C/3 rate.

the rectangular channel geometry noticeably improves electrochemical performance between cells with the same h. The important question remaining is whether these performance gains are worth the additional inactive mass required for the rectangular channel geometry.

In order to address this question and balance the gains in electrochemical performance from smaller channel dimensions with the additional cost the figure of merit $F(h, w)$ is used again. $F(h, w)$ is calculated based on the results of the C/3 cycle simulations for each set of geometric parameters, and the results are shown in Fig. 4-9. From the contour plot in Fig. 4-9 it is apparent that increasing h is beneficial up to ≈ 1.1 mm for all texted channel widths. Beyond $h = 1.1$ mm electrochemical performance drops off as seen in Fig. 4-8, but up to that point the losses in terms of electrochemical performance are outweighed by reductions in the amount of inactive material needed, leading to an overall improvement in the figure of merit. Above $h = 1.4$ mm salt depletion at the Li-foil anode occurs during charging, leading to a dramatic decrease in the % utilization of theoretical capacity and therefore a steep decrease in F. A similar effect is seen as w increases. Since the electrochemical performance losses are relatively small (and fairly constant) for the range of w tested, these losses are once again outweighed by the reduced amount of inactive material

in the system. Therefore F increases with channel width for rectangular channels within the tested range.

4.3.3 Saw-Tooth Geometry

Similarly to the rectangular channel geometry electrochemical performance is expected to decrease with both h and w for the saw-tooth channel geometry. However, because more of the suspension in the saw-tooth design is closer to the separator when compared to the rectangular cross-section, thicker electrodes are expected to perform better than the rectangular geometry of equivalent h.

Figure 4-10 shows the modeled voltage profiles on charge and discharge for saw-tooth channels with $h = 1.5$ mm and varying width. As was the case for the rectangular cross-section channels, higher polarization and lower capacity utilization is evident as channel width increases. This is expected once again since the ratio of current collector area to separator area decreases with increasing w, resulting in larger potential drop at the current collector-suspension interface.

Figure 4-11 shows the effect of increasing h while maintaining a constant channel width ($w = 1$ mm) on the charge and discharge voltage profiles for simulated cycling at C/3 rate. Similarly to the rectangular cross-section case the electrochemical performance losses are greater when increasing h than when increasing w. This occurs because increasing h increases the current density (per unit separator area) applied to the cell, increases the ionic resistance of the cell, and finally leads to salt depletion for sufficiently large values of h.

Based on the similar trends in electrochemical performance for the rectangular and saw-tooth cross-section channels it is reasonable to expect that the figure of merit for the saw-tooth geometry will also resemble that of the rectangular geometry. Figure 4-12 shows the variation of $F(h, w)$ for the saw-tooth channel geometry. As expected the general trends are quite similar to those seen in Fig. 4-9 for the rectangular geometries except for the onset of salt depletion at the anode. Once again, the figure of merit increases with h up to a point before dropping off as a result of reduced electrochemical performance. However, the optimum value of h is larger for the saw-tooth cross-

Figure 4-9: Contour and surface plots showing the value of the figure of merit, F (W/g), as a function of geometric parameters for rectangular candidate channel geometries. Based on a single simulated charge/discharge cycle run at C/3 rate. Increasing channel height improves F up to ≈ 1.1 mm as a result of increasing current, beyond that decreasing energy efficiency and capacity utilization counteract the higher current. In general, F increases with w and will asymptotically approach the value for a planar geometry of equivalent h.
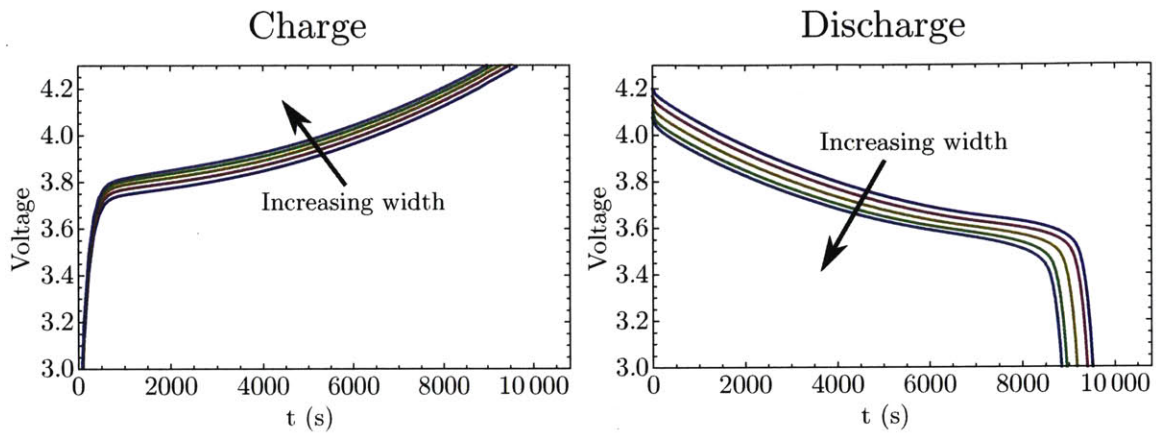
Figure 4-10: Modeled voltage profiles upon charge and discharge for saw-tooth candidate channels with $h = 1.5$ mm and $w = [0.5, 1.0, 1.5, 2.0, 2.5]$ mm. Higher polarization and lower discharge capacity are observed as channel width increases as a result of longer electron transport distances and larger ohmic potential drop at the current collector-suspension interface. All simulations are for C/3 rate.
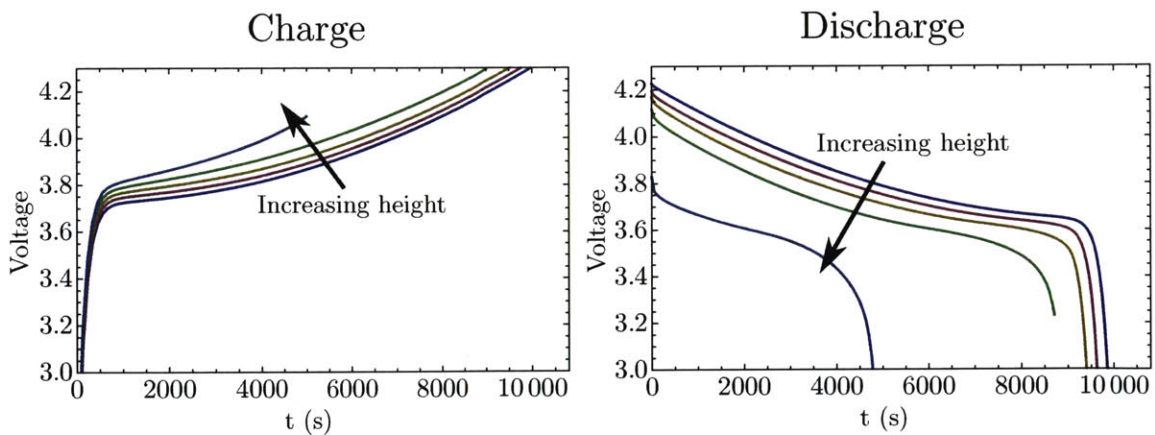
Figure 4-11: Modeled voltage profiles upon charge and discharge for saw-tooth candidate channels with $w = 1$ mm and $h = [0.5, 1.0, 1.5, 2.0, 2.5]$ mm. Higher polarization and lower discharge capacity are observed as channel height increases. All simulations are for C/3 rate.

section, around 1.5 mm, compared to 1.1 mm for the rectangular channels. F also generally increases with w as a result of the corresponding decrease in inactive mass fraction. The most notable difference between the saw-tooth and rectangular channel geometries relates to the onset of salt depletion at the anode during charging which leads to a sudden increase in polarization and therefore a dramatic reduction in the % of theoretical capacity that is accessible. For the rectangular channel geometries this salt depletion effect was seen above $h = 1.4$ mm, but did not have any w dependence. However, in the saw-tooth geometry the h value at which the onset of salt depletion occurs decreases as w increases. This leads to an optimum saw-tooth geometry near $w = 2.75$ mm and $h = 1.5$ mm.

Based on Fig. 4-12 and Fig. 4-9 the maximum figure of merit for the rectangular channel geometries is ≈ 0.33 W/g, while the maximum for the saw-tooth channels is ≈ 0.26 W/g. Therefore the rectangular channel geometry is better in terms of the amount of power produced per unit mass of inactive material which F is designed to measure. However, for some applications volumetric energy density is more important than specific energy density and the saw-tooth channel geometries perform better in that respect. To compare channel geometries in terms of power produced per unit volume a second figure of merit, F_{vol} is used. F_{vol} is defined using the same measure of power as F, but normalizing by channel volume rather than inactive mass:

$$F_{vol} = \frac{P}{V_{cell}} \cdot \eta_{energy} \cdot \eta_{capacity} \qquad (4.5)$$

Contour plots of F_{vol} for the rectangular and saw-tooth candidate geometries are shown in Fig. 4-13 and Fig. 4-14 respectively. As seen in these two figures the saw-tooth channel geometry is capable of higher power per unit volume than the rectangular channel geometry with a maximum $F_{vol} \approx 81$ W/L compared to $F_{vol} \approx 67$ W/L for the rectangular cross-section.
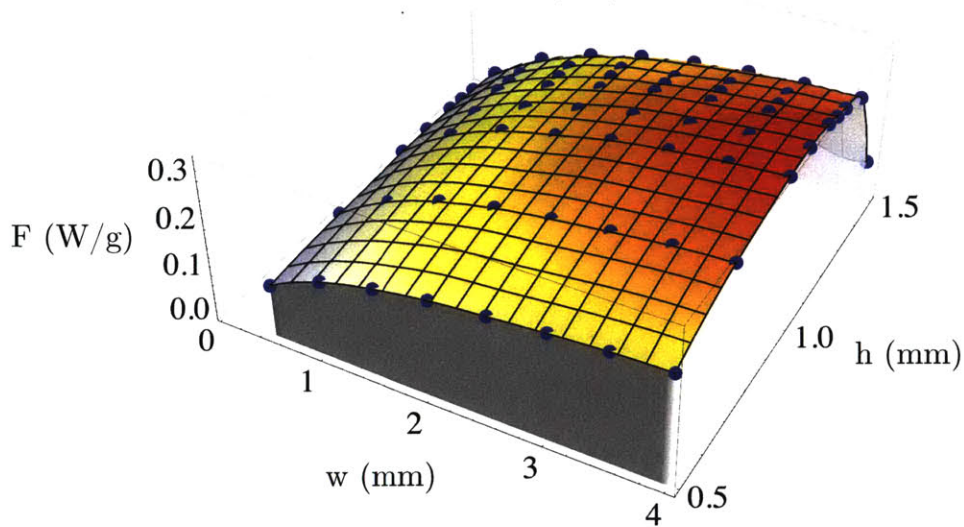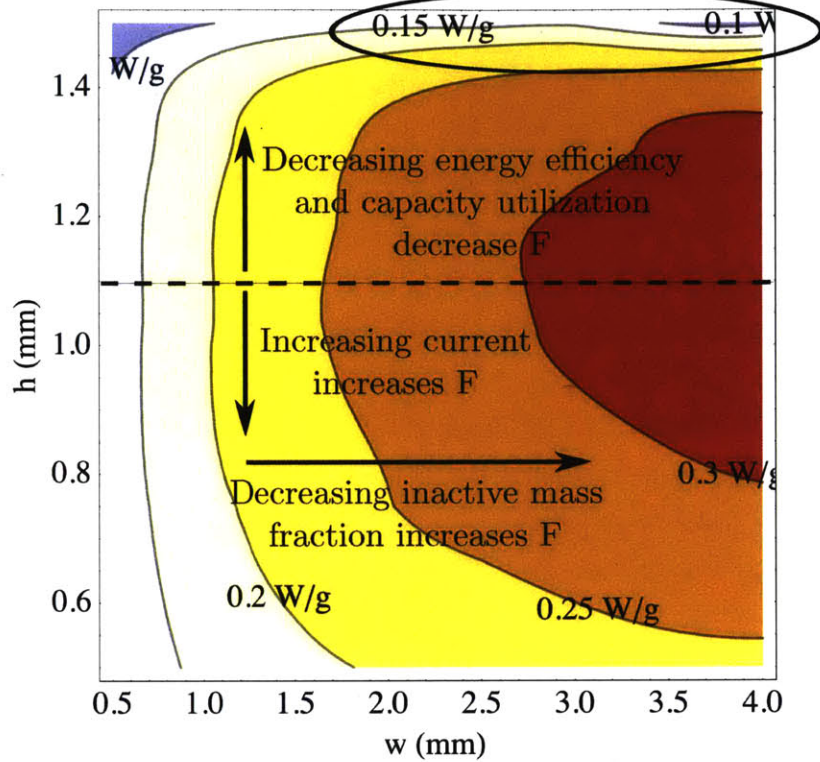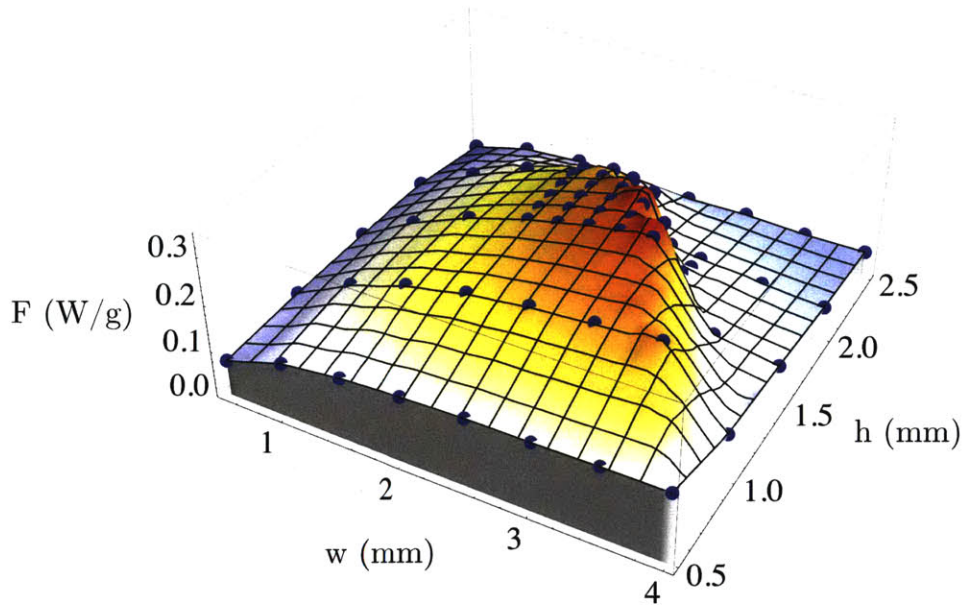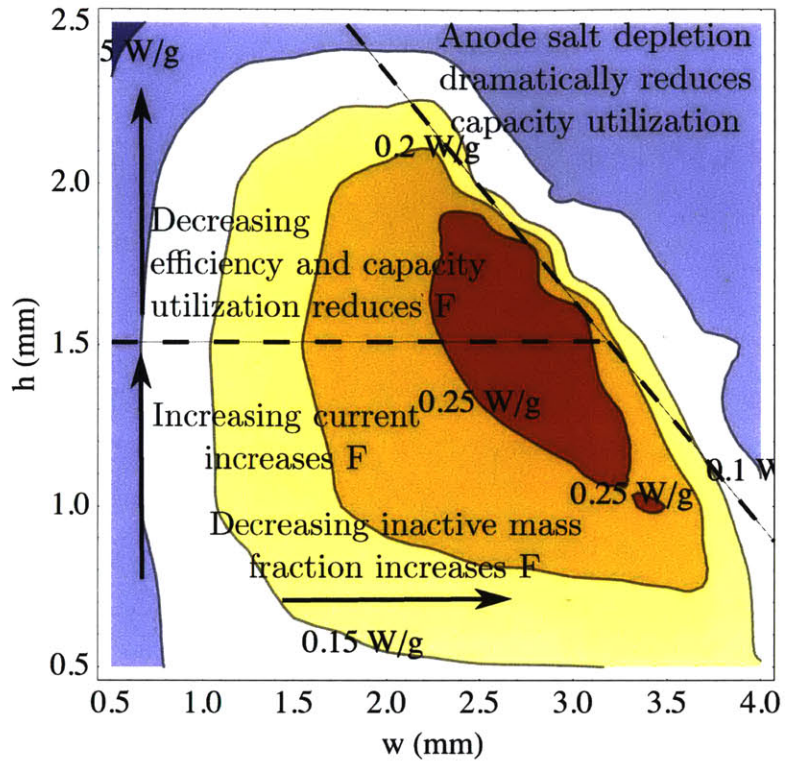
Figure 4-12: Contour and surface plots showing the value of the figure of merit, F, as a function of geometric parameters for saw-tooth candidate geometry. Based on a single simulated charge/discharge cycle run at C/3 rate.
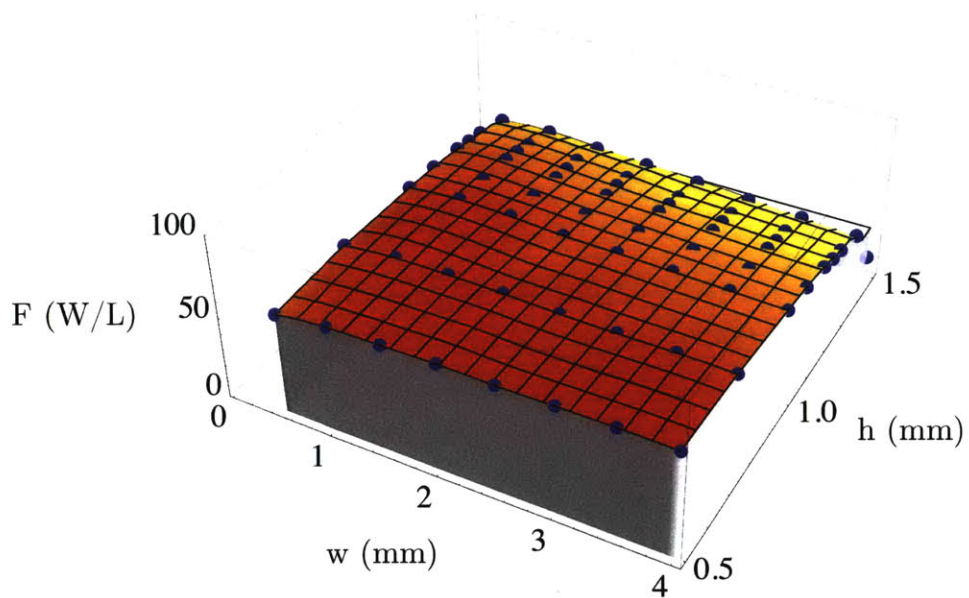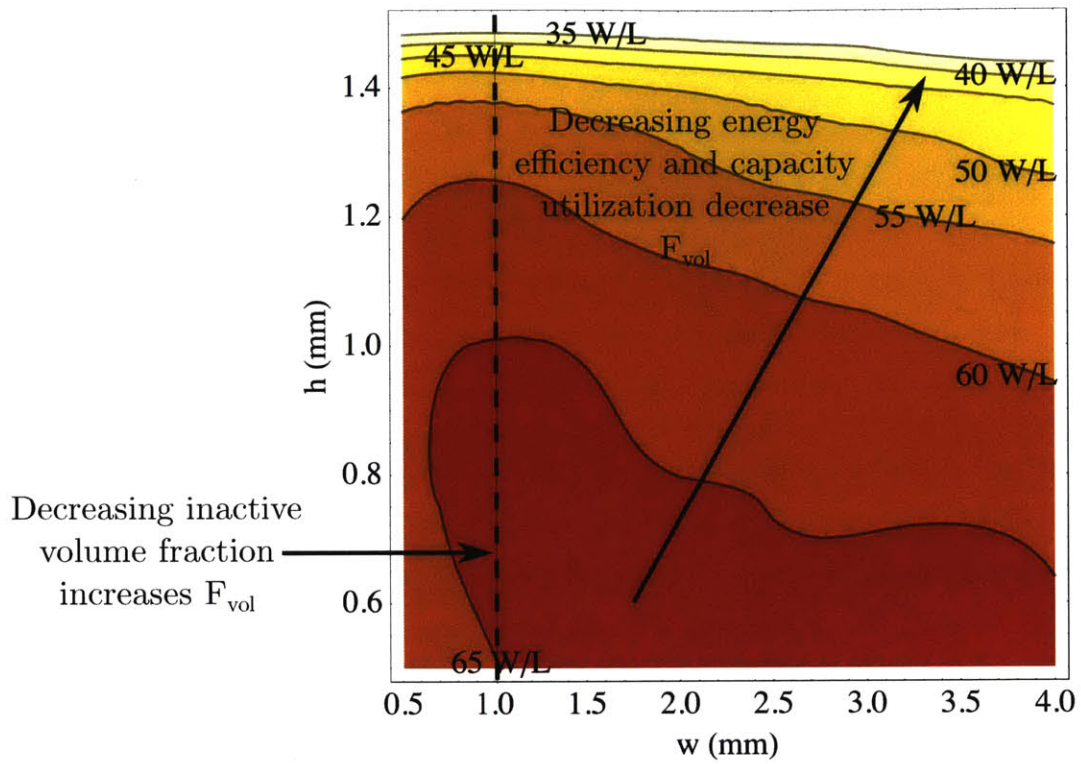
Figure 4-13: Contour plot showing the variation of $F_{vol}(h, w)$ for rectangular candidate channel geometries. Based on simulated cycling at C/3.
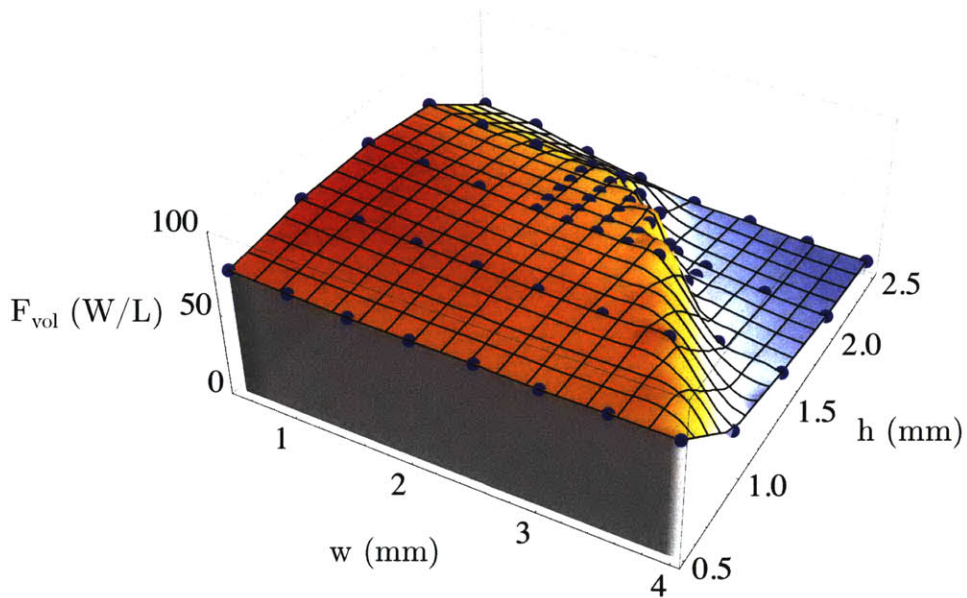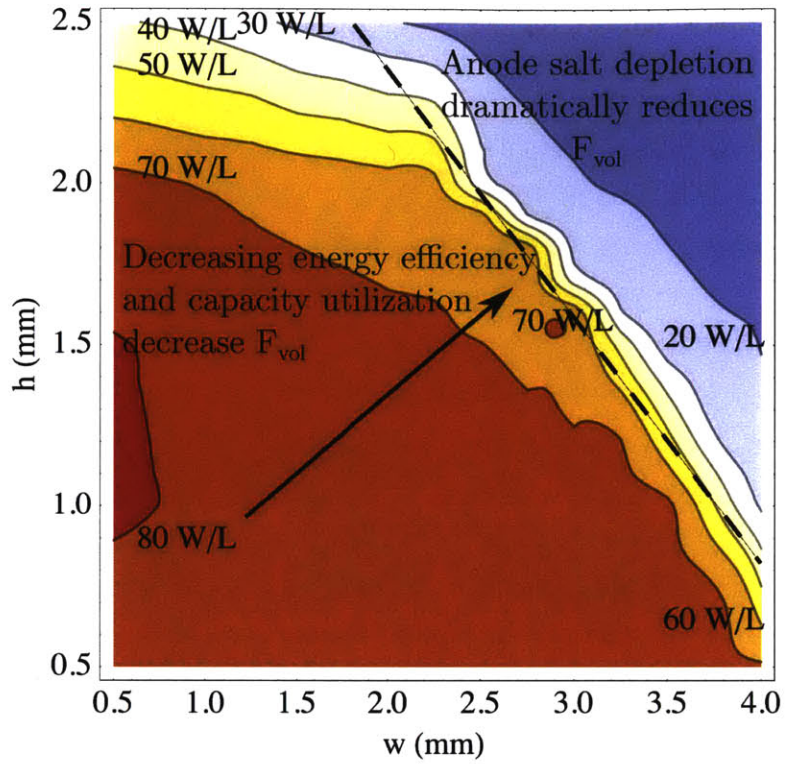
Figure 4-14: Contour plot showing the variation of $F_{vol}(h, w)$ for saw-tooth candidate channel geometries. Based on simulated cycling at C/3.

4.4 Discussion

Based on the results presented in Section 4.3 it is clear that the channel geometry used in an SSFC power stack can dramatically affect its electrochemical performance. For all three candidate geometries examined in this work electrochemical performance is seen to decrease dramatically as flow channel thickness increases. This result is quite reasonable considering the knowledge from conventional Li-ion batteries that rate capability scales roughly with the square of electrode thickness since both the cell resistance and applied current needed to maintain a constant C-rate increase with thickness. In addition, for the rectangular and saw-tooth candidate geometries see an increase in electrochemical performance as the channel width, w, decreases. The initial motivation for considering these geometries was the expectation that additional current collector surface area would improve performance by reducing the potential drop resulting from the current collector-suspension interfacial resistance and would also reduce electron transport distances (and therefore ohmic losses in the conductive network), so the observed results are in line with expectations. Despite this the gains in electrochemical performance from decreasing channel width are relatively modest in comparison to the changes seen when varying h. Therefore, considering only electrochemical behavior the optimal flow channel geometry for use in the power stack would be rectangular or saw-tooth with a small w and small h.

However, as discussed in Section 4.2.2, it is necessary to consider the "cost" associated with each potential geometry in order to optimize the geometry for practical use. In this work the figure of merit, $F(w, h)$, used to compare geometries normalizes gains in electrochemical performance by the total mass of inactive components associated with each geometry. This measure was selected because the inactive components in a flow battery system are a significant contributor to overall system cost and reduce system level energy density, as a result it is desirable to minimize the amount of inactive material in the system. It is important to note that this is not the only reasonable choice for a figure of merit, in practice it may be more important to minimize total system volume or monetary cost for a particular application.

99

Taking into account the "cost" in terms of inactive component mass favors larger flow channel dimensions than would be selected based only on electrochemical performance. For the planar candidate geometry the maximum in $F(h)$ occurs around $h = 1.1$ mm at a value of $F = 0.41$ as seen in Fig. 4-6. For the rectangular candidate geometry $F(w, h)$ exhibits a maximum near $h = 1.1$ mm for all values of w as seen in Fig. 4-9. Interestingly, while electrochemical performance is observed to improve as w decreases the opposite is seen for $F(w, h)$. This suggests that the electrochemical performance gains are outweighed by the additional inactive material needed to construct a cell using smaller flow channels. In fact, the highest figure of merit observed in the tested range of w, h occurs at $w = 4.0$ mm and $h = 1.0$ mm with $F = 0.33$. Figure 4-15 shows the change in $F(w, h)$ as w increases with constant $h = 1.0$ mm. Based on these results it is expected that $F(w, h)$ will continue increasing with w and eventually asymptotically approach the value for the planar candidate geometry with $h = 1.0$ mm. The case is similar for the saw-tooth candidate geometry. The saw-tooth geometry exhibits a maximum in $F(w, h)$ around $h = 1.5$ mm with F increasing with w as in the rectangular case. In general F is approximately 90% of the value for a rectangular geometry with similar w and h, however as seen in Figures 4-13 and 4-14 the saw-tooth geometry performs somewhat better than the rectangular geometry in terms of maximimizing power per unit volume.

Considering these results a planar flow channel of depth $h = 1.1$ mm is optimal for maximizing power output per unit mass of inactive material. However, some prior experiments performed using wide flow channels (> 5 mm) exhibited significant separator bowing that negatively affected capacity matching between anode and cathode material in the flow cell. As a result, using a planar flow geometry is likely to require some additional material to provide mechanical support to the separator. The addition of this inactive support material will decrease F, and therefore it may be an improvement to use a rectangular channel geometry with w determined by the maximum acceptable amount of separator bowing.

These results demonstrate the value of using a continuum model solved with finite element methods to rapidly evaluate a large parameter space and optimize flow
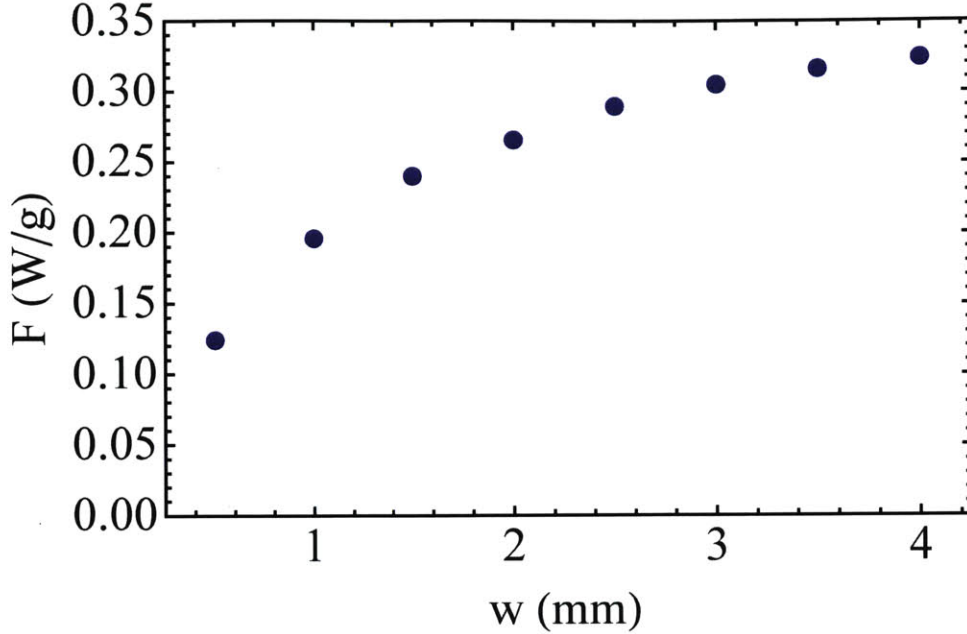
Figure 4-15: Plot of $F(w, h)$ for rectangular geometries with $h = 1.0$ mm. $F(w, h)$ increases with w and is expected to asymptotically approach the value of $F(1.0 \text{ mm})$ for the planar geometry.

channel geometry. However, it is important to remember that the results presented here are only relevant for the specific 20 vol% NMC suspension that was modeled. Higher loading (therefore higher volumetric capacity) suspensions are likely to require shallower flow channels to achieve similar rate performance. Similarly, use of a different active material at a similar loading may result in a different optimal channel geometry. In particular, in the earlier chapters of this work active materials with broad plateaus in the equilibrium voltage were investigated and were seen to cycle by first charging or discharging material nearest the current collector with the "phase boundary" that developed moving inwards as the charge (or discharge) process proceeded. This is very different than the case for the NMC suspension tested in this chapter where the intercalation reaction proceeds much more uniformly throughout the cell as a result of the continously varying $V_{eq}(SOC)$. This difference may favor rectangular channel geometries with small w more strongly than the is the case for the NMC results seen here.

Another important factor to consider is the choice of figure of merit. Recall that

the optimization here was intended for a 1 kW/1 kWh system, which is a relatively small power-to-energy ratio of 1 and therefore achieving high cell power is very important. When optimizing for a different system, for example one with a P/E ratio of 1/10 a figure of merit that more heavily weighs the total amount of suspension needed to meet the energy requirements of the system may be a better choice.

Ultimately, the particular optimum geometry for the specific NMC suspension examined in this work is not the most important take-away of this work. More important is the demonstration that this continuum model for SSFC performance can be effectively used as a design tool, allowing one to rapidly explore a large geometric parameter space to compare performance (as measured by a figure of merit relevant to the specific application) in order to optimize flow channel geometry.

Chapter 5

Conclusions

In this thesis a three-dimensional continuum model for semi-solid flow battery performance incorporating both electrochemical and hydrodynamic behavior has been developed. Finite element methods are used to solve the governing equations of the model, and the results presented seek to address several important questions that are either challenging to tackle experimentally, or that greater insight into the physical problem can be obtained from the additional information that modeling enables (e.g. state of charge distributions during cycling, spatial distributions of salt concentration, etc.). The first two main questions addressed focus on understanding two important modes of operation for semi-solid flow batteries (or other high viscosity flow battery systems). Chapter 2 addresses the importance of active material selection to enable efficient SSFC operation in stoichiometric flow mode. Chapter 3 uses the model and comparisons with experimental data to both validate the model and better understand the extended electrochemically active zone with the goal of improving performance during intermittent flow operation. Finally, Chapter 4 demonstrates the value of using this model as a design tool for optimizing the flow channels used in an SSFC power stack by exploring a wide geometric parameter space more rapidly and cheaply than is possible to do experimentally. The remainder of this chapter summarizes the important results and relevant conclusions from each earlier chapter, and also discusses some interesting directions for future work.

5.1 Modes of Operation to Minimize Pumping Losses in Flow Batteries with High Viscosity Electrodes

As seen in Section 1.3 the energy lost to pumping is an important concern for SSFC systems because of the very high viscosity of the semi-solid electrode suspensions. As a result it is necessary to operate in either stoichiometric or intermittent flow mode. Either of these modes is capable of reducing pumping energy losses to $< 1\%$, however each comes with some important operational challenges that have been addressed in this work.

5.1.1 Importance of Active Material Selection for Efficient Stoichiometric Flow Operation

Stoichiometric flow operation corresponds to the limit of continuous flow operation in which active material enters the stack fully discharged and is fully charged in a single pass (or vice versa for discharge). This has important implications for flow battery performance because active material across the full range of state of charge is present in the stack at any given time. Many active materials have equilibrium voltage profiles that vary continuously as a function of state of charge (for example LCO in an SSFC or the electrolyte solutions used in conventional aqueous flow batteries). For these materials the gradients in state of charge within the power stack during stoichiometric flow operation lead to gradients in the local overpotential, and therefore non-uniform current density distributions along the length of flow channel. This non-uniform current density distribution has several negative effects: it leads to increased polarization, higher localized current density will lead to local ohmic heating with potential performance and safety implications, and finally at steady state $> 90\%$ of the current is entering a third or less of the flow channel (see Fig. 2-3) so much of the inactive material going into cell construction is effectively wasted.

One of the advantages of the semi-solid flow battery architecture is that in prin-

ciple any solid can be used as the active storage compound. This is important for stoichiometric operation because compounds like LFP or LTO that exhibit a plateau in equilibrium potential across the majority of their capacity range can be used. For these phase change materials the gradients in state of charge present during stoichiometric flow operation do not lead to gradients in overpotential, and therefore much more uniform current density distributions are possible. Thus, by using an informed choice of active storage compound in the semi-solid electrodes it is possible to achieve improved performance during stoichiometric flow operation. Alternatively, if a material like LCO or NMC with a constantly sloping equilibrium potential is to be used the results of this work suggest two possibilities for improving performance. One possibility is using an anode material with a similarly sloping V_{eq} profile and flowing the cathode and anode suspensions in opposing directions so that the cell potential remains roughly constant along the length of the flow channel. Unfortunately, this approach is somewhat limited by the difficulty in matching anode and cathode voltage profiles to achieve a constant cell potential. The second possibility is to divide the power stack into multiple electrically insulated regions and enforce a more uniform current density distribution by allowing the potential of each current collector region to differ. One possible downside of this approach is the development of shunt currents between current collector regions at different potentials connected by the conductive network present in the semi-solid electrode suspension.

Ultimately the main conclusion here is that non-uniform current density distributions are important for stoichiometric flow operation, and that their potential negative effects can be mitigated by clever selection of the active storage compound in a semi-solid flow battery. It is also important to note that this general conclusion is expected to be applicable to other new high-energy density flow battery systems that are sufficiently viscous to require either stoichiometric or intermittent operation.

5.1.2 Extended Electrochemically Active Zone Concerns for Intermittent Flow Operation

Semi-solid flow batteries are the first in a new class of flow battery systems where the electronic conductivity that enables the electrochemical reaction to proceed is not provided by a fixed electrode (e.g. a porous carbon mesh or similar) attached to the current collector in the power stack. In a semi-solid flow battery the conductive carbon suspended in the electrolyte forms a percolating network, effectively turning the entire electrode suspension into a liquid wire and providing the electronic conductivity necessary for electrochemical operation. This provides an interesting challenge for operating in intermittent flow mode because the size of the electrochemically active zone (EAZ) is unknown. In principle the EAZ could extend all the way through the electrode feed pipes into the storage tanks when operating at an infinitesimally slow rate. In practice, the EAZ is unlikely to extend that far when running at finite current, however it is important to understand how far it does extend in order to know how much suspension must be pumped between cycles during intermittent operation.

Based on the modeling results presented in Chapter 3 and comparison with experimental data several conclusions may be drawn. First, the comparison with experimental data validates the usefulness of the model for understanding SSFC operation. Second, based on the comparison of experimental and modeled voltage profiles as well as the time evolution of the spatial distribution of intercalated Li it is apparent that there are two regimes of extended-EAZ behavior. The first regime occurs in all SSFCs when some Li intercalates into active particles near the end of the current collector throughout the lithiation process. In this regime, the size of the extended-EAZ is a function of the current *density* applied to the system as well as the electrode suspension properties (most notably the electronic conductivity). The second regime occurs near the end of lithiation in SSFCs where the *total* current is small. In this regime all of the active material in the current collector region as well as the first EAZ regime has already been lithiated, and there is a "phase boundary" separating regions of lithiated and delithiated suspension. Because the *total* current is small in

systems where the second regime is relevant, it is possible for all of the current to flow outwards into the extended-EAZ without immediately hitting the voltage cutoff limits, resulting in the movement of the "phase boundary" outwards until the ohmic polarization is sufficient to reach the cutoff limit. This is seen in the voltage profile as an extended linear "tail" region at the end of the lithiation process, and becomes more pronounced for shorter current collector systems and lower C-rates where the total current is smaller. The difference between these two regimes is illustrated in Fig. 3-8. Because the second extended-EAZ regime is only relevant for cells operating at sufficiently small *total* current it is unlikely to be important for a full-scale SSFC system, only the smaller first regime extended-EAZ will be present and it was observed to be < 1 mm.

The next major result from modeling of the extended-EAZ relates to the development of anisotropic electronic conductivity as a result of flow induced particle migration and its effects on electrochemical performance. Prior work by Dr. Bryan Ho clearly demonstrates that the semi-solid electrode suspensions used in SSFCs are prone to segregation based on particle size during flow, with the smaller carbon black particles migrating to high shear rate regions near the flow channel walls [32]. This creates a highly conductive layer of material on the channel walls which leads to significantly higher electronic conductivity parallel to the direction of flow than perpendicular to it. Comparisons of modeled and experimental voltage profiles presented in Chapter 3 provide the first clear evidence of this anisotropy affecting electrochemical performance. It was observed that the slope of the plateau in the voltage profile depends primarily on the electronic conductivity between the current collector and separator, while the slope of the long tail in the voltage profile (corresponding to the second regime of extended-EAZ) depends primarily on the electronic conductivity parallel to the flow direction. Attempts to model the system using an isotropic conductivity can provide a good match to experimental data for either the plateau slope or tail slope, but not both. Altering the model to incorporate a higher electronic conductivity parallel to the flow direction produces voltage profiles that more closely resemble the experimental data. This observation in combination with the charac-

terization work of Ho provides good evidence that the development of anisotropic conductivity as a result of microstructural changes during flow is a potentially important phenomenon for SSFC operation.

The final important result of the extended-EAZ study concerns the first cycle capacity loss consistently observed in experimental data. One hypothesis that potentially explains this observation is that the extended-EAZ is larger for lithiation than delithiation so that some of the Li intercalated during the first lithiation is inaccessible during the first delithiation. The modeling results presented in Fig. 3-11 support a similar conclusion where an equilibration process that occurs in the extended-EAZ during delithiation makes some of the initially intercalated Li inaccessible during the first delithiation cycle. While this qualitative result is informative, the model only predicts a coulombic inefficiency of $\approx$ 5%, while the experimentally observed inefficiency is significantly larger. Further work is needed to better understand the difference between the modeled and experimental voltage profiles on delithiation and to explain the remaining coulombic inefficiency. The remaining coulombic inefficiency is believed to most likely be the result of an unmodeled side reaction.

Ultimately, the result with the most importance for practical operation of an SSFC in intermittent flow mode is the discovery of the two regimes of extended-EAZ behavior. Since full-scale SSFC systems will be much larger than the lab-scale experimental setup used in this work and will run at much higher *total* currents only the first current *density* dependent regime is expected to be relevant, and its size will be small relative to the total volume of electrode suspension contained in the power stack. Therefore in a full-scale system the pumping volume during intermittent operation should not differ significantly from the active cell volume.

5.2   Use of Continuum Modeling as a Design Tool for Flow Battery Power Stacks

In addition to addressing important issues related to potential modes of operation for semi-solid flow batteries the final primary goal of this thesis is to demonstrate the value of the continuum model developed herein as a design tool for developing flow battery power stacks. Chapter 4 demonstrates the capability of using the models governing equations solved with commerically available finite element software to rapidly and cheaply evaluate a broad geometric parameter space and select the optimal geometry from the available candidates. When attempting to optimize channel geometry it is important to use a figure of merit relevant to the particular application the geometry is designed for. This work suggests a figure of merit based on the power produced per unit mass of inactive material that also incorporates some measures of electrochemical efficiency and utilization of the available active material capacity.

Rectangular and saw-tooth channel geometries are observed to improve electrochemical performance compared to planar geometries with the same channel thickness, however they require significantly more inactive mass to achieve this improved performance. Based on the model results the addition of this inactive mass outweighs the electrochemical gains and therefore a planar flow channel geometry of thickness $h = 1.1$ mm maximizes the figure of merit. However, this geometry is likely to require some additional inactive material to provide mechanical support for the separator. As a result a rectangular geometry using the minimum amount of material to support the separator may be preferable. While the results of this particular optimization are useful, the more important take-away is that this modeling framework can be successfully used as a design tool.

5.3   Directions for Future Work

The lessons learned during the course of this thesis research suggest several interesting avenues for future related work. One of the concerns discussed in Chapter 2 relates

to the local ohmic heating resulting from the non-uniform current density, however the model presented in this work is isothermal. Incorporating thermal effects into the SSFC model presented here is certainly an interesting area for future investigation. Some prior work exists incorporating thermal effects into models for Li-ion batteries, however they do not need to include the convective effects present in a semi-solid flow battery system [57, 58]. One major challenge in incorporating thermal effects into the existing model will be doing so in a computationally efficient manner since the computational requirements for the existing model are already significant.

A second area for further work is motivated by the development of anisotropic conductivity discussed in Chapter 3. Developing a model that relates microstructural changes (e.g. particle segregation and local porosity changes) to local flow conditions (e.g. pressure, shear rate, etc.) and determines their effect on the suspension properties that go into the electrochemical model presented here would be a valuable contribution. A fully coupled model incorporating the flow, electrochemistry, and microstructural evolution is likely to be a significant computational challenge, as a result a multi-scale modeling approach may be preferable.

In terms of use of the finite element model presented here as a design tool there is potential for the addition of a more advanced optimization process. This work demonstrates the ability to use the model to rapidly examine a broad geometric parameter space, however more advanced optimization procedures are possible that can automatically refine geometries based on the results of finite element modeling. A great deal of research is available on using finite element methods for geometric optimization in other fields and applying the methods that have been developed to flow-battery design would be a useful contribution [59–62].

Bibliography

[1] John A Turner. A realizable renewable energy future. *Science*, 285(5428):687–689, July 1999.

[2] Ibrahim Dincer. Renewable energy and sustainable development: a crucial review. *Renewable and Sustainable Energy Reviews*, 4(2):157–175, June 2000.

[3] Martin I Hoffert, Ken Caldeira, Gregory Benford, David R Criswell, Christopher Green, Howard Herzog, Atul K Jain, Haroon S Kheshgi, Klaus S Lackner, John S Lewis, H. Douglas Lightfoot, Wallace Manheimer, John C Mankins, Michael E Mauel, L. John Perkins, Michael E Schlesinger, Tyler Volk, and Tom M. L Wigley. Advanced technology paths to global climate stability: Energy for a greenhouse planet. *Science*, 298(5595):981–987, November 2002.

[4] R.E.H. Sims. Renewable energy: a response to climate change. *Solar Energy*, 76 (13):9–17, January 2004.

[5] Henrik Lund. Renewable energy strategies for sustainable development. *Energy*, 32(6):912–919, June 2007.

[6] R. K. Pachauri and A. Reisinger. *IPCC, 2007: Climate Change 2007: Synthesis Report. Contribution of Working Groups I, II and III to the Fourth Assessment Report of the Intergovernmental Panel on Climate Change.* IPCC, Geneva, Switzerland, 2007.

[7] Advanced Research Projects Agency Energy. Funding Opportunity Announcement - Batteries For Electrical Energy Storage in Transportation (BEEST), December 2009.

[8] United States Advanced Battery Consortium (United States Council on Automotive Research). USABC Goals for Advanced Batteries for EVs.

[9] H. Ibrahim, A. Ilinca, and J. Perron. Energy storage systems - Characteristics and comparisons. *Renewable and Sustainable Energy Reviews*, 12(5):1221–1250, June 2008.

[10] J.P. Deane, B.P. Gallachir, and E.J. McKeogh. Techno-economic review of existing and new pumped hydro energy storage plant. *Renewable and Sustainable Energy Reviews*, 14(4):1293–1302, May 2010.

[11] Advanced Research Projects Agency Energy. Funding Opportunity Announcement - Grid-Scale Rampable Intermittent Dispatchable Storage (GRIDS), March 2010.

[12] Mihai Duduta, Bryan Ho, Vanessa C Wood, Pimpa Limthongkul, Victor E Brunini, W. Craig Carter, and Yet-Ming Chiang. Semi-Solid lithium rechargeable flow battery. *Advanced Energy Materials*, page n/an/a, 2011.

[13] C. Ponce de Leon, A. Frias-Ferrer, J. Gonzalez-Garcia, D.A. Szonto, and F.C. Walsh. Redox flow cells for energy conversion. *Journal of Power Sources*, 160 (1):716–732, September 2006.

[14] Y. Matsuda, K. Tanaka, M. Okada, Y. Takasu, M. Morita, and T. Matsumura-Inoue. A rechargeable redox battery utilizing ruthenium complexes with non-aqueous organic electrolyte. *Journal of Applied Electrochemistry*, 18(6):909–914, 1988.

[15] M.H. Chakrabarti, R.A.W. Dryfe, and E.P.L. Roberts. Evaluation of electrolytes for redox flow battery applications. *Electrochimica Acta*, 52(5):2189–2195, January 2007.

[16] Qinghua Liu, Alice E.S. Sleightholme, Aaron A. Shinkle, Yongdan Li, and Levi T. Thompson. Non-aqueous vanadium acetylacetonate electrolyte for redox flow batteries. *Electrochemistry Communications*, 11(12):2312–2315, December 2009.

[17] Qinghua Liu, Aaron A. Shinkle, Yongdan Li, Charles W. Monroe, Levi T. Thompson, and Alice E.S. Sleightholme. Non-aqueous chromium acetylacetonate electrolyte for redox flow batteries. *Electrochemistry Communications*, 12 (11):1634–1637, November 2010.

[18] Ch Fabjan, J Garche, B Harrer, L Jrissen, C Kolbeck, F Philippi, G Tomazic, and F Wagner. The vanadium redox-battery: an efficient storage unit for photovoltaic systems. *Electrochimica Acta*, 47(5):825–831, December 2001.

[19] Claus Daniel. Materials and processing for lithium-ion batteries. *JOM Journal of the Minerals, Metals and Materials Society*, 60(9):43–48, 2008.

[20] Zhenguo Yang, Jun Liu, Suresh Baskaran, Carl Imhoff, and Jamie Holladay. Enabling renewable energyand the future gridwith advanced electricity storage. *JOM Journal of the Minerals, Metals and Materials Society*, 62(9):14–23, 2010.

[21] Bruno Scrosati. Recent advances in lithium ion battery materials. *Electrochimica Acta*, 45(1516):2461–2466, May 2000.

[22] Uday Kasavajjula, Chunsheng Wang, and A. John Appleby. Nano- and bulk-silicon-based insertion anodes for lithium-ion secondary cells. *Journal of Power Sources*, 163(2):1003–1039, January 2007.

[23] Jeffrey W. Fergus. Recent developments in cathode materials for lithium ion batteries. *Journal of Power Sources*, 195(4):939–954, February 2010.

[24] Sébastien Patoux, Lise Daniel, Carole Bourbon, Hélène Lignier, Carole Pagano, Frédéric Le Cras, Séverine Jouanneau, and Sébastien Martinet. High voltage spinel oxides for li-ion batteries: From the material research to the application. *Journal of Power Sources*, 189(1):344–352, April 2009.

[25] A.N Jansen, A.J Kahaian, K.D Kepler, P.A Nelson, K Amine, D.W Dees, D.R Vissers, and M.M Thackeray. Development of a high-power lithium-ion battery. *Journal of Power Sources*, 8182(0):902–905, September 1999.

[26] Atef Y. Shenouda and K.R. Murali. Electrochemical properties of doped lithium titanate compounds and their performance in lithium rechargeable batteries. *Journal of Power Sources*, 176(1):332–339, January 2008.

[27] X.L. Yao, S. Xie, C.H. Chen, Q.S. Wang, J.H. Sun, Y.L. Li, and S.X. Lu. Comparisons of graphite and spinel Li 1.33 Ti 1.67 O 4 as anode materials for rechargeable lithium-ion batteries. *Electrochimica Acta*, 50(20):4076–4081, July 2005.

[28] Ji Heon Ryu, Jae Woo Kim, Yung-Eun Sung, and Seung M. Oh. Failure modes of silicon powder negative electrode in lithium secondary batteries. *Electrochemical and Solid-State Letters*, 7(10):A306–A309, 2004.

[29] Z.S. Wen, J. Yang, B.F. Wang, K. Wang, and Y. Liu. High capacity silicon/-carbon composite anode materials for lithium ion batteries. *Electrochemistry Communications*, 5(2):165–168, February 2003.

[30] Li-Feng Cui, Yuan Yang, Ching-Mei Hsu, and Yi Cui. Carbon-Silicon Core-Shell nanowires as high capacity electrode for lithium ion batteries. *Nano Lett.*, 9(9): 3370–3374, 2009.

[31] W.J Weydanz, M Wohlfahrt-Mehrens, and R.A Huggins. A room temperature study of the binary lithium-silicon and the ternary lithium-chromium-silicon system for use in rechargeable lithium batteries. *Journal of Power Sources*, 8182 (0):237–242, September 1999.

[32] Bryan Ho. *An Experimental Study on the Structure-Property Relationship of Composite Fluid Electrodes for Use In High Energy Density Semi-Solid Flow Cells.* PhD thesis, Massachusetts Institute of Technology, 2012.

[33] Victor E. Brunini, Yet-Ming Chiang, and W. Craig Carter. Modeling the hydro-dynamic and electrochemical efficiency of semi-solid flow batteries. *Electrochimica Acta*, 69(0):301–307, May 2012.

[34] John Newman and William Tiedemann. Porous-electrode theory with battery applications. *AIChE Journal*, 21(1):25–41, 1975.

[35] Thomas F. Fuller, Marc Doyle, and John Newman. Simulation and optimization of the dual lithium ion insertion cell. *Journal of The Electrochemical Society*, 141(1):1–10, January 1994.

[36] Marc Doyle, John Newman, Antoni S. Gozdz, Caroline N. Schmutz, and Jean-Marie Tarascon. Comparison of modeling predictions with experimental data from plastic lithium ion cells. *Journal of The Electrochemical Society*, 143(6): 1890–1903, June 1996.

[37] Marc Doyle and Yuris Fuentes. Computer simulations of a Lithium-Ion polymer battery and implications for higher capacity Next-Generation battery designs. *Journal of The Electrochemical Society*, 150(6):A706–A713, June 2003.

[38] Qi Zhang, Qingzhi Guo, and Ralph E. White. *Journal of Power Sources*, 165(1): 427–435, February 2007.

[39] Lars Ole Valoen and Jan N. Reimers. Transport properties of LiPF[sub 6]-Based Li-Ion battery electrolytes. *Journal of The Electrochemical Society*, 152 (5):A882–A891, May 2005.

[40] Lawrence H. Thaller. Electrically rechargeable redox flow cell, December 1976.

[41] Johnsee Lee and J. R. Selman. Effects of separator and terminal on the current distribution in Parallel-Plate electrochemical flow reactors. *Journal of The Electrochemical Society*, 129(8):1670–1678, 1982.

[42] A.A. Shah, M.J. Watt-Smith, and F.C. Walsh. A dynamic performance model for redox-flow batteries involving soluble species. *Electrochimica Acta*, 53(27): 8087–8100, November 2008.

[43] A. A. Shah, X. Li, R. G. A. Wills, and F. C. Walsh. A mathematical model for the soluble Lead-Acid flow battery. *Journal of The Electrochemical Society*, 157 (5):A589–A599, May 2010.

[44] Venkat Srinivasan and John Newman. Discharge model for the lithium Iron-Phosphate electrode. *Journal of The Electrochemical Society*, 151(10):A1517–A1529, October 2004.

[45] Yajie Dong, Victor E. Brunini, W. Craig Carter, and Yet-Ming Chiang. Improvements of power stack performance in Semi-Solid flow cells (SSFCs). *ECS Meeting Abstracts*, 1102(17):1355–1355, 2011.

[46] John Christensen, Venkat Srinivasan, and John Newman. Optimization of lithium titanate electrodes for High-Power cells. *Journal of The Electrochemical Society*, 153(3):A560–A565, March 2006.

[47] M. Grujicic, C.L. Zhao, K.M. Chittajallu, and J.M. Ochterbeck. Cathode and interdigitated air distributor geometry optimization in polymer electrolyte membrane (PEM) fuel cells. *Materials Science and Engineering: B*, 108(3):241–252, May 2004.

[48] Nawaz Akhtar, Arshad Qureshi, Joachim Scholta, Christoph Hartnig, Matthias Messerschmidt, and Werner Lehnert. Investigation of water droplet kinetics and optimization of channel geometry for PEM fuel cell cathodes. *International Journal of Hydrogen Energy*, 34(7):3104–3111, April 2009.

[49] M. Grujicic and K.M. Chittajallu. Optimization of the cathode geometry in polymer electrolyte membrane (PEM) fuel cells. *Chemical Engineering Science*, 59(24):5883–5895, December 2004.

[50] T. Berning, D.M. Lu, and N. Djilali. Three-dimensional computational analysis of transport phenomena in a PEM fuel cell. *Journal of Power Sources*, 106(12): 284–294, April 2002.

[51] Xiangkun Ma, Huamin Zhang, and Feng Xing. A three-dimensional model for negative half cell of the vanadium redox flow battery. *Electrochimica Acta*, 58 (0):238–246, December 2011.

[52] Sarah G. Stewart, Venkat Srinivasan, and John Newman. Modeling the performance of Lithium-Ion batteries and capacitors during Hybrid-Electric-Vehicle operation. *Journal of The Electrochemical Society*, 155(9):A664–A671, 2008.

[53] Weifeng Fang, Ou Jung Kwon, and Chao-Yang Wang. Electrochemical-thermal modeling of automotive Li-ion batteries and experimental validation using a three-electrode cell. *International Journal of Energy Research*, 34(2):107–115, February 2010.

[54] M. Rychcik and M. Skyllas-Kazacos. Characteristics of a new all-vanadium redox flow battery. *Journal of Power Sources*, 22(1):59–67, January 1988.

[55] Ludwig Joerissen, Juergen Garche, Ch. Fabjan, and G. Tomazic. Possible use of vanadium redox-flow batteries for energy storage in small grids and stand-alone photovoltaic systems. *Journal of Power Sources*, 127(12):98–104, March 2004.

[56] Saft Batteries. Saft VL 45E Fe technical specifications, http://www.saftbatteries.com/doc/Documents/defence/Cube769/VL45EFe.e3741a09-74fd-4df4-8687-12997f445ef5.pdf.

[57] Yufei Chen and James W. Evans. Thermal analysis of Lithium-Ion batteries. *Journal of The Electrochemical Society*, 143(9):2708–2712, 1996.

[58] Lin Rao and John Newman. Heat-Generation rate and general energy balance for insertion battery systems. *Journal of The Electrochemical Society*, 144(8): 2697–2704, 1997.

[59] W. Annicchiarico and M. Cerrolaza. Structural shape optimization 3D finite-element models based on genetic algorithms and geometric modeling. *Finite Elements in Analysis and Design*, 37(5):403–415, May 2001.

[60] Liangsheng Wang, Prodyot K Basu, and Juan Pablo Leiva. Automobile body reinforcement by finite element optimization. *Finite Elements in Analysis and Design*, 40(8):879–893, May 2004.

[61] M.A. Tsili, A.G. Kladas, P.S. Georgilakis, A.T. Souflaris, and D.G. Paparigas. Geometry optimization of magnetic shunts in power transformers based on a particular hybrid finite-element boundary-element model and sensitivity analysis. *Magnetics, IEEE Transactions on*, 41(5):1776 – 1779, May 2005.

[62] Quoc-Hung Nguyen, Young-Min Han, Seung-Bok Choi, and Norman M Wereley. Geometry optimization of MR valves constrained in a specific volume using the finite element method. *Smart Materials and Structures*, 16(6):2242–2252, December 2007.